Low-loss Deposited Dielectrics for Superconducting Integrated Circuits

Buijtendorp, B.T.

DOI
10.4233/uuid:50173f5f-cf91-4353-b4a7-2c681fc898d8

Publication date
2025

Document Version
Final published version

Citation (APA)
Buijtendorp, B. T. (2025). *Low-loss Deposited Dielectrics for Superconducting Integrated Circuits*. [Dissertation (TU Delft), Delft University of Technology]. https://doi.org/10.4233/uuid:50173f5f-cf91-4353-b4a7-2c681fc898d8

Low-loss Deposited Dielectrics for Superconducting Integrated Circuits

B. T. Buijtendorp

Low-loss Deposited Dielectrics for Superconducting Integrated Circuits

Dissertation

for the purpose of obtaining the degree of doctor
at Delft University of Technology
by the authority of the Rector Magnificus Prof.dr.ir. T.H.J.J. van der Hagen,
Chair of the Board for Doctorates,

to be defended publicly on
Wednesday 14 May 2025 at 15:00

by

Bruno Thomas BUIJTENDORP

This dissertation has been approved by the promotors.

Composition of the doctoral committee:

Rector Magnificus	Chairperson
Prof.dr.ir. J.J.A. Baselmans	Delft University of Technology, promotor
Dr.ir. S. Vollebregt	Delft University of Technology, promotor
Dr. A. Endo	Delft University of Technology, copromotor
Independent members:	
Dr.ir. E.F.C. Driessen	Institut de Radioastronomie Millimétrique, France
Dr. R.A. Norte	Delft University of Technology
Em. Prof.dr.ir. P.M. Sarro	Delft University of Technology
Dr. E.J. Wollack	NASA Goddard Space Flight Center, USA
Prof.dr. N. Llombart Juan	Delft University of Technology, reserve member

An electronic version of this dissertation is available at https://repository.tudelft.nl/
ISBN/EAN: 978-94-6384-777-3

Contents

Summary

Deposited dielectrics with low loss at millimeter-submillimeter (mm-submm) wavelengths are beneficial for the development of superconducting integrated circuits (ICs) for astronomy, such as filter banks, on-chip Fourier-transform spectrometers, and kinetic inductance parametric amplifiers. Although it is possible to fabricate microstrip lines using crystalline Si extracted from a silicon-on-insulator wafer by a flip-bonding process, deposited dielectrics allow for simpler and more flexible chip designs and fabrication routes. In the ∼10–100 THz frequency range, dielectric losses are typically dominated by infrared absorption due to vibrational modes, whereas in the microwave frequency band (∼1–10 GHz) and at sub-Kelvin temperatures the dielectric loss is typically dominated by absorption due to two-level systems (TLSs). However, the origin of the mm-submm (∼0.1–1 THz) loss in deposited dielectrics was unknown. In this dissertation we show that the mm-submm loss in deposited dielectrics can be explained by the absorption tail of vibrational modes which are located above 10 THz. Furthermore, we found that hydrogenated amorphous silicon carbide (a-SiC:H) has a very low mm-submm loss tangent of 1.3×10^{-4} at 350 GHz, which makes it a promising low-loss deposited dielectric for mm-submm superconducting integrated circuits.

Based on a literature study we identified a-SiC:H and hydrogenated amorphous silicon (a-Si:H) as potentially promising low-loss dielectrics. In order to find the origin of the mm-submm loss, and to describe which materials we investigated in this PhD project, we characterized the dielectrics' material properties at room temperature prior to performing the cryogenic loss measurements. We deposited a-SiC:H at a substrate temperature T_{sub} of 400°C using plasma-enhanced chemical vapor deposition (PECVD), and we deposited the a-Si:H films at T_{sub} of 100°C, 250°C, and 350°C. We characterized the films' material properties using Fourier-transform infrared spectroscopy (FTIR), Raman spectroscopy and ellipsometry. For the a-Si:H we determined the hydrogen content and the microstructure parameter from the

FTIR data, the bond-angle disorder from the Raman data, and the void volume fraction from the ellipsometry data. For both the a-Si:H and the a-SiC:H we determined the band gap and optical refractive index from the ellipsometry data, and the infrared refractive index from the FTIR data. From the Raman spectra we observed that the a-SiC:H and the a-Si:H films were amorphous. Furthermore, we performed electron diffraction spectroscopy to determine the Si to C ratio of the a-SiC:H. For the a-Si:H we found that the all the material properties depend monotonically on T_{sub}. Additionally, we measured the cryogenic microwave loss of the a-Si:H films, but we found no correlation between the microwave loss and T_{sub}.

No cryogenic mm-submm and microwave loss data was available for a-SiC:H. We measured the low-power and cryogenic microwave loss of the a-SiC:H and found that the microwave loss tangent ($\tan\delta \sim 10^{-5}$) is comparable to the loss of a-Si:H. Furthermore, we measured the mm-submm loss in the range of 270–385 GHz using an on-chip Fabry-Pérot experiment. The observed mm-submm losss value of 1.2×10^{-4} at 350 GHz was significantly lower than what was reported for a-Si:H, which previously exhibited the lowest reported microwave and mm-subm wave loss values among the deposited dielectrics which are commonly used in superconducting ICs. Furthermore, we found that the mm-submm loss of the a-SiC:H increases monotonically with frequency. This was surprising in the framework of TLSs and led us to the hypothesis that another loss mechanism than TLSs might be dominant at mm-submm wavelengths. In addition to the low losses, the a-SiC:H was found to be beneficial thanks to its very low stress, lack of blisters, and the possibility to fabricate a membrane from the a-SiC:H on a c-Si wafer.

To study the origin of the frequency dependent mm-submm loss in the a-SiC:H, we extended the on-chip Fabry-Pérot experiment to the 270–600 GHz range by making use of a wideband leaky antenna. Additionally, we measured the complex dielectric constant of the a-SiC:H in the 3–100 THz range using Fourier-transform spectroscopy (FTS). We modeled the FTS data using the Maxwell-Helmholtz-Drude (MHD) dispersion model and obtained the complex dielectric constant in the 3-100 THz range. Finally, we modeled the combined on-chip loss data from the Fabry-Pérot experiments and the FTS data by fitting the MHD dispersion model in the frequency range of 0.27–100 THz. Our model demonstrates that the mm-submm loss in the a-SiC:H above 200 GHz can be explained by the absorption tail of vibrational modes which are located above 10 THz. These results pave the way for a thorough understanding of the mm-submm loss in deposited dielectrics.

The low losses of the a-SiC:H allow for integrated superconducting spectrometers with a large frequency bandwidth and relatively high resolving pow-

ers without sacrificing too much optical efficiency. This has led to the application of the a-SiC:H in the DESHIMA 2.0 filter bank, which has seen first light in 2023 at the ASTE telescope in the Atacama Desert.

Samenvatting

Gedeponeerde diëlektrica met lage verliezen bij millimeter-submillimeter (mm-submm) golflengtes zijn gunstig voor de ontwikkeling van supergeleidende geïntegreerde schakelingen (ICs) voor sterrenkunde, zoals filterbanken, on-chip Fourier-transformspectrometers en kinetische inductie parametrische versterkers. Hoewel het mogelijk is om microstriplijnen te vervaardigen met behulp van kristallijn Si (c-Si), verkregen uit een silicium-op-isolator wafer via een flip-bonding proces, maken gedeponeerde diëlektrica eenvoudigere en flexibelere chipontwerpen en fabricageroutes mogelijk. In het frequentiebereik van ∼10–100 THz worden diëlektrische verliezen typisch gedomineerd door infraroodabsorptie als gevolg van vibratiemodi, terwijl in de microgolffrequentieband (∼1–10 GHz) en bij sub-Kelvin temperaturen het diëlektrisch verlies typisch wordt gedomineerd door absorptie door twee-niveau-systemen (TLSs). De oorsprong van het mm-submm verlies (∼0.1–1 THz) in gedeponeerde diëlektrica was echter onbekend. In dit proefschrift tonen we aan dat het mm-submm verlies in gedeponeerde diëlektrica kan worden verklaard door de absorptiestaart van vibratiemodi die zich boven 10 THz bevinden. Bovendien ontdekten we dat gehydrogeneerd amorf siliciumcarbide (a-SiC:H) een zeer lage mm-submm verliestangens $\tan\delta$ heeft van 1.3×10^{-4} bij 350 GHz, wat het een veelbelovend diëlektricum met lage verliezen maakt voor mm-submm supergeleidende geïntegreerde schakelingen.

Op basis van een literatuurstudie hebben we a-SiC:H en gehydrogeneerd amorf silicium (a-Si:H) geïdentificeerd als potentieel veelbelovende diëlektrica met lage verliezen. Om de oorsprong van het mm-submm verlies te achterhalen en om te beschrijven welke materialen we in dit promotieonderzoek hebben onderzocht, hebben we de materiaaleigenschappen van de diëlektrica bij kamertemperatuur gekarakteriseerd voorafgaand aan het uitvoeren van de cryogene verliesmetingen. We hebben a-SiC:H gedeponeerd bij een substraattemperatuur T_{sub} van 400°C met behulp van plasma-geïnduceerde chemische dampdepositie (PECVD), en we hebben de a-Si:H lagen gedeponeerd bij

T_{sub} van 100°C, 250°C en 350°C. We hebben de materiaaleigenschappen van de films gekarakteriseerd met Fourier-transformspectroscopie in het infrarood (FTIR), Ramanspectroscopie en ellipsometrie. Voor de a-Si:H hebben we het waterstofgehalte en de microstructuurparameter bepaald uit de FTIR-gegevens, de bindingshoekwanorde uit de Raman-gegevens, en het volumepercentage van lege ruimten uit de ellipsometriegegevens. Voor zowel de a-Si:H als de a-SiC:H hebben we de bandkloof en de optische brekingsindex bepaald uit de ellipsometriegegevens, en de infraroodbrekingsindex uit de FTIR-gegevens. Uit de Raman-spectra observeerden we dat de a-SiC:H en de a-Si:H lagen amorf waren. Verder hebben we elektronenverstrooiingsspectroscopie uitgevoerd om de Si tot C verhouding van de a-SiC:H te bepalen. Voor de a-Si:H ontdekten we dat alle materiaaleigenschappen monotoon afhangen van T_{sub}. Daarnaast hebben we het cryogene microgolfverlies van de a-Si:H lagen gemeten, maar we vonden geen correlatie tussen het microgolfverlies en T_{sub}.

Er waren geen cryogene mm-submm en microgolfverliesgegevens beschikbaar voor a-SiC:H. We hebben het laag-vermogen en cryogene microgolfverlies van de a-SiC:H gemeten en ontdekten dat de microgolfverliestangens ($\tan\delta \sim 10^{-5}$) vergelijkbaar is met het verlies van a-Si:H. Bovendien hebben we het mm-submm verlies gemeten in het bereik van 270–385 GHz met behulp van een on-chip Fabry-Pérot experiment. De waargenomen mm-submm verlieswaarde van 1.2×10^{-4} bij 350 GHz was significant lager dan wat werd gerapporteerd voor a-Si:H, dat voorheen de laagst gerapporteerde microgolf- en mm-submm verlieswaarden vertoonde onder de gedeponeerde diëlektrica die vaak worden gebruikt in supergeleidende IC's. Verder ontdekten we dat het mm-submm verlies van de a-SiC:H monotoon toeneemt met de frequentie. Dit was verrassend binnen het kader van TLSs en leidde ons tot de hypothese dat een ander verliesmechanisme dan TLSs dominant zou kunnen zijn bij mm-submm golflengtes. Naast de lage verliezen bleek de a-SiC:H ook gunstig te zijn vanwege de zeer lage spanning, het ontbreken van blaren, en de mogelijkheid om een membraan te maken van de a-SiC:H op een c-Si wafer.

Om de oorsprong van het frequentie-afhankelijke mm-submm verlies in de a-SiC:H te bestuderen, hebben we het on-chip Fabry-Pérot experiment uitgebreid tot het bereik van 270–600 GHz door gebruik te maken van een breedbandige lekkende antenne. Daarnaast hebben we de complexe diëlektrische constante van de a-SiC:H gemeten in het bereik van 3–100 THz met behulp van Fourier-transformspectroscopie (FTS). We hebben de FTS-gegevens gemodelleerd met behulp van het Maxwell-Helmholtz-Drude (MHD) dispersiemodel en de complexe diëlektrische constante verkregen in het bereik van 3–100 THz. Ten slotte hebben we de gecombineerde on-chip verliesgegevens van de Fabry-Pérot experimenten en de FTS-gegevens gemodelleerd door het

MHD dispersiemodel te fitten in het frequentiebereik van 0.27–100 THz. Ons model toont aan dat het mm-submm verlies in de a-SiC:H boven 200 GHz kan worden verklaard door de absorptiestaart van vibratiemodi die zich boven 10 THz bevinden. Deze resultaten banen de weg voor een grondig begrip van het mm-submm verlies in gedeponeerde diëlektrica.

De lage verliezen van de a-SiC:H maken geïntegreerde supergeleidende spectrometers mogelijk met een grote frequentiebandbreedte en relatief hoge oplossende vermogens zonder al te veel optische efficiëntie in te leveren. Dit heeft geleid tot de toepassing van de a-SiC:H in de DESHIMA 2.0 filterbank, die *first light* zag in 2023 op de ASTE-telescoop in de Atacama-woestijn.

Chapter 1

Introduction

1.1. Cosmos to nano, past to present

The *kosmos* (κόσμος) was what the ancient Greek Pythagoreans called the ordered Universe. It was believed to be governed by *logos* (λόγος): A universal and divine logic which permeates all reality, and which is analogous to the human power of reasoning. The ancient Greeks were not far from the truth, since we now use the mathematical system of reasoning to formalize physics, and since it seems that the physics which holds true on Earth also holds true for galaxies located billions of light years away from us. This universality means that astronomy allows us to gain a deep understanding of the Universe. For example, gas inside the interstellar medium of distant galaxies emits light at specific frequencies which can be predicted from physical principles and which can be reproduced in our laboratories. Therefore, by performing spectrometry we gain valuable information on distant galaxies, such as on their distance to Earth and on the abundance, kinematics, and physical condition of specific gasses inside those galaxies.

It turns out that to increase our understanding of the cosmos, we first need to understand the *nano*. Nanotechnology allows us to create the extremely sensitive astronomical detectors that are necessary to detect the faint millimeter-submillimeter (mm-submm) signal from distant galaxies. Since the light from these galaxies has travelled for billions of years—from cosmos to nano, from past to present—we are developing technology which can literally look into the past and uncover what is perhaps one of the greatest mysteries: how the Universe came to be as it is.

1

1.2. Creating a three-dimensional map of the early Universe

Stars in dusty star-forming galaxies (DSFGs) in the early Universe were enshrouded by dust and therefore invisible at optical wavelengths. However, the cool interstellar gas which provides the fuel for star formation emits electromagnetic radiation at specific frequencies (emission lines) which can be observed from Earth by looking at mm-submm (∼0.1–1 THz) wavelengths. The light waves that reach Earth are stretched out due to the expansion of the Universe, and the resulting reduction in frequency is called the redshift z:

$$z = \frac{f_{\text{emitted}} - f_{\text{observed}}}{f_{\text{observed}}}, \tag{1.1}$$

where f denotes the emitted or observed frequency of the light. The observed redshift becomes larger with increased distance between the astronomical source and the observer. By measuring the redshifts of DSFGs we can determine their distances to Earth, and therefore we can also determine how far we are looking into the past.

To create a three-dimensional map of the early Universe we need an instrument which can measure a large range of possible redshifts, which means that the instrument needs to instantaneously cover a very large mm-submm frequency bandwidth. Additionally, the instrument needs sufficient resolving power $R = \frac{f}{\mathrm{d}f} \sim 500$ (where f is the measured frequency and $\mathrm{d}f$ is the smallest distinguishable frequency difference at a frequency f) to be able to distinguish the frequencies of individual gas emission lines. The requirement for R matches the expected line widths of the gas emission lines, which are broadened by a local Doppler shift due to the rotation of the DSFGs around their own center of mass. Finally, a third requirement is that the instrument needs to have a very high sensitivity to be able to measure the very faint signal from the DSFGs.

The integrated superconducting spectrometer DESHIMA 2.0 [1, 2] is the first wideband mm-submm spectrometer. With its ultra-wide bandwidth of 220–440 GHz we are able to measure the [CII] emission line (with a rest frequency of 1.9 THz) in the redshift range $z = 3.3$–7.6. This corresponds to looking 11.8–13.0 billion years into the past, compared to the current age of the Universe of 13.7 billion years. Therefore, this instrument enables us to create a three-dimensional map of the early Universe.

In Fig. 1.1 we present a schematic of the DESHIMA 2.0 chip, which has a footprint of a few cm^2. The astronomical mm-submm radiation is focused

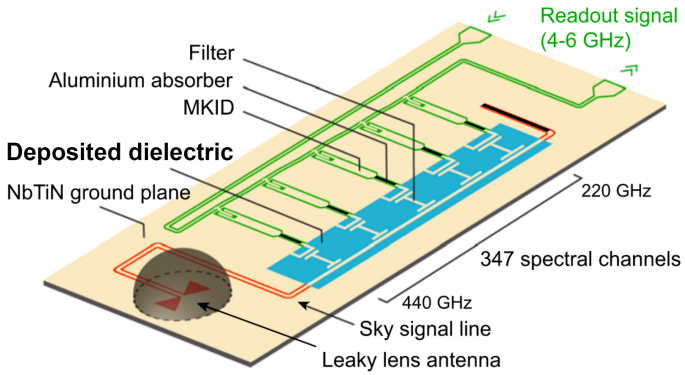

Figure 1.1: Schematic [1] of the DESHIMA 2.0 integrated superconducting spectrometer, which is a chip with a footprint of a few cm^2. The radiation couples to a wideband leaky lens antenna and travels through the coplanar waveguide (CPW) sky signal line before it reaches the microstrip filter bank which includes the deposited dielectric. The band-pass filters are half-wave mm-submm resonators and have a resolving power $R \sim 500$. Behind each filter is a microwave kinetic inductance detector (MKID), which detects the mm-submm radiation. The MKIDs are simultaneously read out by frequency multiplexing using microwave electronics.

by the telescope on a wideband leaky lens antenna. The light travels through the sky signal line and subsequently through a filter bank with 347 spectral channels that together cover the full octave 220–440 GHz bandwidth (Fig. 1.1 shows only 5 of the channels). Each spectral channel consists of a band-pass filter (shown in Fig. 1.2) which is coupled to a microwave kinetic inductance detector (MKID) to detect the filtered radiation. The MKIDs are simultaneously read out by frequency multiplexing using microwave electronics.

Both the sky signal line and filters are made from superconducting microstrip lines (shown in Fig 1.2), where two NbTiN superconducting films are separated by a deposited dielectric. Although it is possible to fabricate microstrip lines using crystalline Si (c-Si) extracted from a silicon-on-insulator wafer by a flip-bonding process [10], deposited dielectrics allow for simpler and more flexible chip designs and fabrication routes. However, deposited dielectrics typically exhibit higher losses than crystalline dielectrics, which means that a relatively large fraction of the mm-submm radiation will be dissipated inside the deposited dielectric before reaching the detectors.

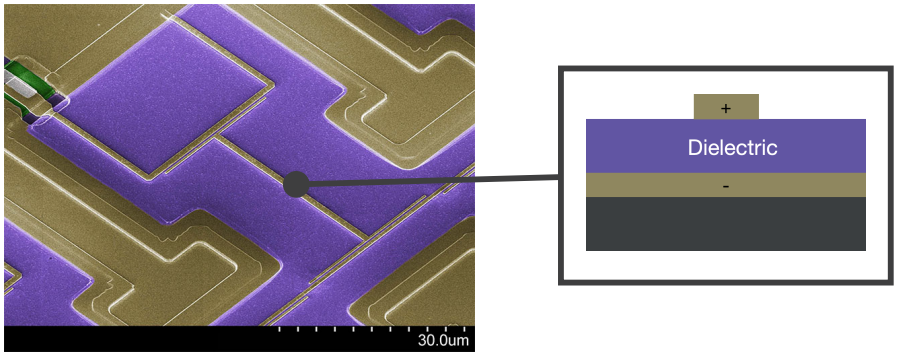

Figure 1.2: A scanning-electron micrograph [3] of a DESHIMA 2.0 filter, with the deposited dielectric colored in purple, and the NbTiN superconductor colored in gold. The annotation shows a schematic (not to scale) of the cross-section of the microstrip line. The dielectric in this micrograph is the a-Si:H (deposited at a substrate temperature T_{sub} of 250°C) which was developed in this PhD project (Chapter 2). Later versions of DESHIMA 2.0 (Fig. 5.1 in Chapter 5) have incorporated the a-SiC:H which was developed in this PhD project (Chapters 3 and 4).

1.3. Transparent dielectrics for cosmology

The maximum achievable frequency bandwidth and resolving power R are limited by dielectric losses because an increase in either of these two quantities increases the distance that the radiation has to travel through the dielectric, and therefore leads to increased transmission losses and reduced sensitivity. For the bandwidth, this is simply the case because a larger bandwidth (assuming equal R) requires a longer filter bank. For R this is the case because an increase in R leads to a proportional increase in the number of times that the radiation bounces around inside a band-pass filter before reaching the detector.

The peak transmission $|S_{31}|^2_{\mathrm{norm}}$ through a single isolated band-pass filter from the sky signal line (Fig. 1.1) into the MKID detector, normalized to the value obtained for a loss-free filter, can be expressed as:

$$|S_{31}|^2_{\mathrm{norm}} = \left(1 - \frac{R}{Q_{\mathrm{i}}}\right)^2, \tag{1.2}$$

where Q_i is the internal quality factor of the band-pass filter, which is equal[1] to $1/\tan\delta$, where $\tan\delta$ is the dielectric loss tangent. Therefore, a high Q_i implies low dielectric loss.

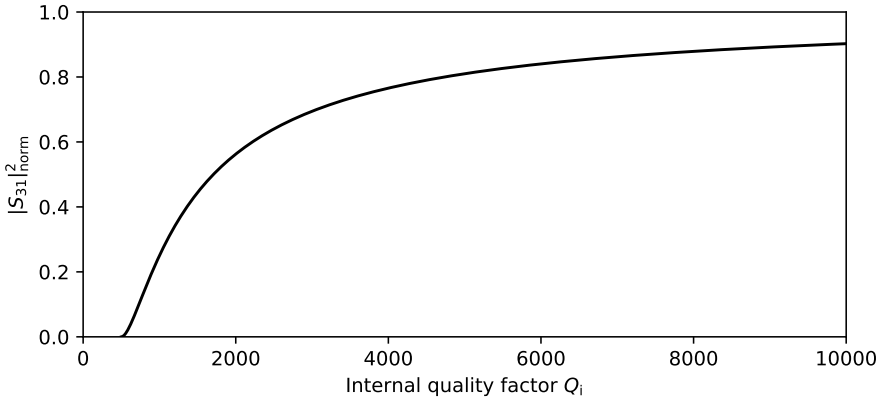

Figure 1.3: Plot of the peak transmission $|S_{31}|^2_{\mathrm{norm}}$ through a single isolated band-pass filter from the sky signal line (Fig. 1.1) into the MKID detector, normalized to the value obtained for a loss-free filter. The horizontal axis represents the internal quality factor Q_i of the band-pass filter. The filter has a resolving power $R = 500$.

In Fig. 1.3 we plotted $|S_{31}|^2_{\mathrm{norm}}$ versus Q_i for $R = 500$. The radiation coupled to the detector decreases sharply for $Q_\mathrm{i} < 2000$. At the start of this PhD project, the only loss data in the DESHIMA 2.0 frequency band for deposited dielectrics was for silicon nitride (SiN_x), which corresponded with a $Q_\mathrm{i} \sim 1440$ [7], implying a normalized filter transmission of 43% for $R = 500$. In other words, more than a factor 2 increase in sensitivity can be achieved by developing low-loss dielectrics, and the effect is even greater if higher R values are desired for future instruments.

In addition to being beneficial for DESHIMA 2.0, deposited dielectrics with low loss at mm-submm wavelengths are beneficial for the development of superconducting integrated circuits for astronomy in general [4], such as filter banks [1, 5–7], on-chip Fourier-transform spectrometers [8], and kinetic inductance parametric amplifiers [9]. Furthermore, low-loss deposited dielectrics are important for the TIFUUN instrument, which will scale the DESHIMA 2.0 technology to multiple spatial pixels. Even though there are many technologies that would greatly benefit from low-loss deposited dielectrics, the origin

[1] $Q_\mathrm{i} = 1/(p\tan\delta)$, where p is the filling fraction of the dielectric, which is close to unity for microstrip resonators.

of the mm-submm loss in deposited dielectrics was unknown at the start of this PhD project.

1.4. What is the origin of the mm-submm loss in deposited dielectrics?

In the ∼10–100 THz frequency range, dielectric losses are typically dominated by infrared absorption due to vibrational modes [11–20], whereas in the microwave frequency range (∼1–10 GHz) and at sub-Kelvin temperatures the dielectric loss is typically dominated by absorption due to two-level systems (TLSs) [21–23]. The mechanism behind the loss in the intermediate mm-submm (∼0.1–1 THz) frequency range was unknown at the start of this PhD project. Therefore, we investigated if the loss in the mm-submm frequency range is explained by the absorption tail of infrared vibrational modes, by TLS loss, or by a combination of these two loss mechanisms.

The infrared absorption in a-Si:H and a-SiC:H can be attributed to specific vibrational modes that are directly related to the composition and microstructure of the dielectric [11–17, 17–20, 24, 25]. In contrast, the microscopic origin of the TLSs in these materials remains unknown [22]. However, TLSs are successfully modeled by the standard tunneling model (STM) [21] and relations between TLSs and various material properties have been reported in literature (Section 2.1.1).

In Fig. 1.4 we plotted an overview of the cryogenic loss tangent versus frequency data which had been reported in literature at the start of this PhD project. We observed that: (1) Hydrogenated amorphous silicon (a-Si:H) had the lowest reported microwave losses, and significantly lower microwave losses than a-Si (evaporated and hydrogen-free). This is in agremeent with a reported correlation between TLS-loss and dangling bond density [26], since hydrogen atoms passivate dangling bonds; (2) The mm-submm loss of SiN_x is higher than its microwave loss, suggesting that the mm-submm loss is dominated by a loss mechanism other than TLSs (since the TLS density is expected to be frequency-independent [21]). However, the comparison of the microwave loss data and mm-submm loss data of the SiN_x is difficult since no material characterization was provided; (3) The loss of SiO_2 at 100 GHz is comparable to the microwave loss, suggesting that the loss in SiO_2 at 100 GHz is dominated by TLSs [29].

In this PhD project we initially focused on a-Si:H (Chapter 2) due to the reported low microwave losses ($\tan\delta \sim 10^{-5}$). However, during the course

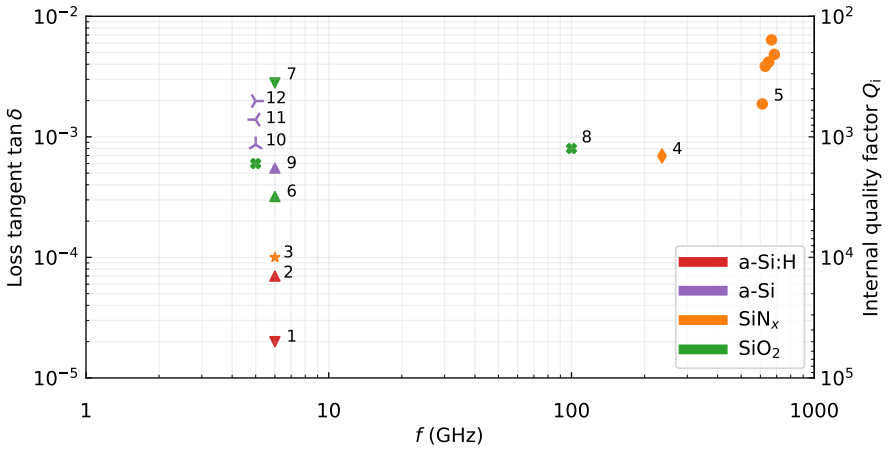

Figure 1.4: An overview of the mm-submm wave and microwave cryogenic dielectric loss tangent data, which had been reported in literature at the start of this PhD project for various deposited dielectrics. Data sources: (1) Ref. [23], PPC; (2): Ref. [23], CPW; (3) Ref. [23], PPC; (4) Ref. [7], microstrip; (5) Ref. [28], CPW; (6) Ref. [23], CPW, thermal SiO_2; (7) Ref. [23], CPW, sputtered SiO_2; (8) Ref. [29], microstrip; (9) Ref. [23], CPW; (10): Ref. [26], $T_{sub} = 50°C$; (11): Ref. [26], $T_{sub} = 225°C$; (12): Ref. [26], $T_{sub} = 425°C$.

of the PhD project we measured very low mm-submm losses in hydrogenated amorphous silicon carbide a-SiC:H (Chapter 3), which has led us to transition our focus to a-SiC:H. The cryogenic mm-submm and microwave losses of a-SiC:H had not yet been measured at the start of this PhD project. However, the suggested relations in literature between TLS-loss and various material properties made it promising that a-SiC:H is a four-fold coordinated and hydrogenated material, similar to a-Si:H. Furthermore, it was reported that low-stress a-SiC:H films can be deposited by PECVD, even at a high T_{sub} of 400°C [30]. Additionally, the a-SiC:H films do not exhibit blisters, which are a common issue with a-Si:H [31, 32]. Furthermore, a-SiC:H has high wet etching selectivity with Si [30], enabling an a-SiC:H film to be used as a membrane, for example in superconducting photon detectors [33]. These properties suggested that a-SiC:H would be a promising alternative to a-Si:H and SiN_x for superconducting devices.

During the course of this PhD project there have been mutiple reports on low-loss deposited dielectrics. In 2021 I co-authored an article [34] where the 6 GHz and 350 GHz cryogenic losses were measured of the 250°C a-Si:H film which we present in this dissertation. This provided the first cryogenic mm-

submm loss measurements of a-Si:H, and it was found that the a-Si:H exhibited significantly lower mm-submm losses ($\tan\delta = 2.1 \times 10^{-4}$) than SiN_x and SiO_2 (Fig. 1.4). The low-power microwave loss ($\tan\delta \sim 10^{-5}$) was comparable to previous reports on a-Si:H. Furthermore, in 2021 it was reported that an evaporated amorphous germanium film had a very low low-power microwave loss tangent of 5×10^{-6} [35]. Additionally, in 2024 there has been a report of a-Si:H films in parallel plate capacitors deposited at a T_{sub} of 350°C [36]. The authors reported a PECVD a-Si:H film with a low-power microwave loss tangent of 1×10^{-5}, and a film deposited by inductively coupled plasma chemical vapor deposition (ICPCVD) with a low-power microwave loss tangent of 7×10^{-6}.

1.5. Research questions

This PhD project had two research questions:

- Can we deposit dielectrics that have significantly lower mm-submm loss than the state of the art?
- What is the origin of the mm-submm loss in deposited dielectrics?

The steps that we took to answer the two research questions are presented in the outline of the dissertation (Section 1.6).

1.6. Outline of this dissertation

Chapter 2 focuses on the material characterization at room temperature of a-Si:H and a-SiC:H deposited by PECVD, and on the cryogenic microwave loss measurements of a-Si:H. We deposited the a-Si:H at T_{sub} of 100°C, 250°C and 350°C and we deposited the a-SiC:H at a T_{sub} of 400°C. The measured Raman spectra confirmed that the films were fully amorphous. We obtained the films' infrared refractive indices from the measured Fourier-transform infrared (FTIR) spectra, and from the FTIR spectra we observed that the infrared absorption of the a-Si:H films was dominated by the Si-H_x absorption band near 640 cm^{-1} (19 THz), whereas the infrared absorption of the a-SiC:H film was dominated by Si-C stretching modes near 750 cm^{-1} (22 THz). We observed that the intensity of the Si-H_x absorption band near 640 cm^{-1} decreased with

increasing T_{sub}. Additionally, we obtained the 1–4 eV (242–967 THz) complex dielectric constant and band gap values of the a-Si:H and a-SiC:H films from ellipsometry measurements. Furthermore, we measured the cryogenic microwave loss of the a-Si:H films and we found that all three a-Si:H films exhibited a $\tan\delta < 10^{-5}$ at 120 mK and at an average photon number of 10^5, equivalent to –55 dBm internal resonator power. Finally, for the a-Si:H films we obtained the hydrogen content and microstructure parameter from the FTIR spectra, the bond-angle disorder from the Raman spectra and the void volume fraction from the ellipsometry spectra. We observed that the hydrogen content, microstructure parameter, bond-angle disorder and void volume fraction of the a-Si:H decreased with increasing T_{sub} and that the refractive index increased with increasing T_{sub}. We did not observe a correlation of the room temperature properties of the a-Si:H with its measured cryogenic microwave loss. The observation that the intensity of the Si-H_x absorption band near 640 cm^{-1} decreased with increasing T_{sub} was interesting under the hypothesis that the mm-submm loss of the a-Si:H and a-SiC:H could be caused by the absorption tail of infrared vibrational modes, suggesting that the a-Si:H could be optimized for low mm-submm loss by depositing films at elevated T_{sub}. However, for the a-Si:H film that was deposited at 350°C we measured high compressive stress values and observed blistering defects, which made it impractical to fabricate devices with this material. In contrast, the a-SiC:H film exhibited a low stress value and no blistering defects even at a high T_{sub} of 400°C.

Chapter 3 introduces a-SiC:H as a novel low-loss deposited dielectric. We measured the low-power microwave loss and show that it is comparable to the microwave loss of the a-Si:H. Furthermore, we measured the loss in the 270–385 GHz frequency range using an on-chip Fabry-Pérot experiment. We show that the mm-submm losses are significantly lower than that of other deposited dielectrics such as a-Si:H, SiN_x and SiO_x. For this reason we transitioned our focus from a-Si:H to a-SiC:H. Furthermore, we observed that the mm-submm loss is strongly frequency-dependent, which is surprising in the framework of the STM for TLSs. This led us to the hypothesis that the mm-submm loss is caused by the absorption tail of infrared vibrational modes and not by TLSs.

Chapter 4 focuses on the origin of the mm-submm loss in the a-SiC:H. We extended the on-chip Fabry-Pérot measurements to the 270–600 GHz frequency range by replacing the narrow-band twin slot antenna of the Fabry-Pérot chip with a wideband leaky antenna. Furthermore, we performed Fourier-transform spectroscopy of the a-SiC:H in the 3–100 THz frequency range. We modeled the combined on-chip mm-submm loss data and the FTS data using a Maxwell-Helmholtz-Drude dispersion model, demonstrating that the losses

of the a-SiC:H in the 0.27–100 THz frequency range can be explained by the absorption tail of infrared vibrational modes. In addition to the TU Delft / SRON collaboration which I belonged to, this part of the work was done in collaboration with researchers from NASA Goddard Space Flight Center.

Chapter 5 gives the conclusions of this dissertation, and discusses the applications of the a-SiC:H in on-chip mm-submm superconducting astronomical instruments. We discuss the impact of the work, and finally we give an outlook for future research and applications.

Bibliography

[1] A. Taniguchi, T. J. L. C. Bakx, J. J. A. Baselmans, R. Huiting, K. Karatsu, N. Llombart, M. Rybak, T. Takekoshi, Y. Tamura, H. Akamatsu, S. Brackenhoff, J. Bueno, B. T. Buijtendorp, S. O. Dabironezare, A.-K. Doing, Y. Fujii, K. Fujita, M. Gouwerok, S. Hähnle, T. Ishida, S. Ishii, R. Kawabe, T. Kitayama, K. Kohno, A. Kouchi, J. Maekawa, K. Matsuda, V. Murugesan, S. Nakatsubo, T. Oshima, A. Pascual Laguna, D. J. Thoen, P. P. Van Der Werf, S. J. C. Yates, and A. Endo, "DESHIMA 2.0: Development of an Integrated Superconducting Spectrometer for Science-Grade Astronomical Observations," *Journal of Low Temperature Physics*, vol. 209, pp. 278–286, Nov. 2022.

[2] A. Endo, K. Karatsu, Y. Tamura, T. Oshima, A. Taniguchi, T. Takekoshi, S. Asayama, T. J. L. C. Bakx, S. Bosma, J. Bueno, K. W. Chin, Y. Fujii, K. Fujita, R. Huiting, S. Ikarashi, T. Ishida, S. Ishii, R. Kawabe, T. M. Klapwijk, K. Kohno, A. Kouchi, N. Llombart, J. Maekawa, V. Murugesan, S. Nakatsubo, M. Naruse, K. Ohtawara, A. Pascual Laguna, J. Suzuki, K. Suzuki, D. J. Thoen, T. Tsukagoshi, T. Ueda, P. J. de Visser, P. P. van der Werf, S. J. C. Yates, Y. Yoshimura, O. Yurduseven, and J. J. A. Baselmans, "First light demonstration of the integrated superconducting spectrometer," *Nat. Astron.*, vol. 3, no. 11, pp. 989–996, 2019.

[3] D. J. Thoen, V. Murugesan, A. Pascual Laguna, K. Karatsu, A. Endo, and J. J. A. Baselmans, "Combined ultraviolet- and electron-beam lithography with Micro-Resist-Technology GmbH ma-N1400 resist," *Journal of Vacuum Science & Technology B*, vol. 40, p. 052603, Sept. 2022.

[4] N. Jovanovic, P. Gatkine, N. Anugu, R. Amezcua-Correa, R. Basu Thakur, C. Beichman, C. F. Bender, J.-P. Berger, A. Bigioli, J. Bland-Hawthorn, G. Bourdarot, C. M. Bradford, R. Broeke,

J. Bryant, K. Bundy, R. Cheriton, N. Cvetojevic, M. Diab, S. A. Diddams, A. N. Dinkelaker, J. Duis, S. Eikenberry, S. Ellis, A. Endo, D. F. Figer, M. P. Fitzgerald, I. Gris-Sanchez, S. Gross, L. Grossard, O. Guyon, S. Y. Haffert, S. Halverson, R. J. Harris, J. He, T. Herr, P. Hottinger, E. Huby, M. Ireland, R. Jenson-Clem, J. Jewell, L. Jocou, S. Kraus, L. Labadie, S. Lacour, R. Laugier, K. Ławniczuk, J. Lin, S. Leifer, S. Leon-Saval, G. Martin, F. Martinache, M.-A. Martinod, B. A. Mazin, S. Minardi, J. D. Monnier, R. Moreira, D. Mourard, A. S. Nayak, B. Norris, E. Obrzud, K. Perraut, F. Reynaud, S. Sallum, D. Schiminovich, C. Schwab, E. Serbayn, S. Soliman, A. Stoll, L. Tang, P. Tuthill, K. Vahala, G. Vasisht, S. Veilleux, A. B. Walter, E. J. Wollack, Y. Xin, Z. Yang, S. Yerolatsitis, Y. Zhang, and C.-L. Zou, "2023 Astrophotonics Roadmap: Pathways to realizing multi-functional integrated astrophotonic instruments," *Journal of Physics: Photonics*, vol. 5, p. 042501, Oct. 2023.

[5] A. Pascual Laguna, K. Karatsu, D. Thoen, V. Murugesan, B. Buijtendorp, A. Endo, and J. Baselmans, "Terahertz Band-Pass Filters for Wideband Superconducting On-Chip Filter-Bank Spectrometers," *IEEE Transactions on Terahertz Science and Technology*, vol. 11, pp. 635–646, Nov. 2021.

[6] K. S. Karkare, P. S. Barry, C. M. Bradford, S. Chapman, S. Doyle, J. Glenn, S. Gordon, S. Hailey-Dunsheath, R. M. J. Janssen, A. Kovács, H. G. LeDuc, P. Mauskopf, R. McGeehan, J. Redford, E. Shirokoff, C. Tucker, J. Wheeler, and J. Zmuidzinas, "Full-Array Noise Performance of Deployment-Grade SuperSpec mm-Wave On-Chip Spectrometers," *J. Low Temp. Phys.*, vol. 199, no. 3-4, pp. 849–857, 2020.

[7] S. Hailey-Dunsheath, P. S. Barry, C. M. Bradford, G. Chattopadhyay, P. Day, S. Doyle, M. Hollister, A. Kovacs, H. G. LeDuc, N. Llombart, P. Mauskopf, C. McKenney, R. Monroe, H. T. Nguyen, R. O'Brient, S. Padin, T. Reck, E. Shirokoff, L. Swenson, C. E. Tucker, and J. Zmuidzinas, "Optical Measurements of SuperSpec: A Millimeter-Wave On-Chip Spectrometer," *J. Low Temp. Phys.*, vol. 176, no. 5-6, pp. 841–847, 2014.

[8] R. Basu Thakur, A. Steiger, S. Shu, F. Faramarzi, N. Klimovich, P. K. Day, E. Shirokoff, P. D. Mauskopf, and P. S. Barry, "Development of Superconducting On-chip Fourier Transform Spectrometers," *Journal of Low Temperature Physics*, vol. 211, pp. 227–236, June 2023.

[9] B.-K. Tan, N. Klimovich, R. Stephenson, F. Faramarzi, and P. Day, "Operation of kinetic-inductance travelling wave parametric amplifiers at millimetre wavelengths," *Superconductor Science and Technology*, vol. 37, p. 035006, Mar. 2024.

[10] A. Patel, A. Brown, W. Hsieh, T. Stevenson, S. H. Moseley, K. U-yen, N. Ehsan, E. Barrentine, G. Manos, and E. J. Wollack, "Fabrication of MKIDS for the MicroSpec Spectrometer," *IEEE Transactions on Applied Superconductivity*, vol. 23, pp. 2400404–2400404, June 2013.

[11] G. Cataldo, J. A. Beall, H.-M. Cho, B. McAndrew, M. D. Niemack, and E. J. Wollack, "Infrared dielectric properties of low-stress silicon nitride," *Optics Letters*, vol. 37, p. 4200, Oct. 2012.

[12] G. Cataldo, E. J. Wollack, A. D. Brown, and K. H. Miller, "Infrared dielectric properties of low-stress silicon oxide," *Optics Letters*, vol. 41, p. 1364, Apr. 2016.

[13] M. Cardona, "Vibrational spectra of hydrogen in silicon and germanium," *Physica Status Solidi (B)*, vol. 118, no. 2, pp. 463–481, 1983.

[14] M. H. Brodsky, M. Cardona, and J. J. Cuomo, "Infrared and Raman spectra of the silicon-hydrogen bonds in amorphous silicon prepared by glow discharge and sputtering," *Physical Review B*, vol. 16, pp. 3556–3571, Oct. 1977.

[15] W. Jacob, A. Von Keudell, and T. Schwarz-Selinger, "Infrared analysis of thin films: Amorphous, hydrogenated carbon on silicon," *Braz. J. Phys.*, vol. 30, no. 3, pp. 508–516, 2000.

[16] S. King, M. French, J. Bielefeld, and W. Lanford, "Fourier transform infrared spectroscopy investigation of chemical bonding in low-k a-SiC:H thin films," *Journal of Non-Crystalline Solids*, vol. 357, pp. 2970–2983, July 2011.

[17] A. A. Langford, M. L. Fleet, B. P. Nelson, W. A. Lanford, and N. Maley, "Infrared absorption strength and hydrogen content of hydrogenated amorphous silicon," *Physical Review B*, vol. 45, pp. 13367–13377, June 1992.

[18] N. Maley, "Critical investigation of the infrared-transmission-data analysis of hydrogenated amorphous silicon alloys," *Physical Review B*, vol. 46, pp. 2078–2085, July 1992.

[19] H. Shanks, W. Kamitakahara, J. McClelland, and C. Carlone, "Phonon density of states of amorphous silicon," *Journal of Non-Crystalline Solids*, vol. 59–60, pp. 197–200, Dec. 1983.

[20] J. D. Ouwens and R. E. I. Schropp, "Hydrogen microstructure in hydrogenated amorphous silicon," *Physical Review B*, vol. 54, pp. 17759–17762, Dec. 1996.

[21] W. A. Phillips, "Tunneling states in amorphous solids," *J. Low Temp. Phys.*, vol. 7, no. 3-4, pp. 351–360, 1972.

[22] C. Müller, J. H. Cole, and J. Lisenfeld, "Towards understanding two-level-systems in amorphous solids: Insights from quantum circuits," *Rep. Prog. Phys.*, vol. 82, no. 12, p. 124501, 2019.

[23] A. D. O'Connell, M. Ansmann, R. C. Bialczak, M. Hofheinz, N. Katz, E. Lucero, C. McKenney, M. Neeley, H. Wang, E. M. Weig, A. N. Cleland, and J. M. Martinis, "Microwave dielectric loss at single photon energies and millikelvin temperatures," *Appl. Phys. Lett.*, vol. 92, no. 11, p. 112903, 2008.

[24] R. Street, *Hydrogenated Amorphous Silicon.* (Cambridge Solid State Science Series), Cambridge University Press, 1991.

[25] A. H. M. Smets, W. M. M. Kessels, and M. C. M. van de Sanden, "Vacancies and voids in hydrogenated amorphous silicon," *Applied Physics Letters*, vol. 82, pp. 1547–1549, Mar. 2003.

[26] M. Molina-Ruiz, Y. J. Rosen, H. C. Jacks, M. R. Abernathy, T. H. Metcalf, X. Liu, J. L. DuBois, and F. Hellman, "Origin of mechanical and dielectric losses from two-level systems in amorphous silicon," *Phys. Rev. Mater.*, vol. 5, no. 3, p. 035601, 2021.

[27] D. Queen, X. Liu, J. Karel, H. Jacks, T. Metcalf, and F. Hellman, "Two-level systems in evaporated amorphous silicon," *Journal of Non-Crystalline Solids*, vol. 426, pp. 19–24, Oct. 2015.

[28] A. Endo, C. Sfiligoj, S. J. C. Yates, J. J. A. Baselmans, D. J. Thoen, S. M. H. Javadzadeh, P. P. van der Werf, A. M. Baryshev, and T. M. Klapwijk, "On-chip filter bank spectroscopy at 600–700 GHz using NbTiN superconducting resonators," *Appl. Phys. Lett.*, vol. 103, no. 3, p. 032601, 2013.

[29] J. Gao, A. Vayonakis, O. Noroozian, J. Zmuidzinas, P. K. Day, H. G. Leduc, B. Young, B. Cabrera, and A. Miller, "Measurement of loss in superconducting microstrip at millimeter-wave frequencies," in *The Thirteenth International Workshop on Low Temperature Detectors — LTD13*, (Stanford (California)), pp. 164–167, 2009.

[30] P. Sarro, C. de Boer, E. Korkmaz, and J. Laros, "Low-stress PECVD SiC thin films for IC-compatible microstructures," *Sens. Actuator A Phys.*, vol. 67, no. 1-3, pp. 175–180, 1998.

[31] Y. Mishima and T. Yagishita, "Investigation of the bubble formation mechanism in a-Si:H films by Fourier-transform infrared microspectroscopy," *J. Appl. Phys.*, vol. 64, no. 8, pp. 3972–3974, 1988.

[32] J. Wang, L. Wu, X. Chen, W. Zhuo, and G. Wang, "Avoiding blister defects in low-stress hydrogenated amorphous silicon films for MEMS sensors," *Sens. Actuator A Phys.*, vol. 276, pp. 11–16, 2018.

[33] P. J. de Visser, S. A. H. de Rooij, V. Murugesan, D. J. Thoen, and J. J. A. Baselmans, "Phonon-trapping enhanced energy resolution in superconducting single photon detectors," *arXiv:2103.06723 [astro-ph, physics:cond-mat, physics:physics]*, Mar. 2021.

[34] S. Hähnle, K. Kouwenhoven, B. Buijtendorp, A. Endo, K. Karatsu, D. Thoen, V. Murugesan, and J. Baselmans, "Superconducting Microstrip Losses at Microwave and Submillimeter Wavelengths," *Phys. Rev. Appl.*, vol. 16, no. 1, p. 014019, 2021.

[35] C. J. Kopas, J. Gonzales, S. Zhang, D. R. Queen, B. Wagner, M. Robinson, J. Huffman, and N. Newman, "Low microwave loss in deposited Si and Ge thin-film dielectrics at single-photon power and low temperatures," *AIP Advances*, vol. 11, p. 095007, Sept. 2021.

[36] F. Defrance, A. D. Beyer, S. Shu, J. Sayers, and S. R. Golwala, "Characterization of the low electric field and zero-temperature two-level-system loss in hydrogenated amorphous silicon," *Physical Review Materials*, vol. 8, p. 035602, Mar. 2024.

[37] B. A. Mazin, D. Sank, S. McHugh, E. A. Lucero, A. Merrill, J. Gao, D. Pappas, D. Moore, and J. Zmuidzinas, "Thin film dielectric microstrip kinetic inductance detectors," *Appl. Phys. Lett.*, vol. 96, no. 10, p. 102504, 2010.

Chapter 2

Material characterization

2.1. Introduction

The origin of the loss in the mm-submm frequency range (∼0.1–1 THz) was unknown at the start of this PhD project (Section 1.4). Therefore, in this dissertation we investigated if the mm-submm loss was caused by TLSs, by the absorption tail of infrared vibrational modes, or by some other loss mechanism. In this chapter we present characterization measurements of the material properties of a-Si:H deposited by PECVD at T_{sub} of 100°C, 250°C and 350°C, and of a-SiC:H deposited by PECVD at a T_{sub} of 400°C. Thereby we aim to:

- Describe which materials were investigated in this dissertation, which is necessary due to the many degrees of freedom of the compositional and microstructural properties of a-Si:H and a-SiC:H. We measured the infrared absorption spectra, Raman spectra, film stress and band gap of the a-Si:H and a-SiC:H (Sections 2.3–2.6).
- Investigate if the microwave TLS loss and the compositional and microstructural material properties of a-Si:H can be tuned by changing the T_{sub} during the PECVD deposition process, and if there is a correlation between the TLS loss and the material properties of a-Si:H. In addition to the room temperature characterizations (Sections 2.3–2.6), we measured the cryogenic microwave loss of a-Si:H (Section 2.7).
- Investigate which infrared vibrational modes are present in a-Si:H and a-SiC:H (Section 2.4).

This chapter was based on a published article [1].

To put this chapter into the context of the subsequent chapters of this dissertation, we note that the detailed investigation of a-Si:H which we present in this chapter was motivated by the reported low microwave losses ($\tan\delta \sim 10^{-5}$) of this material [2, 3]. In Chapter 3 we present the microwave loss and mm-submm loss of a-SiC:H, where we observed that although the microwave loss of a-SiC:H was comparable to the microwave loss of a-Si:H, the mm-submm loss was significantly lower than what has been reported for other deposited dielectrics. This motivated us to focus our subsequent research on a-SiC:H and to investigate in Chapter 4 how the infrared vibrational modes of a-SiC:H are related to its mm-submm loss. Furthermore, in Section 4.2, we provide additional characterization by measuring the Si/C ratio of the a-SiC:H.

2.1.1. Relation between the TLS loss and the material properties of a-Si:H

Although the origin of the TLS loss is unknown [4], there have been multiple reports on the relations between the material properties and the TLS density in a-Si and a-Si:H. Interestingly, a relation has been reported between the TLS density and dangling bond density [5], and the dangling bond density in a-Si has been reported to be related to voids in the dielectric [6]. These findings suggest that there could be a relationship between the TLS density and the microstructure of a-Si:H. The microstructure of a-Si:H is known to be largely governed by the occurrence of SiH and SiH_2 configurations in the material [7–9]. The SiH configurations reside mostly in small vacancies, corresponding to up to three missing Si atoms [8] per vacancy. This is in contrast to the SiH_2 configurations that exist mostly on the surface of voids with a radius of 1–4 nm, corresponding to 10^2 to 10^4 missing Si atoms [8] per void. The fraction of Si atoms that are bonded as SiH_3 is negligible below hydrogen concentrations of 40% [10]. Furthermore, it has been suggested that a higher coordination number (the average number of bonds per atom) leads to lower TLS loss [2], due to the observation that the fourfold-coordinated material a-Si:H has relatively low TLS loss compared to materials such as SiN_x and SiO_x with lower coordination numbers. Finally, for a-Si it has been found that deposition at elevated T_{sub} leads to increased film density, decreased dangling bond density, and decreased TLS density.

Even if we assume that the TLS density in a-Si:H is related to the dangling bond density, the relation between the TLS density and the material properties of a-Si:H is not obvious. On the one hand, a large concentration of SiH_2 bonds suggests a large void volume fraction that could potentially

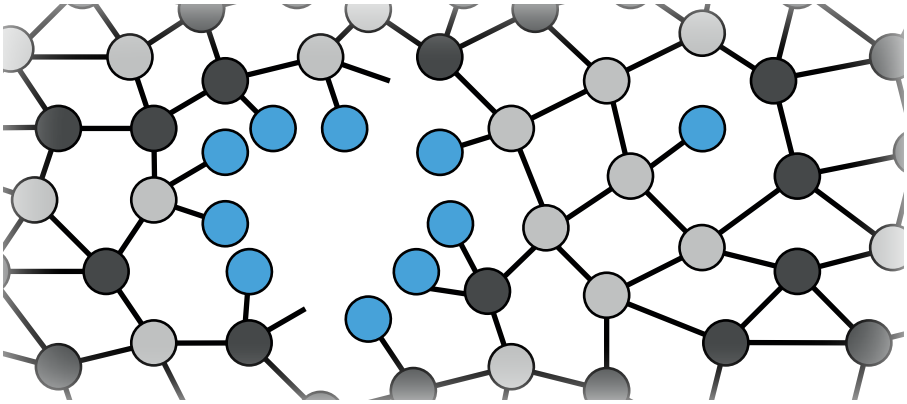

Figure 2.1: Illustration of a-SiC:H, or equivalently an illustration of a-Si:H in the case where all carbon atoms are replaced by silicon atoms. The light grey circles represent silicon atoms, the dark grey circles represent carbon atoms, and the blue circles represent hydrogen atoms. The schematic a monovacancy with a SiH defect, and a small void with SiH and SiH_2 defects and dangling bonds.

host dangling bonds. On the other hand, the incorporation of hydrogen leads to passivation of dangling bonds, and this is a potential explanation of why a-Si:H has lower TLS loss than a-Si. Based on our literature study, we hypothesized that depositing a-Si:H at elevated T_{sub} leads to a denser material with less disorder and a decrease in the TLS loss. Furthermore, we expected that we can control the following material properties by changing T_{sub}, and we investigated if the following material properties of a-Si:H are correlated to the TLS density:

- The infrared refractive index n_{3000} at 3000 cm$^-$1, measured using Fourier-transform infrared spectroscopy (FTIR). We expect that the n_{3000} increases with T_{sub} due to a decrease in void volume fraction [11].
- The hydrogen content C_{H}, measured using FTIR by integrating the SiH_x absorption peak at 640 cm^{-1} [7, 12]. We expect that C_{H} decreases with T_{sub} due to a decrease in void volume fraction and corresponding decrease in the amount of SiH_2 bonds [7–9].
- The microstructure parameter R^*, measured using FTIR, which quantifies the relative amount of SiH and SiH_2 bonds [7]. A large R^* points to a relatively large amount of SiH_2 bonds, which reside mostly on the surface of voids. Therefore, we expect that R^* decreases with increasing T_{sub}.

- The bond-angle disorder $\Delta\theta$, measured by determining the position of the transverse optical (TO) phonon mode at roughly 480 cm^{-1} using Raman spectroscopy [13]. We expect that $\Delta\theta$ decreases with increasing T_{sub} due to a decreased disorder of the silicon network.

- The void volume fraction f_v, measured using ellipsometry [11]. We expect that f_v decreases with increasing T_{sub} [6].

2.1.2. Infrared vibrational modes in a-Si:H and a-SiC:H

The infrared vibrational modes of a-Si:H and a-SiC:H played a fundamental role in this dissertation. We hypothesized that the absorption tail of infrared vibrational modes could potentially cause significant mm-submm losses. Furthermore, we hypothesized that TLS loss could contribute to the mm-submm loss, and in Subsection 2.1.1 we pointed towards literature that suggests that the TLS density could be related to the occurrence of specific infrared vibrational modes. We used two complementary methods to measure the vibrational modes in a-Si:H and a-SiC:H: FTIR spectroscopy and Raman spectroscopy. Whereas the infrared absorption measured using FTIR is a direct measurement of dielectric loss at infrared wavelengths, the measured Raman scattering intensity provides us with the bond-angle disorder and can show us if the films are amorphous or polycrystalline.

These two measurement methods are complementary because not all infrared-active modes are Raman-active and vice versa. Infrared absorption (measured by FTIR) only occurs if the excitation induces an oscillating dipole moment. Raman spectroscopy, on the other hand, measures inelastic scattering at visible wavelengths that is caused by the excitation of infrared vibrational modes, and the Raman scattering only occurs if the excitation induces an oscillating polarizability. This means that vibrations involving polar bonds, such as Si-H and Si-C, exhibit infrared absorption. In contrast, the vibration of the Si-Si bond exhibits no oscillating dipole moment and no infrared absorption, but it is strongly Raman active due to an induced change in polarizability. The vibrational modes in a-Si:H and a-SiC:H that we measured using FTIR and Raman spectroscopy can be divided into two categories: phonon modes caused by oscillations of the atomic network, and local vibrational modes that are similar to molecular vibrational modes.

Despite the lack of long-range order in amorphous dielectrics such as a-Si:H and a-SiC:H, these materials typically retain some of the vibrational characteristics of their crystalline counterparts by exhibiting vibrational modes that

can propagate over some small distance through the disordered network, and that are commonly referred to as phonon modes. These semi-localized phonon modes are typically broadened, caused by the averaging of many vibrational frequencies due to the heterogeneity of the disordered network. Furthermore, the disordered network is generally less stiff than the crystal lattice, which causes a reduced resonance frequency. For example, c-Si exhibits a transverse-optical (TO) phonon mode at 520 cm^{-1} and a-Si, a-Si:H and a-SiC:H exhibit a broadened TO phonon mode at roughly 480 cm^{-1}. Here, the label transverse refers to atomic oscillations that are perpendicular to the direction of propagation, in contrast to longitudinal modes where the atomic oscillations are parallel to the direction of propagation. The label "optical" refers to a type of mode where neighboring atoms move out of phase with each other, and this term historically comes from research on ionic crystals where the out of phase oscillations generate oscillating electric dipoles that couple strongly to electromagnetic waves. In contrast, in acoustic phonon modes the atoms move in phase with each other, resembling sound waves, hence the name "acoustic".

The local vibrational modes are tied to specific chemical bonds in impurities such as Si-H_x groups, in contrast to the phonon modes which are related to vibrations of the atomic network. The local vibrational modes are very similar to molecular vibrations, since they arise from the oscillating relative motion of small groups of atoms that are bonded together. For example, the polar Si-H bond exhibits an oscillation of the Si-H distance (stretching mode) which causes an oscillating dipole moment that couples to the EM-field and thereby causes infrared absorption. Other types of modes are rocking, wagging, twisting, and bending (scissoring) modes. In this chapter we were mainly interested in the following vibrational modes that were known to be present in a-Si:H and a-SiC:H:

- **480** cm^{-1} (14 THz): The TO phonon mode of the Si network [13], measured using Raman spectroscopy. From its center frequency we calculated the $\Delta\theta$ of the a-Si:H films (Subsection 2.5.3).
- **640** cm^{-1} (19 THz): The Si-H_x absorption band, measured using FTIR. From its integrated absorption we calculated the C_H of the a-Si:H films [7, 12] (Subsection 2.4.5).
- **750** cm^{-1} (22 THz): The Si-C stretching modes, measured using FTIR [14] (Subsection 2.4.4).
- **980** cm^{-1} (29 THz): The Si-CH_2-Si wagging modes, measured using FTIR [14] (Subsection 2.4.4).

- **2000** cm^{-1} (60 THz): The Si-H stretching mode [7], measured using FTIR. From its intensity we calculated the R^* of the a-Si:H films (Subsection 2.4.5).

- **2100** cm^{-1} (63 THz): The $Si-H_2$ stretching mode [7], measured using FTIR. From its intensity we calculated the R^* of the a-Si:H films (Subsection 2.4.5) [7].

2.2. Plasma-enhanced chemical vapor deposition of the a-Si:H and a-SiC:H

We deposited the a-Si:H films by PECVD with an Oxford Plasmalab 80 Plus. The a-SiC:H film was deposited by PECVD using a Novellus Concept One [15]. In Fig. 2.2 we present a schematic of the PECVD deposition process. The T_{sub} was the only parameter that was varied among the a-Si:H samples. The a-Si:H films have an estimated thickness of 250 nm, and the a-SiC:H film has an estimated thickness of 260 nm. The thicknesses were estimated based on the previously recorded deposition rates for these deposition recipes. The deposition parameters and deposition rates are listed in Table 2.1. We deposited the films on crystalline silicon (c-Si) substrates with (100) crystal orientation. Further substrate details depend on the subsequent experiment, and are described in the methods of each experiment.

Table 2.1: The PECVD deposition parameters and the deposition rates for the films which we investigated in this chapter.

Material	a-Si:H 100°C / 250°C / 350°C	a-SiC:H
T_{sub} (°C)	100 / 250 / 350	400
RF power (W)	15	450
LF Power (W)	-	150
SiH_4 flow (sccm)	25	25
Ar flow (sccm)	475	-
CH_4 flow (sccm)	-	411
Pressure (Torr)	1	2
Deposition rate (nm/s)	0.42 / 0.58 / 0.60	1.43

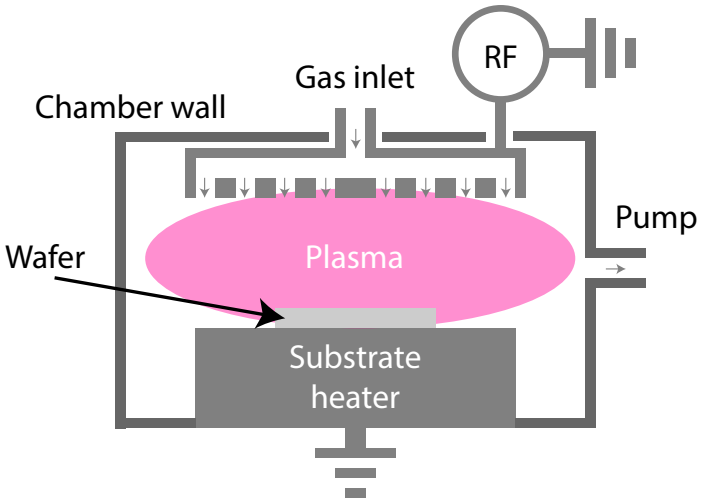

Figure 2.2: Schematic of a PECVD deposition tool. The gas inlet allows various precursor gasses, with controlled gas flows, to flow into the deposition chamber. An RF voltage is applied to the top electrode, thereby ionizing the gas inside the deposition chamber and creating a reactive plasma. The plasma reacts with the substrate, which causes film growth on top of the substrate. The substrate temperature T_{sub} can be controlled using a substrate heater.

2.3. Residual film stress

The film stress is an important film property for device fabrication, since stress can cause peeling of the deposited films. We measured the residual stress of the films using a laser deflection stress measurement system (FLX Flexus). The system moves a laser beam over the wafer along an axis parallel to the wafer surface. A position-sensitive photo diode is used to measure the deflection of the laser beam by the wafer. In this way the system determines the radius of curvature of the wafer along this axis. We performed the deflection measurement before and after the deposition of the films, and we calculated the stress σ using the Stoney equation [16]:

$$\sigma = \frac{E_{\mathrm{s}}}{6(1-\nu_{\mathrm{s}})} \frac{t_{\mathrm{s}}^2}{t_{\mathrm{f}}} \left(\frac{1}{R} - \frac{1}{R_0} \right), \tag{2.1}$$

where the subscripts s and f denote the substrate and the deposited film respectively, E is the Young's modulus ($E_{\mathrm{s}} = 130$ GPa), v is the Poisson's ratio

($\nu_s = 0.28$), t is the thickness, R_0 is the radius of curvature before deposition and R is the radius of curvature after deposition.

The resulting stress values are listed in Table 2.2. For the a-Si:H, we observe a decrease in σ from positive (tensile) to negative (compressive) with increasing T_{sub}. The a-Si:H film that was deposited at a T_{sub} of 350°C had a large residual stress of -379 MPa and exhibited many blistering defects, making this film impractical for fabrication (Fig. 2.3). Interestingly, the a-SiC:H exhibits a low stress value and no blistering defects even when depositing at a high T_{sub} of 400°C.

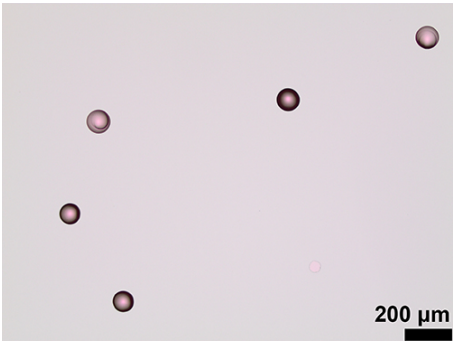

Figure 2.3: The micrograph shows blistering defects which were present in the a-Si:H film that was deposited at a T_{sub} of 350°C, making this film impractical for fabrication.

Table 2.2: The measured residual stress σ of the a-SiH films and of the a-SiC:H film (a positive number means tensile stress).

Material	a-Si:H 100°C	a-Si:H 250°C	a-Si:H 350°C	a-SiC:H
σ (MPa)	129	3	-379	-20

2.4. Fourier-transform infrared spectroscopy

2.4.1. Experimental method

We measured the Fourier-transform infrared (FTIR) transmission of the three a-Si:H films and of the a-SiC:H film (Section 2.2) in the wavenumber range of 500–3000 cm^{-1} (15–90 THz). The FTIR measurement provides us with the complex infrared refractive index $\hat{n}$ of the deposited dielectrics:

$$\hat{n} \equiv n + ik, \tag{2.2}$$

where the real part n is the refractive index and the imaginary part k is the extinction coefficient. In Fig. 2.4 we present a schematic which explains the FTIR instrument's working principle.

We performed the measurements using a Thermo Fischer Nicolet FTIR system with a resolution of 4 cm^{-1}. The sample chamber was continuously purged with nitrogen prior to and during the measurements. We performed measurements with the sample as well as reference measurements without a sample. We determined The FTIR transmission by dividing the measured intensity of the sample measurements by the measured intensity of a reference measurement without a sample. To be able to interpret the data we modeled the FTIR transmission using the transfer-matrix method (TMM) (Appendix A), thereby allowing us to extract the $\hat{n}$ of the deposited dielectrics. The TMM models of the samples include the deposited dielectric film and the c-Si substrate. Prior to the sample measurements we performed an FTIR measurement of a blank c-Si substrate (Appendix B) to obtain the substrate's $\hat{n}$ that we included in the model.

For the fabrication of the FTIR samples we used 500-μm-thick double-side-polished (DSP) p-type c-Si substrates with resistivity $\rho > 1$ kΩ cm. The substrates were dipped in 1% hydrofluoric acid for one minute prior to film deposition. The deposition details are presented in Section 2.2.

2.4.2. Film transmission spectra

In Fig. 2.5 we present the measured FTIR transmission of the a-SiC:H sample and of the three a-Si:H samples. The decrease in transmission of the a-Si:H samples with increasing T_{sub} in the wavenumber ranges without absorption modes (e.g. around 2500 cm^{-1}) can be explained by an increase in reflection due to a monotonic increase in n (and a relatively small n for the a-SiC:H

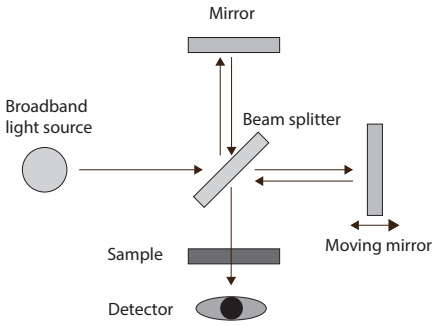

Figure 2.4: Illustration of an FTIR spectrometer. The moving mirror changes the path length of one of the two split beams. Therefore, the recombined beam which goes through the sample and which reaches the detector has an altered intensity, depending on the wavelength and the mirror displacement. The intensity versus displacement data is Fourier-transformed to obtain the intensity versus wavenumber data, thereby generating the FTIR intensity spectrum. A measurement without a sample in place is used as a reference measurement. Finally, the FTIR transmission is calculated by dividing the sample measurement by the reference measurement.

compared to the a-Si:H). The absorption features of the c-Si substrate (Fig. B.2 in Appendix B) have a strong effect on the transmission spectrum in the wavenumber range of roughly 500–1500 cm^{-1}. In Fig. 2.6 we plotted the FTIR sample transmission divided by the FTIR transmission of the substrate, to show the absorption features of the deposited dielectrics. In Fig. 2.6, for the a-Si:H we observe a temperature dependence of the absorption features near 640 cm^{-1} and near 2000–2100 cm^{-1}. The implications of this observation in the context of TLS loss are discussed in Section 2.4.5. Furthermore, in Fig. 2.6 we observe for the a-SiC:H that the infrared absorption is dominated by the Si-C stretching modes near 750 cm^{-1}, compared to the absorption of the a-Si:H films which is dominated by the Si-H_x modes near 640 cm^{-1}.

Implications for the mm-submm loss of a-Si:H and a-SiC:H

The FTIR transmission spectra are interesting in the context of the mm-submm loss, since we hypothesized that the absorption tail of the infrared vibrational modes causes the mm-submm loss in the a-Si:H and a-SiC:H. The dependence of the intensity of the Si-H_x absorption band near 640 cm^{-1} on T_{sub} suggests that the a-Si:H could be optimized for low mm-submm loss by

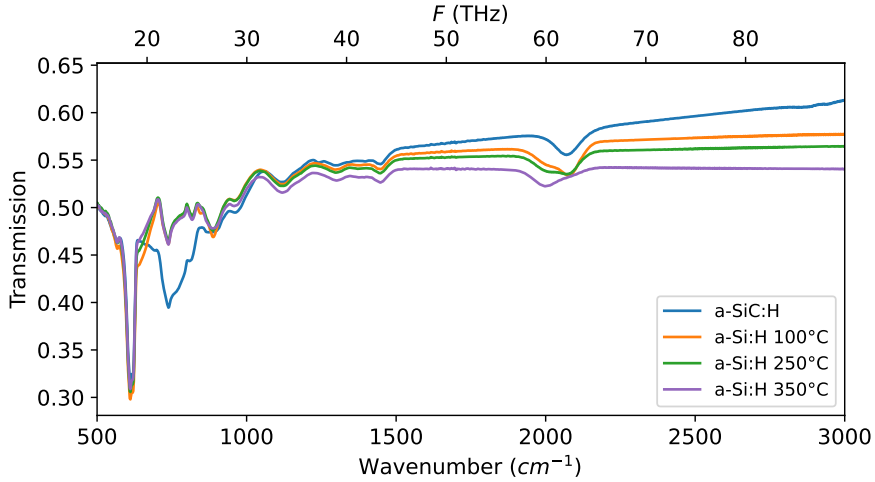

Figure 2.5: The measured FTIR transmission of the a-Si:H samples and of the a-SiC:H sample. The legend indicates the T_{sub} value during deposition. The absorption features of the substrate are visible in the transmission spectrum. In Fig. 2.6 we plotted the sample transmission divided by the substrate transmission.

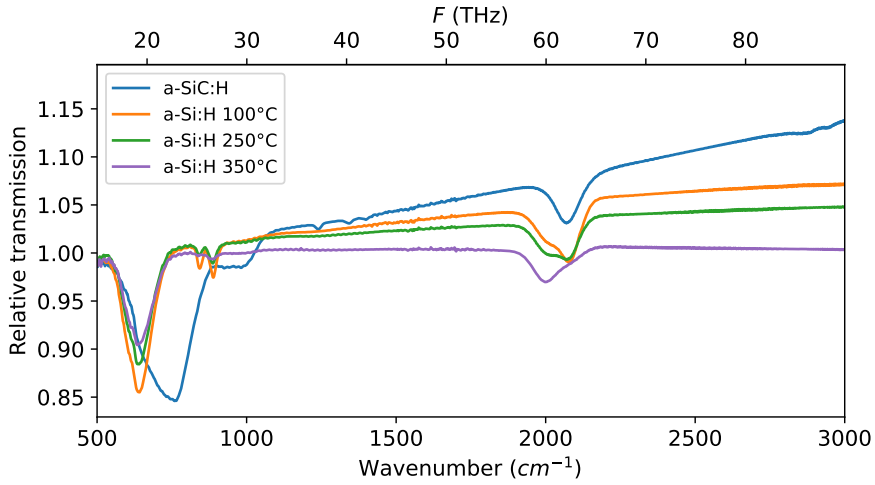

Figure 2.6: FTIR transmission of the a-Si:H films and of the a-SiC:H film, divided by the substrate transmission. The legend indicates the T_{sub} value during deposition.

depositing films at high T_{sub}. However, for our films the deposition at elevated T_{sub} resulted in blistering defects and high compressive stress values (Section 2.3) which makes it difficult to fabricate devices with the 350°C a-Si:H.

For the a-SiC:H, it is interesting that the infrared absorption is dominated by the Si-C stretching modes near 750 cm^{-1}, instead of by the Si-H_x absorption band near 640 cm^{-1}. We note that the absorption band near 640 cm^{-1} in the a-SiC:H was expected to be small in comparison with the 100°C a-Si:H and 250°C a-Si:H samples for two reasons: (1) The very high T_{sub} of 400°C of the a-SiC:H, while achieving a low stress value and no blistering defects, was expected to lead to a small void volume fraction and therefore a low hydrogen content; (2) In a-SiC:H only a fraction of the hydrogen bonds contributes to the Si-H_x absorption near 640 cm^{-1}, since a fraction of the hydrogen in a-SiC:H is bonded to C atoms. This suggests that for a-SiC:H we could expect relatively low mm-submm losses due to a relatively weak Si-H_x absorption band. The absorption band near 750 cm^{-1} due to Si-C stretching modes is further away in frequency from the mm-submm frequency range, and therefore at mm-submm frequencies the absorption tail of this band is expected to be attenuated more in comparison with the absorption tail of the Si-H_x absorption band near 640 cm^{-1}. These observations suggest the a-SiC:H could be optimized for lower mm-submm losses by decreasing the intensity of the Si-C stretching modes, for example by increasing the Si/C ratio (measured in Section 4.2) of the a-SiC:H. This could be achieved by decreasing the LF power [15] or by increasing the $\mathrm{SiH_4/CH_4}$ gas flow ratio during the deposition. However, it is not yet clear if this would produce the desired effect since the higher Si/C ratio could lead to an increased intensity of the Si-H_x absorption band near 640 cm^{-1}.

2.4.3. Kramers-Kronig-consistent infrared optical constants

We determined the infrared optical constants n and k of the a-Si:H and the a-SiC:H from the FTIR spectra. For the a-Si:H, subsequent analysis (Subsection 2.4.5) allowed us to determine the C_{H} and the R^* from the optical constants. While determining the optical constants, we took into account that n is related to k (and vice versa) through the Kramers-Kronig (KK) relations. The KK relations imply that n cannot be assumed to be constant over the measured wavelength range. Here we note that for the c-Si substrate the k is much smaller (Fig. B.2 in Appendix B) than in the case of the deposited dielectrics, and therefore in the case of the substrate the constant n was a valid approximation. The KK relations for the complex electric susceptibility $\hat{\chi} \equiv \chi^{'} + i\chi^{''}$ are equivalent to a Hilbert transform, and are given by the set

of equations:

$$\chi^{'}(\omega) = \frac{1}{\pi}\text{p.v.}\int_{-\infty}^{\infty}\frac{\chi^{''}(\omega^{'})}{\omega^{'}-\omega}d\omega^{'}, \qquad \chi^{''}(\omega) = -\frac{1}{\pi}\text{p.v.}\int_{-\infty}^{\infty}\frac{\chi^{'}(\omega^{'})}{\omega^{'}-\omega}d\omega^{'}, \tag{2.3}$$

where the integrals are calculated using the Cauchy principle value (p.v.). Here, the $\hat{\chi} = \hat{\varepsilon}_{\text{r}} - 1$ and $\hat{\varepsilon}_{\text{r}} = (n + ik)^2$, where $\hat{\varepsilon}_{\text{r}}$ is the complex dielectric constant.

We ensured KK consistency of the optical constants by performing an iterative fitting procedure. First, we assumed a constant refractive index value n_0 and we obtained $k_0(\omega)$ by doing a point-by-point fit of a TMM model to the measured FTIR transmission. Subsequently, we determined $n_1(\omega)$ from $k_0(\omega)$ using the KK relations and we did another point-by-point fit to obtain $k_1(\omega)$. We then repeated this procedure until the optical constants converged. We plotted the results of this procedure for the a-SiC:H film in Fig. 2.7 and for the 250°C a-Si:H film in Fig. 2.8.

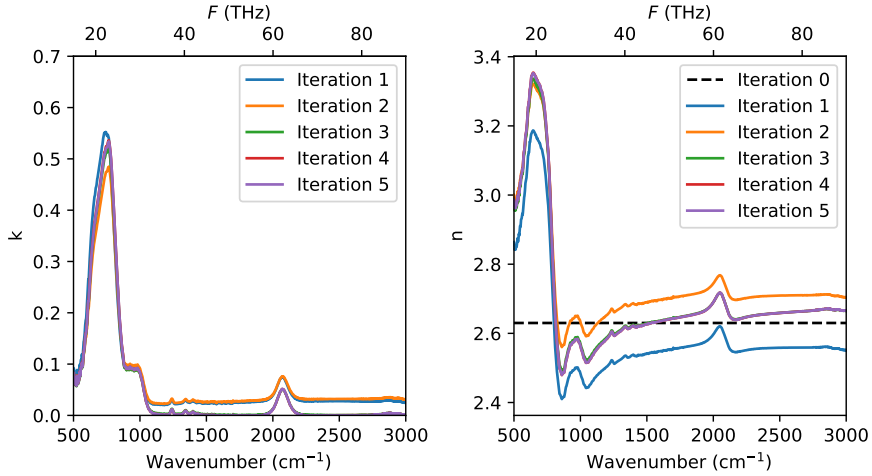

Figure 2.7: Imaginary part k and real part n of the complex refractive index $\hat{n}$ of the a-SiC:H film, obtained from the FTIR measurements by an iterative fitting of the TMM model. The iterative fitting procedure ensures Kramers-Kronig consistency of n and k. Iteration 5 was the final iteration.

In Fig. 2.9 we plotted the infrared refractive index at 3000 cm^{-1} (n_{3000}) of the three a-Si:H films and of the a-SiC:H film. We observe that the n_{3000}

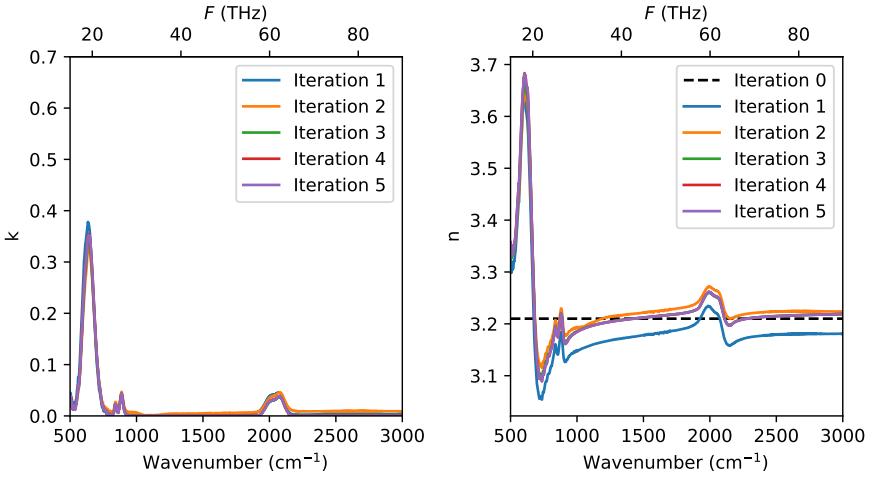

Figure 2.8: Imaginary part k and real part n of the complex refractive index $\hat{n}$ of the 250°C a-Si:H film, obtained from the FTIR measurements by an iterative fitting of the TMM model. The iterative fitting procedure ensures Kramers-Kronig consistency of n and k. Iteration 5 was the final iteration.

of the a-Si:H increases monotonically with increasing T_{sub} and approaches the infrared refractive index of c-Si.

2.4.4. Absorption spectra and fitting of absorption modes

In Fig. 2.10 we plotted the absorption coefficients $\alpha = 4\pi k/\lambda$ of the a-Si:H films in two wavenumber ranges, together with Gaussian fits of the absorption modes. The α values were calculated from the KK-consistent k values of Subsection 2.4.3. The first plotted wavenumber range in Fig. 2.10 contains a Si-H_x absorption peak near 640 cm^{-1}, from which we calculated the hydrogen content C_{H} of the a-Si:H films (Subsection 2.4.5) [7, 12]. The second wavenumber range in Fig. 2.10 contains the SiH and SiH_2 stretching modes near 2000 cm^{-1} and 2100 cm^{-1} respectively, [7], from which we calculated the microstructure parameter R^* of the a-Si:H films (Subsection 2.4.5) [7]. We observe a decrease in the intensity of the absorption peak near 640 cm^{-1} and a decrease in intensity of the stretching mode near 2100 cm^{-1} with increasing T_{sub}. These observations are quantified, and discussed in the context of TLS

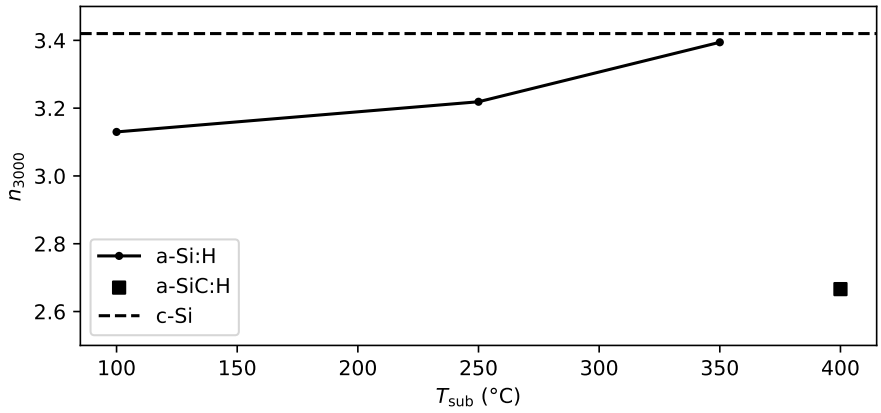

Figure 2.9: The infrared refractive index at 3000 cm^{-1} (n_{3000}) of the three a-Si:H films and of the a-SiC:H film, which we derived from the KK-consistent FTIR analysis. We observe that the n_{3000} of the a-Si:H increases monotonically with increasing T_{sub} and approaches the infrared refractive index of c-Si.

loss, in the subsequent Subsection 2.4.5. In Subsection 2.4.2 we discussed the observed vibrational modes in the context of the mm-submm loss.

In Fig. 2.11 we plotted the absorption spectrum of the a-SiC:H film in frequency bands around 800 cm^{-1} and 2070 cm^{-1}, together with Gaussian fits of the absorption modes. In contrast to a-Si:H, the absorption spectrum of the a-SiC:H below 1000 cm^{-1} is not dominated by the Si-H_x absorption peak around 640 cm^{-1} [14]. In Fig. 2.11 we fitted the spectrum with two Si-C stretching modes near 750 cm^{-1} and a Si-CH_2-Si wagging mode near 980 cm^{-1}. We note that more absorption modes [14], including Si-H_x absorption modes, including the Si-H_x absorption peak near 640 cm^{-1} could be attributed to the a-SiC:H spectrum. However, in our measurements it was not possible to distinguish the Si-H_x absorption peak from the Si-C stretching modes. We observed that the a-SiC:H only exhibits a single SiH_x absorption mode around 2070 cm^{-1}, in contrast to the a-Si:H which exhibits two absorption modes around this wavenumber. In Subsection 2.4.2 we discussed the observed vibrational modes in the context of the mm-submm loss.

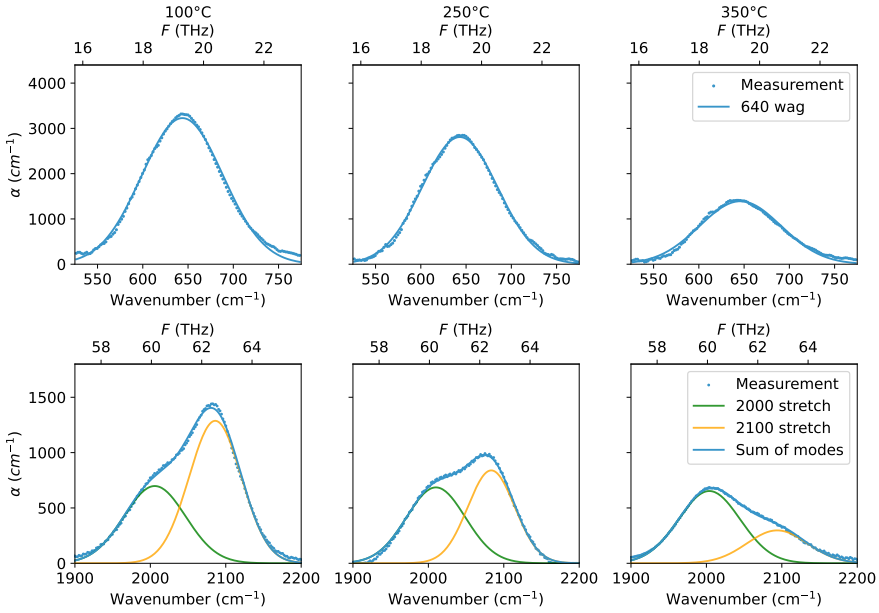

Figure 2.10: The absorption coefficient α of the a-Si:H films, obtained from the FTIR measurements. The different columns show the results for the films that were deposited at T_{sub} of 100°C, 250°C and 350°. The decrease of the intensities of the Si-H$_x$ mode near 640 cm^{-1} and the Si-H$_2$ stretch mode near 2100 cm^{-1} with increasing T_{sub} corresponds with a decrease in the hydrogen content C_{H} and the microstructure parameter R^* respectively (Fig. 2.12).

2.4.5. Hydrogen content and microstructure parameter of a-Si:H

We calculated the hydrogen content C_{H} and the microstructure parameter R^* of the a-Si:H films from the absorption spectra which we presented in Subsection 2.4.4. For this purpose we numerically calculated the integrated absorptions I_x of the absorption modes which we plotted in Fig. 2.10:

$$I_x = \int \frac{\alpha_x(\tilde{\nu})}{\tilde{\nu}} d\tilde{\nu}, \tag{2.4}$$

where x denotes the center wavenumber of the Gaussian absorption peak that is integrated.

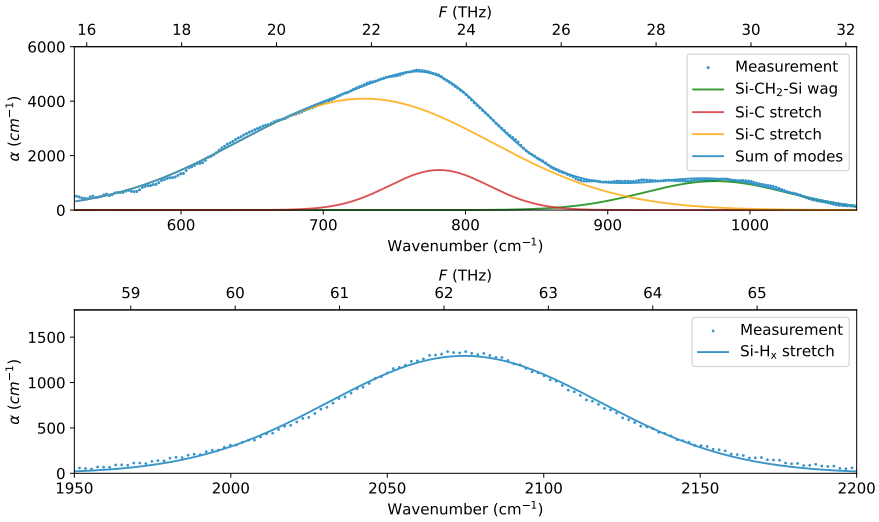

Figure 2.11: Fit of absorption modes to the FTIR absorption spectrum of the a-SiC:H film. We fitted two Si-C stretching modes near 750 cm^{-1}, a Si-CH_2-Si wagging mode near 980 cm^{-1}, and a SiH_x stretching mode near 2070 cm^{-1}.

From the integrated absorption I_{640} of the absorption peak around 640 cm^{-1} we calculated C_H in atomic percent (at. %) [7, 8, 12, 17]:

$$C_H = \frac{A_{640} I_{640}}{A_{640} I_{640} + N_{Si}}, \tag{2.5}$$

where A_{640} is a proportionality constant that is an inverse cross-section for photon absorption at this wavenumber. We used the value $A_{640} = 2.1 \cdot 10^{19}$ cm^{-2} [12]. For N_{Si}, the atomic density of silicon, we used the value $5 \cdot 10^{22}$ cm^{-3}.

The microstructure parameter R^* is defined as [7]:

$$R^* \equiv \frac{I_{2100}}{I_{2100} + I_{2000}}. \tag{2.6}$$

We plotted the results for the C_H and R^* of the three a-Si:H films in Fig. 2.12. We observe that both C_H and R^* decrease monotonically with increasing T_{sub}. The decrease of C_H with T_{sub} is interesting in the context of mm-submm loss caused by infrared absorption, since it is expected that the decrease of the intensity of the absorption peak around 640 cm^{-1} will lead to a decrease in the corresponding absorption tail in the mm-submm wavelength range. The

decrease in R^* indicates a decrease in the fraction of the hydrogen that is bonded in SiH_2 configurations, which suggests a decrease in the number of voids [8]. This is interesting in the context of TLS loss, which can contribute to the microwave as well as mm-submm loss in deposited dielectrics, since it has been suggested in literature that TLSs are related to voids in the dielectric [6].

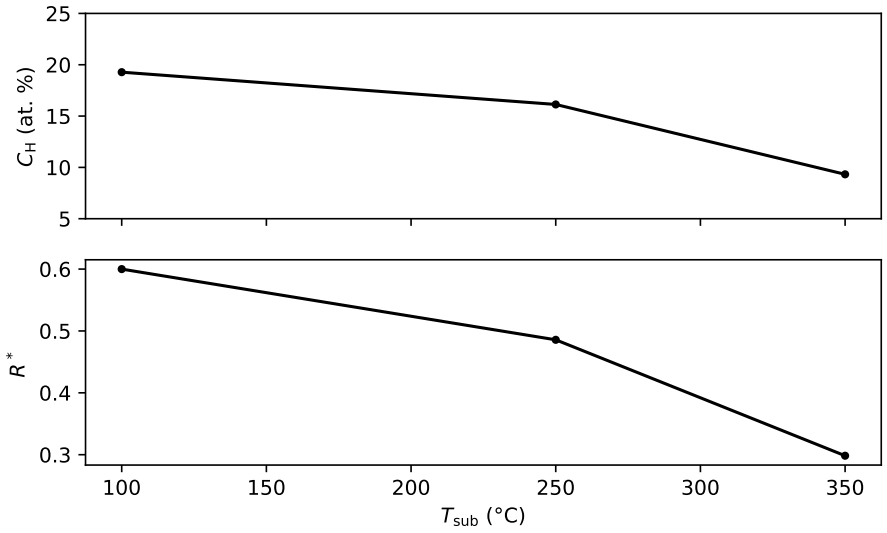

Figure 2.12: The hydrogen content C_H (Eq. (2.5)) and microstructure parameter R^* (Eq. (2.6)) of the a-Si:H films, which we derived from the FTIR analysis. We observe that the C_H and the R^* are monotonically dependent on the substrate temperature T_{sub}.

2.5. Raman spectroscopy

2.5.1. Experimental method

The Raman active modes can be probed by shining visible light on a sample, and measuring the frequency of the inelastically scattered light. In Fig. 2.13 we present a schematic which explains the Raman measurement's working principle.

We performed the Raman measurements using a Renishaw inVia, with a 514-nm (green) laser. We deposited the a-Si:H films and the a-SiC:H film on single side polished (SSP) n-type substrates with a resistivity ρ of 1–5 Ω cm, and with a 101-nm thick thermal oxide layer between the deposited films and the c-Si.

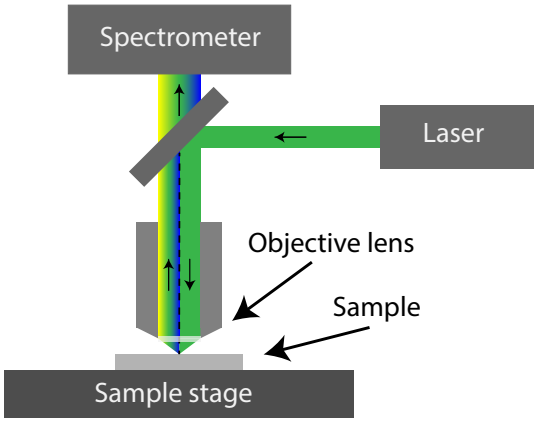

Figure 2.13: Illustration of the Raman spectroscopic instrument. The sample stage can be moved in three dimensions via an external controller. By moving the stage in the vertical direction, the laser can be focused on the sample. The light is inelastically scattered due to Raman scattering, and the difference in wavelength is measured. The wavelength difference corresponds to the excitation energy of an infrared vibrational mode.

2.5.2. Raman spectra and identification of modes

In Fig. 2.14 we plotted the measured Raman spectrum of the a-Si:H film deposited at 250°C, and the Gaussian fits. In addition to the transverse-optical (TO) mode near 480 cm^{-1} (TO 480), we observe a transverse-acoustic (TA) mode near 170 cm^{-1} (TA 170) [18], a longitudinal-acoustic mode near 300 cm^{-1} (LA 300) [19], a longitudinal-optical mode near 425 cm^{-1} (LO 425), and at 520 cm^{-1} the TO mode of the c-Si substrate, fitted with a Lorentzian [13, 20]. The peak near 620 cm^{-1} can be attributed to a variety of modes [19–22], such as the second order 2LA mode and the Si-H_x rocking and wagging modes [22]. In our fitting we fixed the peak position of the LA 300 mode at 300 cm^{-1}.

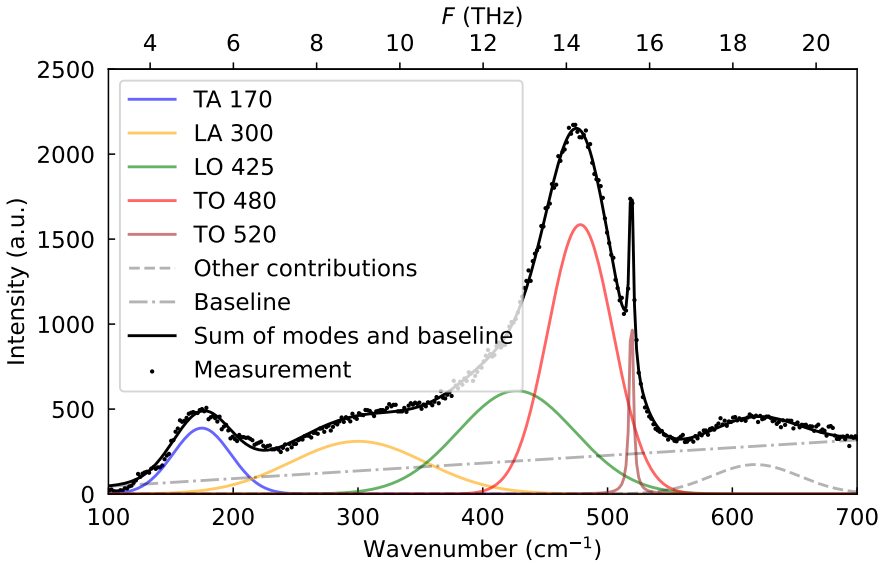

Figure 2.14: Raman spectrum of the 250°C a-Si:H film. We observe a TO mode near 480 cm^{-1}, TA mode near 170 cm^{-1}, LA mode near 300 cm^{-1}, LO mode near 425 cm^{-1}, and at 520 cm^{-1} the TO mode of the c-Si substrate. The spectrum is typical for a fully amorphous film. We note that the intensity is in arbitrary units (a.u.), and therefore only comparisons of relative peak heights can be made within the same spectrum.

In Fig. 2.15 we show the fitted Raman spectrum of the a-SiC:H film. The a-SiC:H exhibits the Raman modes that are also present in the a-Si:H films [22], and we used the same fitting procedure as we used for the a-Si:H films. We observe that the TO 480 mode of the a-Si:H is much more prominent than for the a-SiC:H, relative to the other Raman modes. The Raman spectra of the three a-Si:H films as well as of the a-SiC:H film are typical for fully amorphous materials [13, 22].

2.5.3. Bond-angle disorder of a-Si:H

We calculated the bond-angle disorder $\Delta\theta$ of the a-Si:H films from the Raman spectra. The $\Delta\theta$ is defined as the root mean square deviation from the

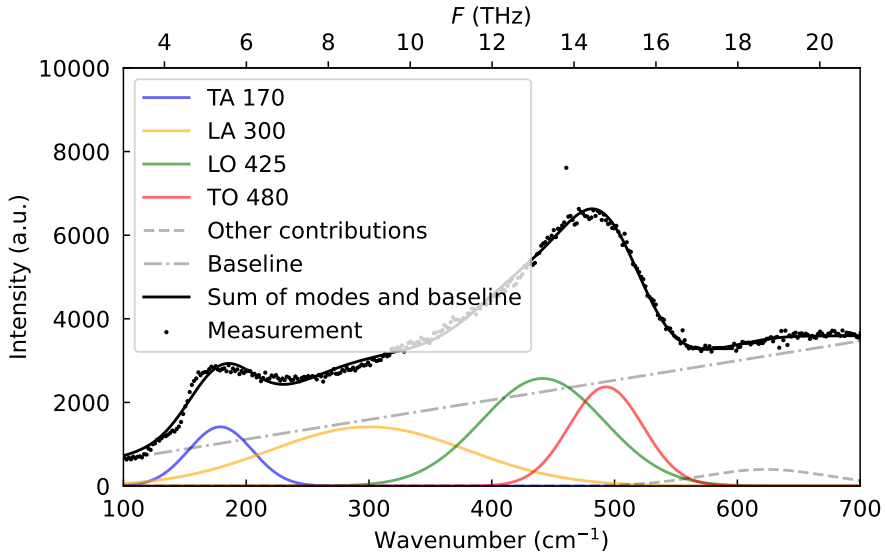

Figure 2.15: Raman spectrum of the a-SiC:H film. We observe a TO mode at near 480 cm^{-1}, TA mode near 170 cm^{-1}, LA mode near 300 cm^{-1}, and the LO mode near 425 cm^{-1}. The spectrum is typical for a fully amorphous film. We note that the intensity is in arbitrary units (a.u.), and therefore only comparisons of relative peak heights can be made within the same spectrum.

tetrahedral bond angle of 109.5° within the silicon network [13]:

$$\Delta\theta = \frac{505.5 - \tilde{\nu}_{\mathrm{TO}}}{2.5}, \tag{2.7}$$

where $\tilde{\nu}_{\mathrm{TO}}$ is the center wavenumber of the TO 480 mode. We plotted the measured $\Delta\theta$ of the three films in Fig. 2.16. We observe a monotonic decrease of $\Delta\theta$ with increasing T_{sub}.

2.6. Ellipsometry

2.6.1. Experimental method

We determined the films' complex dielectric constants $\hat{\varepsilon}$ and band gaps E_{g} using variable-angle spectroscopic ellipsometry in the frequency range of 242–

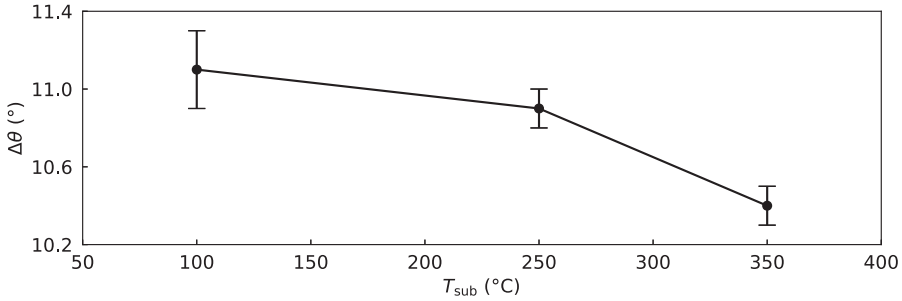

Figure 2.16: The bond-angle disorder $\Delta\theta$ of the three a-Si:H films that we derived from the Raman spectroscopy measurements. The films were deposited at the substrate temperature T_{sub}. The error bars represent the standard deviations of $\Delta\theta$ that we estimated from the least-squares fit.

967 THz (energy range of 1–4 eV). Ellipsometry measures the change of the polarization of the light beam which is reflected off the sample, and it can be used to measure the $\hat{\varepsilon}$ if the film thickness is known, or vice versa. In Fig. 2.17 we show a schematic that demonstrates the working principle of the ellipsometer. The ellipsometry measurement data is commonly given as the parameters ψ and Δ, which are defined as:

$$\psi \equiv \tan^{-1}\left(|r_{\mathrm{p}}/r_{\mathrm{s}}|\right), \qquad \Delta \equiv \mathrm{phase}\left(-r_{\mathrm{p}}/r_{\mathrm{s}}\right), \tag{2.8}$$

where the r are the complex Fresnel reflection coefficients and where the subscripts denote the polarization. We measured ψ and Δ at angles of incidence θ (Fig. 2.17) in the range of 45°–75° in increments of 5°. The ellipsometry parameters can be calculated using the TMM, which is described in Appendix A. We fitted the measured change in polarization to an optical model that includes a native oxide layer, the a-Si:H or a-SiC:H film, a thermal oxide layer, and the c-Si substrate. We performed the analysis using the commercial software CompleteEASE [23]. We fitted the ψ and Δ curves for all θ values together in a single fitting procedure.

We deposited the a-Si:H films and the a-SiC:H films that we used for the ellipsometry measurements on single-side-polished (SSP) n-type substrates with a ρ of 1–5 Ω cm, with a 101-nm thick thermal oxide layer between the deposited films and the c-Si for increased reflection.

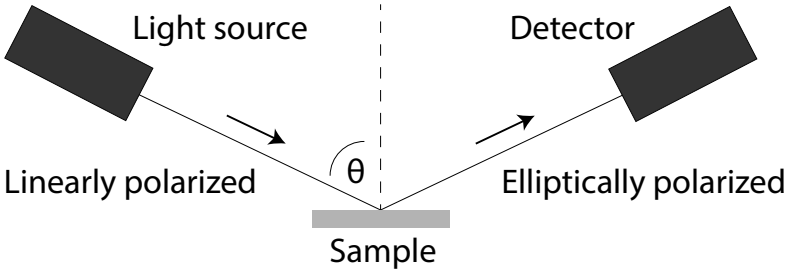

Figure 2.17: Illustration of an ellipsometry setup. The measurement is taken at multiple wavelengths and angles of incidence θ. The reflected beam has undergone a change in intensity and polarization, which can be modeled using the TMM in combination with dispersion models to obtain the film properties.

2.6.2. Fitting of Tauc-Lorentz model to determine the complex dielectric constant and the band gap of the a-SiC:H and a-Si:H

We fitted the ellipsometry data of the a-Si:H films and of the a-SiC:H film using the Tauc-Lorentz dispersion model to obtain the band E_{g} and the n of the a-Si:H and of the a-SiC:H. To give an indication of the small fitting errors, we plotted the fits to the raw ψ and Δ data in Appendix C. The $\varepsilon^{''}$ in the Tauc-Lorentz dispersion model equals [24]:

$$\varepsilon^{''} = \frac{AE_0B\left(E-E_{\mathrm{g}}\right)^2}{\left(E^2-E_0^2\right)^2+B^2E^2}\frac{1}{E}, \qquad E > E_{\mathrm{g}}, \tag{2.9}$$

$$\varepsilon^{''} = 0, \qquad E < E_{\mathrm{g}}, \tag{2.10}$$

where A is the amplitude parameter, B is the broadening parameter, and E_0 is the resonant frequency of the oscillator. The real part $\varepsilon^{'}$ is also defined by Eq. (2.9), since the Tauc-Lorentz model is Kramers-Kronig consistent [24].

We present the resulting complex dielectric constant $\hat{\varepsilon}$ in Fig. 2.18. The band gaps of the a-SiC:H and the a-Si:H films all are in the 1.7–1.8 eV range. Here we note that the relatively high band gap of the a-Si:H compared to the c-Si band gap of 1.1 eV is expected [25]. We observe that the $\varepsilon^{'}$ of the a-Si:H below the band gap increases with increasing T_{sub}, and that below the band gap the a-SiC:H has a relatively small $\varepsilon^{'}$ compared to the a-Si:H.

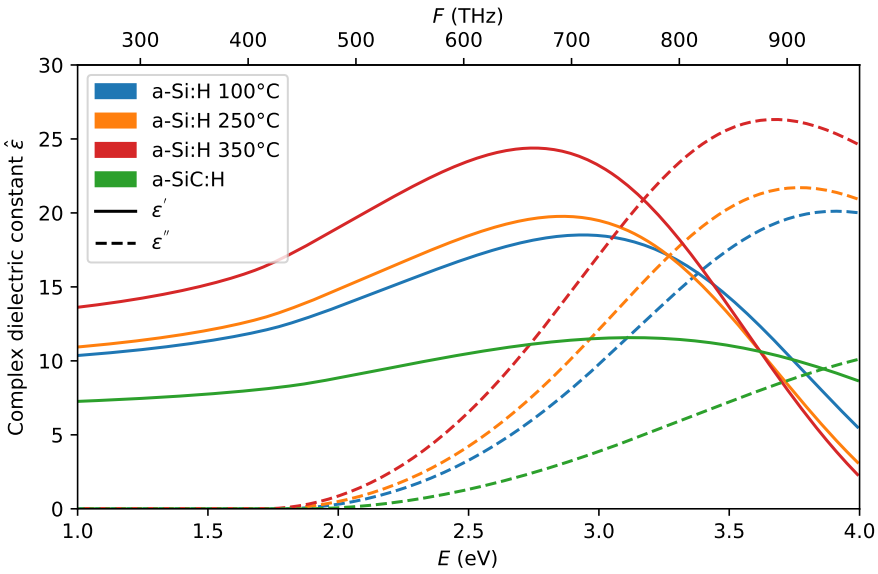

Figure 2.18: The complex dielectric constants $\hat{\varepsilon} = \varepsilon^{'} + i\varepsilon^{''}$ of the a-Si:H films and of the a-SiC:H film resulting from the fitting of the Tauc-Lorentz model to the ellipsometry data.

2.6.3. Void volume fraction of a-Si:H

We obtained the void volume fraction f_v of the a-Si:H films by using the Bruggeman effective medium approximation to model the a-Si:H film as a composite material consisting of a-Si and spherical voids [11]. We plotted the results for f_v in Fig. 2.19. We observe that f_v decreases monotonically with increasing T_{sub}. A decrease in f_v is expected to lead to a decrease in the amount of SiH_2 bonds [8] and therefore a decrease in C_H [7, 17]. This is consistent with the observations in Subsection 2.4.5. It is expected that the decrease in C_H leads to a decrease in the fraction of the mm-submm loss that is caused by the absorption tail due to infrared vibrational modes. Furthermore, the decrease in f_v is expected to lead to decreased TLS loss [6].

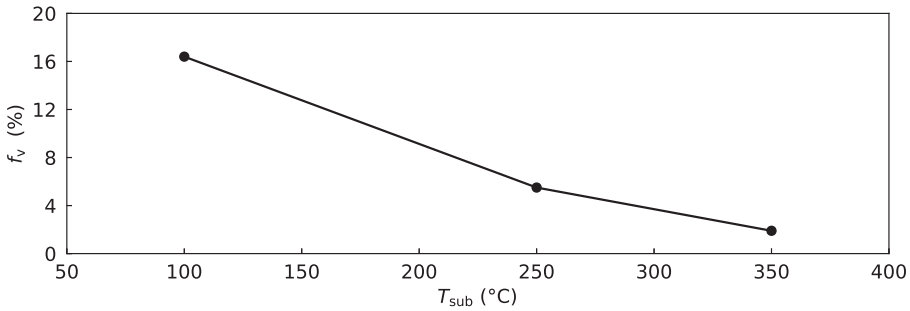

Figure 2.19: The void volume fractions f_v of the three a-Si:H films, that we derived from the ellipsometry data by modeling the a-Si:H layer as a composite material of a-Si and spherical voids using the Bruggeman effective medium approximation. The films were deposited at the substrate temperature T_{sub}.

2.7. Cryogenic microwave loss of a-Si:H

2.7.1. Experimental method

To measure the cryogenic microwave loss of the a-Si:H films, we fabricated superconducting chips with 109 nm thick aluminum (Al) quarter-wavelength CPW resonators on top of the 250 nm thick a-Si:H films. To estimate the losses other than the losses due to the a-Si:H we also fabricated a chip directly on top of a c-Si substrate. The Al layer was patterned using photolithography. We deposited the a-Si:H films on DSP intrinsic c-Si substrates with $\rho > 10$ kΩ cm.

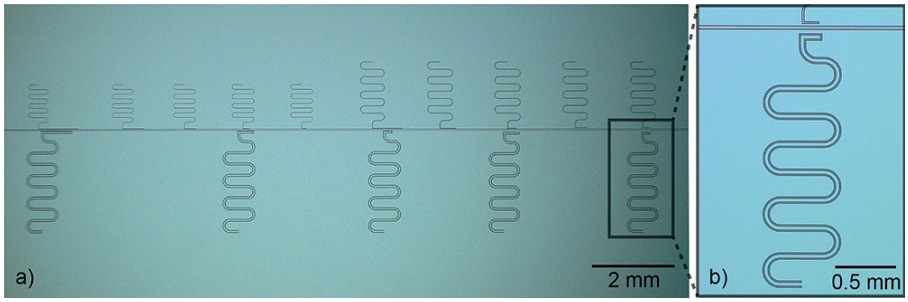

Figure 2.20: a) Micrograph of the superconducting chip. There are three groups of five quarter-wavelength CPW resonators, each group has a different CPW geometry (listed in Table 2.4). Within each group, the resonators vary in the coupling quality factor Q_c. b) Zoomed-in micrograph of the bottom-right resonator in Fig. 2.20a.

The substrates were dipped in 1% hydrofluoric acid for one minute prior to film deposition, with the result that the native oxide of the c-Si was completely removed.

A micrograph of the chip with the 250°C a-Si:H is shown in Fig. 2.20a. The chips feature a CPW readout line with a slot width s of 8 μm and a center line width c of 20 μm. The readout line is coupled to 15 resonators. The resonators are divided into three geometry groups with different s and c. The five resonators within each group have different coupling quality factors Q_c.

	CPW s-c-s (μm)		
Material	2-3-2	6-9-6	18-27-18
c-Si	$2.83 \pm 0.04 \times 10^5$	$2.65 \pm 0.09 \times 10^5$	$1.96 \pm 0.03 \times 10^5$
a-Si 100°C	$1.67 \pm 0.01 \times 10^5$	$2.06 \pm 0.05 \times 10^5$	$2.00 \pm 0.06 \times 10^5$
a-Si 250°C	$1.76 \pm 0.02 \times 10^5$	$3.05 \pm 0.07 \times 10^5$	$3.13 \pm 0.11 \times 10^5$
a-Si 350°C	$3.32 \pm 0.04 \times 10^5$	$2.06 \pm 0.05 \times 10^5$	$2.98 \pm 0.10 \times 10^5$

Table 2.3: The measured coupling quality factors Q_c of the resonators, averaged over all readout powers. The listed uncertainties are the standard deviations in Q_c. In the heading, s is the CPW slot width and c is the CPW center line width.

We obtained the loss tangents $\tan\delta$ of the a-Si:H films at 4–7 GHz and at 120 mK. The cryogenic setup which uses an adiabatic demagnetization refrigerator includes a 35 dB gain low noise (noise temperature of 3-4 K) high-

electron-mobility transistor amplifier at the cryostat's 3-K stage, as well as two amplifiers at room temperature. The 120-mK stage is shielded from magnetic fields using a superconducting lead-tin coated shield that is surrounded by a Cryoperm shield. Further details on the cryogenic setup are given in De Visser's PhD thesis [26]. To derive $\tan\delta$, we measured the S-parameter $S_{21}(f)$ as a function of frequency using a vector network analyzer (VNA). We then obtained $\tan\delta$ from $S_{21}(f)$ by fitting the squared magnitude of the measured $S_{21}(f)$ to a Lorentzian:

$$|S_{21}(f)|^2 = 1 - \frac{1 - S_{21,\min}^2}{1 + \left(2Q\frac{f-f_\mathrm{r}}{f_\mathrm{r}}\right)^2}. \tag{2.11}$$

Here Q is the loaded quality factor, $S_{21,\min}$ is the minimum of the resonance dip, and f_r is the resonance frequency. The internal quality factor Q_i is determined from the equality [26]

$$Q_\mathrm{i} = Q/S_{21,\min}. \tag{2.12}$$

For each geometry group we used the data of the resonator that was designed for the largest $Q_{\mathrm{c,design}} = 3 \times 10^5$, since these have the smallest fitting errors when fitting Eq. 2.11. The measured Q_c values vary between the different resonators in the range of $Q_\mathrm{c} = 1.7$–3.3×10^5 and the values are listed in Table 2.3.

The $1/Q_\mathrm{i}$ can be expressed as:

$$\frac{1}{Q_\mathrm{i}}(g) = p(g)\tan\delta + b(g), \tag{2.13}$$

where g makes it explicit that these quantities are dependent on the CPW geometry. The $p(g)$ is the filling fraction of the a-Si:H film (or the c-Si substrate in the case of the c-Si reference chip), which is the fraction of the resonator's electric energy that is stored inside the dielectric [27]. The $b(g)$ term in Eq. 2.13 represent the sum of all loss mechanisms other than the $\tan\delta$ of the dielectric film.

We calculated the $p(g)$ using the EM-solver Sonnet [28], where we used the ε_mw listed in Table 2.4. The resulting $p(g)$ are visible in Table 2.4.

From the standard tunneling model (STM) it follows that the TLS-induced $\tan\delta$ is dependent on power, frequency, and temperature [5, 27]:

$$\tan\delta = \tan\delta_0 \tanh\frac{\hbar\omega}{2k_BT}\left(1 + \frac{N}{N_0}\right)^{-\beta/2}, \tag{2.14}$$

Material	CPW *s-c-s* (μm) 2-3-2	6-9-6	18-27-18
c-Si ($\varepsilon_{\mathrm{mw}} = 11.44$)	0.920	0.920	0.920
a-Si 100°C ($\varepsilon_{\mathrm{mw}} \approx 9.5$)	0.208	0.101	0.044
a-Si 250°C ($\varepsilon_{\mathrm{mw}} \approx 10.1$)	0.197	0.095	0.042
a-Si 350°C ($\varepsilon_{\mathrm{mw}} \approx 11.2$)	0.214	0.103	0.045

Table 2.4: The filling fractions p of the a-Si:H films that we calculated using the EM-solver Sonnet[28]. In the case of c-Si, the p is calculated for the substrate. The $\varepsilon_{\mathrm{mw}}$ of the a-Si:H films were estimated from their infrared values as $\varepsilon_{\mathrm{mw}} \approx \left(n_{\mathrm{ir}}/n_{\mathrm{cSi,ir}}\right)^2 \varepsilon_{\mathrm{cSi,mw}}$. In the heading s is the CPW slot width and c is the CPW center line width.

where $\tan\delta_0$ is the TLS-induced loss tangent at zero temperature and low internal resonator power, N is the average number of photons inside the resonator, N_0 is the critical photon number above which the TLSs start to saturate, and β is equal to 1 in the STM, but has experimentally been found to range between 0.3 to 0.7 [5]. The frequency ω, the temperature T , and the photon number N are controlled by the experiment. We defined N as the average number of photons per quarter-wavelength, which is equal to $N = P_{\mathrm{int}}/\left(2hf^2\right)$, where P_{int} is the internal resonator power, which can be calculated from the readout power [27].

By equating the losses $b(g)$ from Eq. (2.13) to zero when deriving $\tan\delta$ from $1/Q_{\mathrm{i}}$ we calculated an upper bound of the $\tan\delta$ of the dielectric under consideration. Additionally, we estimated the $\tan\delta$ of the a-Si:H films by equating $b(g)$ to the $1/Q_{\mathrm{i}}$ of the c-Si reference chip.

2.7.2. Loss tangent results

In Fig. 2.21a we plotted the measured Q_{i} versus N of the resonators. We observe that Q_{i} increases with increasing N and that it is dependent on the CPW geometry, even for the c-Si where the filling fraction of the c-Si substrate does not depend on the CPW geometry. The filling fractions of the dielectrics are listed in Table 2.4.

In Fig. 2.21b we show the upper bounds of the $\tan\delta$ of the three a-Si:H films and of the c-Si substrate. The plotted $\tan\delta$ take the filling fractions of the dielectrics into account (Eq. 2.13). We observe that the a-Si:H films have an order of magnitude higher upper bound of $\tan\delta$ than the c-Si substrate. We

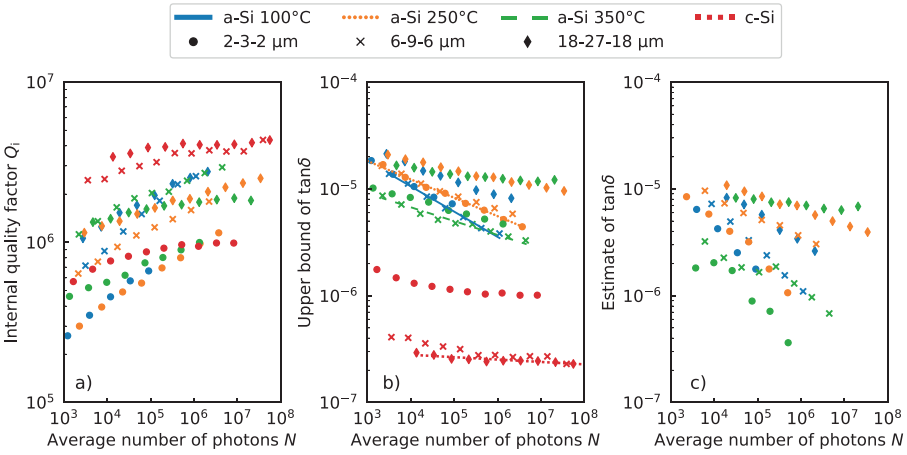

Figure 2.21: a) The measured internal quality factors Q_i of the resonators. The horizontal axis shows the average number of photons in the resonator per quarter-wavelength $N = P_\mathrm{int}/\left(2hf^2\right)$, where P_int is the internal resonator power. b) The upper bounds of $\tan\delta$, which we calculated by equating $b(g)$ in Eq. 2.13 to zero. The lines show the overall upper bounds of the $\tan\delta$ of each material and are fits to a power law. c) The estimates of $\tan\delta$ which were calculated by equating $b(g)$ in Eq. 2.13 to the $1/Q_\mathrm{i}$ of the c-Si reference chip which has resonators directly on top of the c-Si substrate.

did not observe a correlation between T_sub and the upper bound of $\tan\delta$. The upper bounds of $\tan\delta$ vary with the CPW geometry. For each material, the lowest values for the upper bound of $\tan\delta$ represent the overall upper bound, since $\tan\delta$ is independent of geometry. We plotted the overall upper bounds as lines in Fig. 2.21b. These lines are fits to a power law. From the fits we observe that the upper bound of the $\tan\delta$ of the a-Si:H film that was deposited with a T_sub of 100 °C has a steeper slope than the other two a-Si:H films.

The estimates of $\tan\delta$ which we calculated by using the $1/Q_\mathrm{i}$ of the c-Si chip as an estimate for the losses other than the a-Si:H loss are plotted in Fig. 2.21c. We do not observe a correlation between T_sub and the estimate of $\tan\delta$. The estimate of $\tan\delta$ for each material varies with the CPW geometry.

2.7.3. Discussion on the loss tangent results

We did not observe a correlation between $\tan\delta$ and the room temperature properties or T_sub. At the powers at which we measured, a variation in the

low-power TLS-induced loss tangent $\tan\delta_0$ cannot be distinguished from a variation in the critical photon number N_0, above which the TLSs start to saturate. However, if we assume that the three a-Si:H films have identical N_0, then the upper bounds of $\tan\delta$ point to a low-power $\tan\delta_0$ that decreases monotonically with increasing T_{sub}.

For the resonators with a-Si:H, it is expected that the Q_{i} is dependent on the CPW geometry due to differences in the dielectrics' filling fractions (Table 2.4). We observe that the Q_{i} of the c-Si resonators is also dependent on the CPW geometry even though the filling fraction of the c-Si substrate is equal for these resonators. We suggest that this is an effect due to TLS-hosting interface layers [29–32], whose filling fractions and therefore effect on the measured $\tan\delta$ are dependent on the CPW geometry. Furthermore, we suggest that the same effect causes the upper bound and the estimate of $\tan\delta$ to be dependent on the CPW geometry, even though here the filling fractions of the dielectrics have been taken into account. Finally, we note that in reality the c-Si chip is not a perfect reference for the $b(g)$ term in Eq. 2.13, which results in some estimates being higher than the overall upper bound of $\tan\delta$ (the lines in Fig. 2.21b). This discrepancy can be explained by a different metal-dielectric surface, different dielectric-air surface, and an additional surface between the a-Si:H film and the substrate that is not present on the c-Si chip.

The power and frequency range in which we measured is directly applicable to MKIDs, which operate at relatively high powers in comparison with the mm-submm filters that operate at single photon energies. The a-Si:H films are promising for MKID detectors because all three films exhibit an excellent $\tan\delta < 10^{-5}$ at a resonator energy of 10^5 photons per quarter-wavelength, or at –55 dBm internal resonator power.

2.8. Conclusion

We presented extensive material characterization of the a-SiC:H and a-Si:H. From the Raman measurements we observed that the a-Si:H and the a-SiC:H are fully amorphous. A practical benefit of the a-SiC:H film and of the a-Si:H film that was deposited at 250°C is that these films exhibited very low residual stress values. For the a-Si:H we observed that an increase in T_{sub} results in films with less hydrogen, less voids, smaller microstructure parameter, less bond-angle disorder, and higher refractive index. Even though the structural and compositional properties at room temperature of the a-Si:H exhibited a monotonic dependence on T_{sub}, we did not observe a correlation of the room

temperature properties with the cryogenic microwave $\tan\delta$. All three a-Si:H films exhibited a $\tan\delta < 10^{-5}$ at 120 mK and at an average photon number N of 10^5, equivalent to –55 dBm internal resonator power. This makes these a-Si:H films promising for MKID detectors.

The dependence of the intensity of the Si-H_x absorption band near 640 cm^{-1} (19 THz) on T_{sub} suggests that the a-Si:H could be optimized for low mm-submm loss by depositing films at elevated T_{sub}. However, the high compressive stress values and blistering defects of the a-Si:H film that was deposited at a T_{sub} of 350°C make it impractical to fabricate devices with this material. In contrast, the a-SiC:H was deposited at a T_{sub} of 400°C and exhibited a low stress value and no blistering defects. The infrared absorption of the a-SiC:H is mainly caused by Si-C stretching modes near 750 cm^{-1} (22 THz), and the relatively high frequency of these modes is expected to lead to relatively strong attenuation of the absorption tail at mm-submm wavelengths. These findings suggest that a-SiC:H could potentially be optimized for low mm-submm loss by decreasing the intensity of the Si-C absorption band near 750 cm^{-1}. This could be achieved by increasing the Si/C ratio (measured in Section 4.2), by decreasing the LF power [15] or by increasing the SiH_4/CH_4 gas flow ratio during deposition. However, it is not yet clear if this would produce the desired effect since the higher Si/C ratio could lead to an increased intensity of the Si-H_x absorption band near 640 cm^{-1}.

To put this chapter into the context of the most recent literature, we remark that in 2024 there have been reports of low-power microwave losses of a-Si:H films deposited at 350°C: $\tan\delta = 1.2\times10^{-5}$ and $\tan\delta = 7\times10^{-6}$ were reported for films deposited by PECVD and ICPCVD respectively [33]. For future work we recommend to measure the mm-submm and low-power microwave loss of the three a-Si:H films, to investigate if there is a dependence on T_{sub}. In the rest of this dissertation we focus on the a-SiC:H, guided by our measurements of its very low mm-submm losses (Chapter 3).

Bibliography

[1] B. T. Buijtendorp, J. Bueno, D. J. Thoen, V. Murugesan, P. M. Sberna, J. J. A. Baselmans, S. Vollebregt, and A. Endo, "Characterization of low-loss hydrogenated amorphous silicon films for superconducting resonators," *Journal of Astronomical Telescopes, Instruments, and Systems*, vol. 8, June 2022.

[2] A. D. O'Connell, M. Ansmann, R. C. Bialczak, M. Hofheinz, N. Katz, E. Lucero, C. McKenney, M. Neeley, H. Wang, E. M. Weig, A. N. Cleland, and J. M. Martinis, "Microwave dielectric loss at single photon energies and millikelvin temperatures," *Appl. Phys. Lett.*, vol. 92, no. 11, p. 112903, 2008.

[3] B. A. Mazin, D. Sank, S. McHugh, E. A. Lucero, A. Merrill, J. Gao, D. Pappas, D. Moore, and J. Zmuidzinas, "Thin film dielectric microstrip kinetic inductance detectors," *Appl. Phys. Lett.*, vol. 96, no. 10, p. 102504, 2010.

[4] C. Müller, J. H. Cole, and J. Lisenfeld, "Towards understanding two-level-systems in amorphous solids: Insights from quantum circuits," *Rep. Prog. Phys.*, vol. 82, no. 12, p. 124501, 2019.

[5] M. Molina-Ruiz, Y. J. Rosen, H. C. Jacks, M. R. Abernathy, T. H. Metcalf, X. Liu, J. L. DuBois, and F. Hellman, "Origin of mechanical and dielectric losses from two-level systems in amorphous silicon," *Phys. Rev. Mater.*, vol. 5, no. 3, p. 035601, 2021.

[6] D. Queen, X. Liu, J. Karel, H. Jacks, T. Metcalf, and F. Hellman, "Two-level systems in evaporated amorphous silicon," *Journal of Non-Crystalline Solids*, vol. 426, pp. 19–24, Oct. 2015.

[7] J. D. Ouwens and R. E. I. Schropp, "Hydrogen microstructure in hydrogenated amorphous silicon," *Physical Review B*, vol. 54, pp. 17759–17762, Dec. 1996.

[8] A. H. M. Smets, W. M. M. Kessels, and M. C. M. van de Sanden, "Vacancies and voids in hydrogenated amorphous silicon," *Applied Physics Letters*, vol. 82, pp. 1547–1549, Mar. 2003.

[9] W. Beyer, W. Hilgers, P. Prunici, and D. Lennartz, "Voids in hydrogenated amorphous silicon materials," *Journal of Non-Crystalline Solids*, vol. 358, pp. 2023–2026, Sept. 2012.

[10] K. Mui and F. W. Smith, "Optical dielectric function of hydrogenated amorphous silicon: Tetrahedron model and experimental results," *Physical Review B*, vol. 38, pp. 10623–10632, Nov. 1988.

[11] G. Niklasson, C. Granqvist, and O. Hunderi, "Effective medium models for the optical properties of inhomogeneous materials," *Applied Optics*, vol. 20, no. 1, pp. 26–30, 1981.

[12] A. A. Langford, M. L. Fleet, B. P. Nelson, W. A. Lanford, and N. Maley, "Infrared absorption strength and hydrogen content of hydrogenated amorphous silicon," *Physical Review B*, vol. 45, pp. 13367–13377, June 1992.

[13] R. L. C. Vink, G. T. Barkema, and W. F. van der Weg, "Raman spectra and structure of amorphous Si," *Physical Review B*, vol. 63, p. 115210, Mar. 2001.

[14] S. King, M. French, J. Bielefeld, and W. Lanford, "Fourier transform infrared spectroscopy investigation of chemical bonding in low-k a-SiC:H thin films," *Journal of Non-Crystalline Solids*, vol. 357, pp. 2970–2983, July 2011.

[15] P. Sarro, C. de Boer, E. Korkmaz, and J. Laros, "Low-stress PECVD SiC thin films for IC-compatible microstructures," *Sens. Actuator A Phys.*, vol. 67, no. 1-3, pp. 175–180, 1998.

[16] M. R. Ardigo, M. Ahmed, and A. Besnard, "Stoney formula: Investigation of curvature measurements by optical profilometer," *Advanced Materials Research*, vol. 996, pp. 361–366, 2014.

[17] R. Street, *Hydrogenated Amorphous Silicon*. (Cambridge Solid State Science Series), Cambridge University Press, 1991.

[18] D. J. Lockwood and A. Pinczuk, eds., *Optical Phenomena in Semiconductor Structures of Reduced Dimensions*. Dordrecht: Springer Netherlands, 1993.

[19] M. H. Brodsky, M. Cardona, and J. J. Cuomo, "Infrared and Raman spectra of the silicon-hydrogen bonds in amorphous silicon prepared by glow discharge and sputtering," *Physical Review B*, vol. 16, pp. 3556–3571, Oct. 1977.

[20] C. Smit, R. A. C. M. M. van Swaaij, H. Donker, A. M. H. N. Petit, W. M. M. Kessels, and M. C. M. van de Sanden, "Determining the material structure of microcrystalline silicon from Raman spectra," *Journal of Applied Physics*, vol. 94, pp. 3582–3588, Sept. 2003.

[21] P. Mishra and K. P. Jain, "First- and second-order Raman scattering in nanocrystalline silicon," *Physical Review B*, vol. 64, p. 073304, July 2001.

[22] G. Morell, R. S. Katiyar, S. Z. Weisz, and I. Balberg, "Characterization of the silicon network disorder in hydrogenated amorphous silicon carbide alloys with low carbon concentrations," *Journal of Non-Crystalline Solids*, vol. 194, no. 1-2, pp. 78–84, 1996.

[23] Inc. J. A. Woollam Co., "CompleteEASE manual," 2011.

[24] H. Fujiwara and R. W. Collins, eds., *Spectroscopic Ellipsometry for Photovoltaics: Volume 1: Fundamental Principles and Solar Cell Characterization*, vol. 212 of *Springer Series in Optical Sciences*. Cham: Springer International Publishing, 2018.

[25] T. Ibn-Mohammed, S. Koh, I. Reaney, A. Acquaye, G. Schileo, K. Mustapha, and R. Greenough, "Perovskite solar cells: An integrated hybrid lifecycle assessment and review in comparison with other photovoltaic technologies," *Renewable and Sustainable Energy Reviews*, vol. 80, pp. 1321–1344, Dec. 2017.

[26] P. de Visser, *Quasiparticle Dynamicsin Aluminium Superconducting Microwave Resonators*. PhD thesis, 2014.

[27] J. Gao, *The Physics of Superconducting Microwave Resonators*. PhD thesis, California Institute of Technology, 2008.

[28] "Sonnet User's Guide — Sonnet 17."

[29] J. Gao, M. Daal, A. Vayonakis, S. Kumar, J. Zmuidzinas, B. Sadoulet, B. A. Mazin, P. K. Day, and H. G. Leduc, "Experimental evidence for a surface distribution of two-level systems in superconducting lithographed microwave resonators," *Appl. Phys. Lett.*, vol. 92, no. 15, p. 152505, 2008.

[30] J. Wenner, R. Barends, R. Bialczak, Y. Chen, J. Kelly, E. Lucero, M. Mariantoni, A. Megrant, P. O'Malley, D. Sank, A. Vainschencher, H. Wang, T. White, Y. Yin, J. Zhao, A. Cleland, and J. M. Martinis, "Surface loss simulations of superconducting coplanar waveguide resonators," *Applied Physics Letters*, vol. 99, no. 11, p. 113513, 2011.

[31] W. Woods, G. Calusine, A. Melville, A. Sevi, E. Golden, D. Kim, D. Rosenberg, J. Yoder, and W. Oliver, "Determining Interface Dielectric Losses in Superconducting Coplanar-Waveguide Resonators," *Phys. Rev. Appl.*, vol. 12, no. 1, p. 014012, 2019.

[32] R. Barends, N. Vercruyssen, A. Endo, P. J. De Visser, T. Zijlstra, T. M. Klapwijk, and J. J. Baselmans, "Reduced frequency noise in superconducting resonators," *Applied Physics Letters*, vol. 97, no. 3, pp. 2008–2011, 2010.

[33] F. Defrance, A. D. Beyer, S. Shu, J. Sayers, and S. R. Golwala, "Characterization of the low electric field and zero-temperature two-level-system loss in hydrogenated amorphous silicon," *Physical Review Materials*, vol. 8, p. 035602, Mar. 2024.

Chapter 3

a-SiC:H as a low-loss deposited dielectric for mm-submm superconducting circuits

3.1. Introduction

In this chapter we present measurements of the sub-kelvin and low-power dielectric loss of a-SiC:H at microwave (7 GHz) and mm-submm (270–385 GHz) frequencies. Although we identified a-Si:H and a-SiC:H as two promising candidates for low-loss dielectrics (Chapter 2), the cryogenic mm-submm loss and microwave loss of a-SiC:H had not yet been measured. This is in contrast to a-Si:H, for which the work in Chapter 2 has led to co-authorship of an article [2] on a-Si:H film (deposited at T_{sub} of 250°C), where the low-power cryogenic microwave loss ($\tan\delta$=4×10^{-5}) and the cryogenic mm-submm loss at 350 GHz ($\tan\delta$=$2.1 \pm 0.1 \times 10^{-4}$) were measured [2].

3.2. Device fabrication

The losses were measured on chips with superconducting NbTiN/a-SiC:H/NbTiN microstrip resonators, with an identical design for each chip. Fig. 3.1a shows a photograph of one of the chips. The fabrication details for an equivalent chip

This chapter was based on a published article [1].

with a-Si:H instead of a-SiC:H have previously been reported [2]. The NbTiN films were sputter deposited using a Nordiko 2000 [3]. The NbTiN ground plane under the a-SiC:H is 135 nm thick and the NbTiN line on top of the a-SiC:H is 150 nm thick, measured using step profilometry and tilted scanning electron microscopy at the position of the Fabry-Pérot resonators (FP1–4 in Fig. 3.1a).

The 295 nm thick a-SiC:H film was deposited by PECVD using a Novellus Concept One [4, 5]. The deposition parameters are listed in Table 2.1. We patterned the a-SiC:H layer using reactive ion etching with an SF_6 and O_2 plasma at a rate of approximately 0.8 nm/s.

3.3. Dielectric loss measurements

3.3.1. Method for mm-submm loss measurements

The loss measurement device and experimental setup are equivalent to what has been reported for earlier work on a-Si:H [2]. We measured the mm-submm loss at 120 mK by analyzing the transmission through four in-line Fabry-Pérot NbTiN/a-SiC:H/NbTiN microstrip resonators (FP1–4) with 2 μm line width. Each FP is coupled to a NbTiN CPW feed line on one end, and to a hybrid NbTiN-Al microwave kinetic inductance detector (MKID) [6] on the other end, as shown for FP2 in the micrograph in Fig. 3.1b. The FPs' couplers all have an identical design. Fig. 3.1c shows a scanning electron micrograph of the coupling of FP2 to an MKID. Each feed line is connected to a twin slot antenna with a center frequency of 350 GHz, which is located in the focus of a Si-lens glued to the backside of the chip. The antennas receive mm-submm radiation from a Toptica Photonics TeraBeam 1550 continuous-wave photomixer source. The MKIDs are coupled to a shared NbTiN CPW microwave readout line which we read out using a frequency-multiplexed readout system [7].

A schematic of the mm-submm experiment is given in Fig. 1d. The different lengths of the FPs result in different fundamental resonance frequencies f_0. The FPs have transmission peaks at integer multiples (mode numbers n) of f_0. The power that is transmitted through an FP breaks Cooper pairs in the Al section of the MKID, resulting in a change in the MKID's resonance frequency (frequency response) [8]. The frequency response was corrected for stray light by dividing by the response of an MKID that is not connected to an FP (blind MKID in Fig. 3.1a).

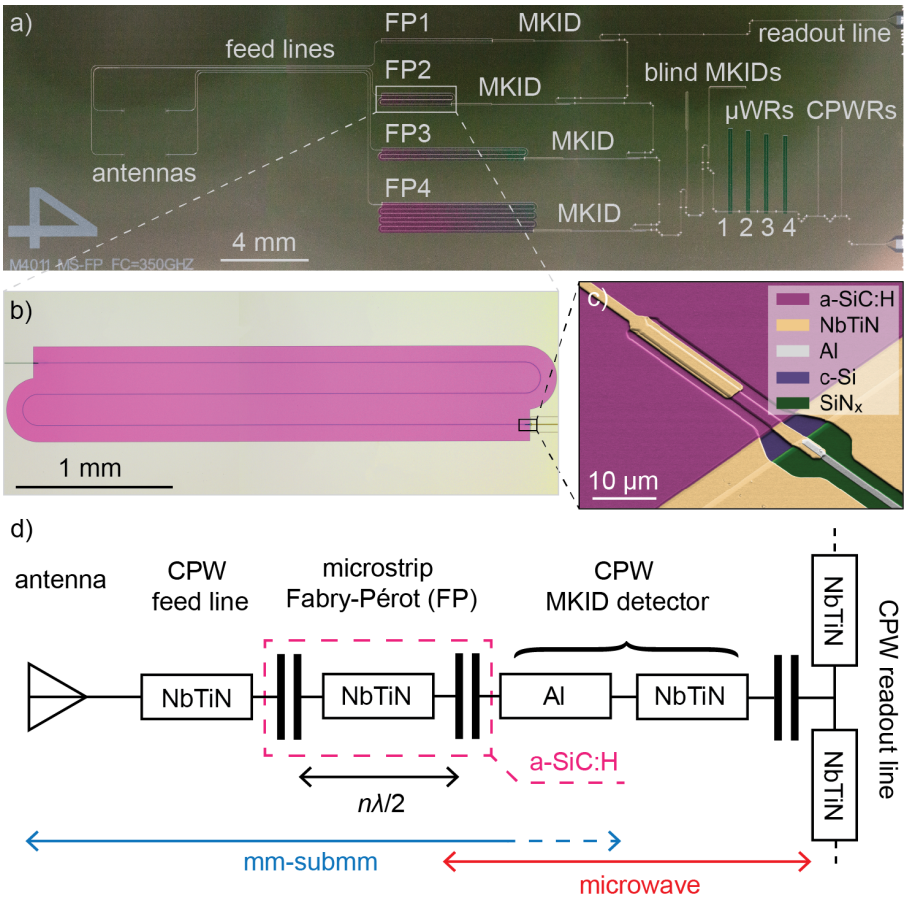

Figure 3.1: a) Photograph of chip 2. The four Fabry-Pérot resonators (FP1–4) receive the mm-submm signal from antennas which receive radiation from a Toptica TeraBeam 1550 photomixer source. Each FP is coupled to an MKID. The four shunted microstrip microwave resonators (μWR1–4) are coupled to the readout line. b) Micrograph of Fabry-Pérot resonator 2 (FP2). The purple area is a-SiC:H. The feed line is visible on the left of the image and the MKID is visible on the right. c) Tilted scanning electron micrograph of the coupling of FP2 to the MKID, with false coloring. d) Schematic of an antenna–FP–MKID circuit. The FPs have a length of an integer (mode number n) multiple of half the mm-submm wavelength λ, and have transmission peaks at nf_0, where f_0 is the fundamental resonance frequency. The mm-submm signal is absorbed in the Al section of the MKID, resulting in a change of resonance frequency (frequency response) of the MKID.

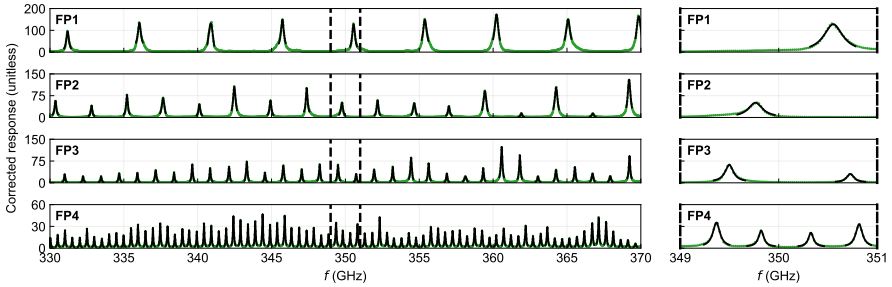

Figure 3.2: The measured frequency response in the 330–370 GHz band for chip 1. The response is measured by the MKIDs that are coupled to the FP1–4. The response is corrected for stray light by dividing by the response of an MKID that is not coupled to an FP (blind MKID in Fig. 3.1a). The green dots represent the measured response, and the black curves are Lorentzian fits to the peaks, from which we obtain the average Q for each FP. The same analysis is performed for each of the four frequency bands. The right plot shows the same data zoomed in to 349–351 GHz.

Since the MKIDs' frequency responses are linear in power[1], they trace the $|S_{21}(f)|^2$ transmission curves of the FPs. The transmission of the mm-submm power through an FP is a sum of Lorentzian peaks [9] and therefore we can obtain the FP's loaded quality factor Q from the transmission peaks as $Q = f_{\mathrm{peak}}/\Delta f$, where f_{peak} is the peak's center frequency and Δf is the peak's full-width at half-maximum.

The frequency response was measured in the 250–400 GHz frequency range by sweeping the photomixer source in steps of 20 MHz. We separated the frequency response data into four bands centered around 270, 310, 350 and 385 GHz to determined the loss of the a-SiC:H at these four frequencies. The frequency bands are shown by the vertical dashed lines in Fig. 3.4.

In each band and for each FP we obtained the average n and the average Q, from which we obtained the internal quality factors Q_{i} by fitting to the equation [2]:

$$Q = \frac{nQ_{\mathrm{c},1}Q_{\mathrm{i}}}{nQ_{\mathrm{c},1} + Q_{\mathrm{i}}}, \tag{3.1}$$

where $Q_{\mathrm{c}} = nQ_{\mathrm{c},1}$ is the FP's coupling quality factor. Here $Q_{\mathrm{c},1} = \pi/|t_{\mathrm{c}}|^2$, with t_{c} the coupler's transmission coefficient. The $\tan\delta$ is obtained from Q_{i}

[1]The measured Fabry-Pérot peaks differ in intensity, corresponding to different mm-submm powers being received by the MKIDs. We observe that the measured Q factors are independent from the powers received by the MKIDs, indicating that the MKIDs' responses are linear within the range of powers in which we performed our measurements.

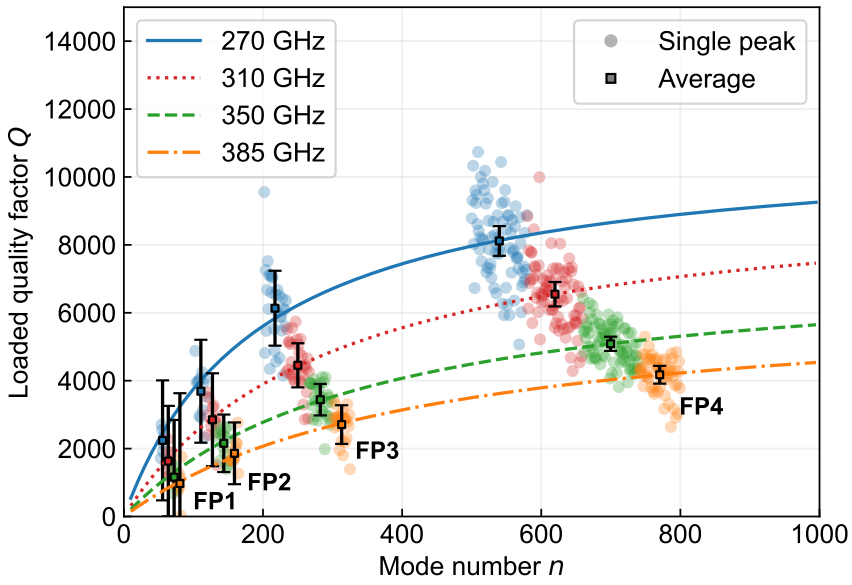

Figure 3.3: Loaded quality factor Q versus mode number n of the Fabry-Pérot resonators (FP1–4) of chip 1. The curves are fits of Eq. 3.1 to the average Q and average n values. The error bars represent 30 standard errors (±30 SE) in Q and the $1/SE$ were used as fitting weights.

as:

$$\tan\delta = 1/(pQ_{\mathrm{i}}), \tag{3.2}$$

where p is the filling fraction [10] of the dielectric, which we determined to be 0.97 in our microstrip resonators using the EM-field solver Sonnet [11].

3.3.2. Mm-submm loss results and discussion

We measured the mm-submm loss of the a-SiC:H on two chips (chips 1 and 2) fabricated on the same wafer. To illustrate the response, we give in Fig. 4.3 the response in the 330–370 GHz band of the four MKIDs behind the four FPs of chip 1. The measured Q versus n and the fits to Eq. 3.1 of chip 1 are shown in Fig. 3.3. An equivalent plot for chip 2 is shown in Fig. F.1 in Appendix F. In the fits of Eq. (3.1) the standard errors in the average Q were used as

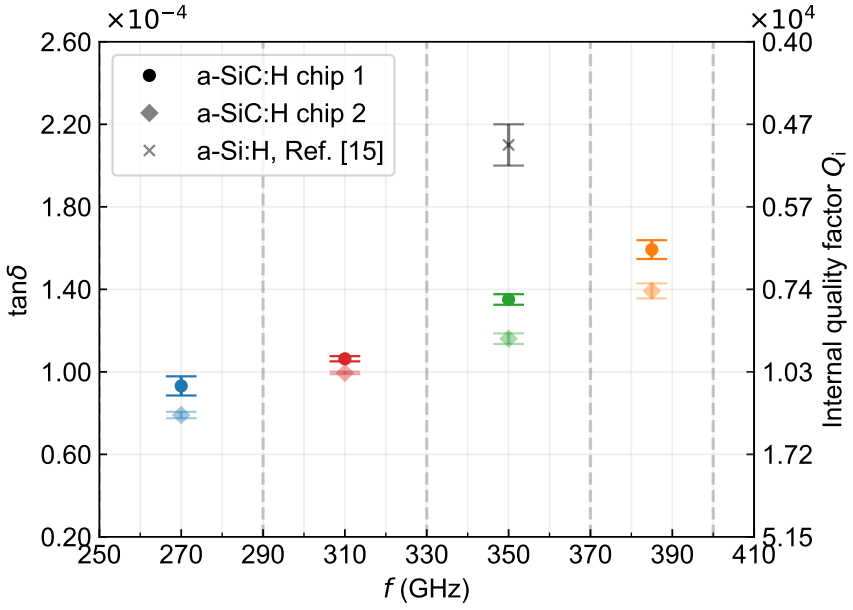

Figure 3.4: The mm-submm $\tan\delta = 1/(pQ_i)$ versus frequency for chips 1 and 2. The error bars represent one standard deviation ($\pm\sigma$). The frequency bands over which Q and n were averaged are displayed by the vertical dashed lines. The a-Si:H loss value at 350 GHz was reported in earlier work and was measured using the same experimental method [2].

fitting weights. In addition to obtaining the Q_i values, from this fit we also obtained the $Q_{\mathrm{c},1}$ values of chips 1 and 2. The measured $Q_{\mathrm{c},1}$ values are given in Fig. F.2 in Appendix F.

The resulting $\tan\delta$ values of chips 1 and 2 are plotted in Fig. 3.4. The mm-submm $\tan\delta$ of the a-SiC:H ranges from 0.9×10^{-4} at 270 GHz to 1.5×10^{-4} at 385 GHz, averaged over chips 1 and 2. These losses are significantly lower than what has been reported for other dielectrics such as a-Si:H [2] and SiN_x [12, 13]. At 350 GHz the a-SiC:H exhibits a $\tan\delta$ of 1.3×10^{-4}, compared with a $\tan\delta$ of 2.1×10^{-4} for a-Si:H, which was measured using the same experimental method [2].

We calculated that the internal mm-submm power $P_{\mathrm{int,FP}}$ circulating inside the FPs is below 1 pW, corresponding to an average number of photons per half-wavelength $N < 1$. We do not observe a significant correlation between $P_{\mathrm{int,FP}}$ and the loss tangent $\tan\delta$ of the a-SiC:H, suggesting that TLS saturation [10, 14] does not affect the mm-submm loss measurements. More information on this calculation is given in Appendix E.

3.3.3. Method for microwave loss measurements

We measured the microwave loss of the of the a-SiC:H on two chips (chips 1 and 3) fabricated on the same wafer, where chip 1 is the same chip as discussed for the mm-submm loss measurements. On each chip, the microwave losses were measured using four NbTiN/a-SiC:H/NbTiN half-wavelength microstrip microwave resonators (μWR1–4 in Fig. 3.1a.) with 2 μm line width, at a temperature of 60 mK. We used a vector network analyzer to measure the S_{21}-parameter of the NbTiN coplanar waveguide (CPW) readout line, which is coupled to the four shunted μWRs. We measured $\tan\delta$ in a range of microwave internal resonator powers P_int, corresponding to an average number of photons per half-wavelength in the resonators N of roughly 10^{-1}–10^{8}. In Appendix D we described the design of a microwave readout chain which allows for measurements at single photon energies. N is equal to:

$$N = P_\mathrm{int} / \left(hf^2\right). \tag{3.3}$$

We fitted the $|S_{21}|$ dips of the four μWRs using the model described in Ref. [15] to obtain the resonators' Q_i, from which we calculated $\tan\delta$ (Eq. 3.2).

3.3.4. Microwave loss results and discussion

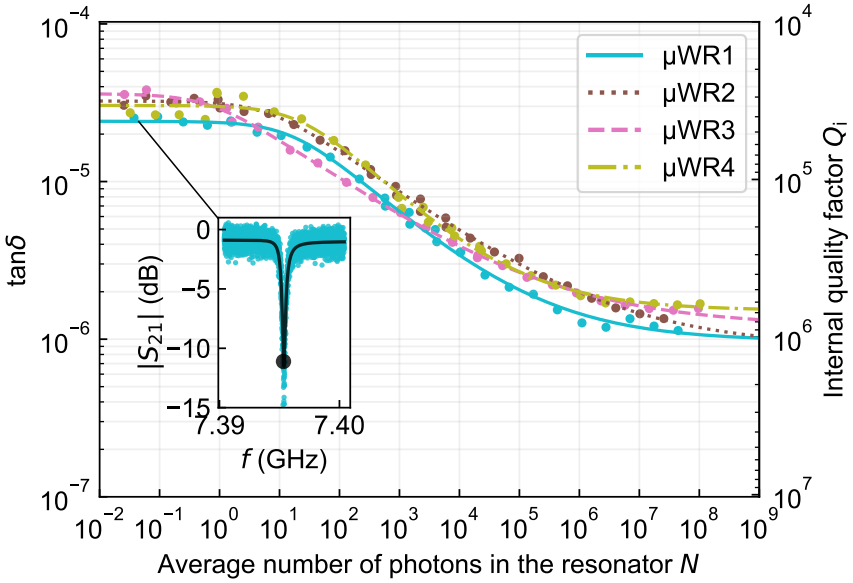

Figure 3.5: Measured microwave $\tan\delta = 1/(pQ_i)$ versus average number of photons in the resonators μWR1–4 of chip 1. The curves are fits to Eq. 4.2. The inset illustrates how $\tan\delta$ is obtained at each power, by fitting the $|S_{21}|$ dips using the model in Ref. [15]. The $\tan\delta_0$ are obtained by fitting the $\tan\delta$ versus N curves to Eq. 4.2.

From Fig. 3.5 we observe that the microwave $\tan\delta$ follows the power dependence predicted by the standard tunneling model (STM) [10, 14]:

$$\tan\delta = \tan\delta_0 \tanh\frac{hf}{2k_BT}\left(1+\frac{N}{N_0}\right)^{-\beta/2} + \tan\delta_{\mathrm{HP}}, \tag{3.4}$$

where f is the frequency, T is the temperature, N_0 is the critical photon number above which the TLSs saturate, and β is equal to 1 in the STM, but it has previously been observed in the range of 0.3–0.7 [2, 16, 17]. The $\tan\delta_{\mathrm{HP}}$ term represents losses other than TLS loss which dominate at high internal resonator power. The $\tan\delta_0$ is the TLS-induced $\tan\delta$ in the low-power limit and at 0 K.

We obtained the microwave $\tan\delta_0$ and β by fitting Eq. 4.2 to the measured $\tan\delta$ versus N. The fits for chip 1 are shown in Fig. 3.5 and the fits for chip 3 are shown in Fig. F.3 in Appendix F. The μWRs of chips 1 and 3 exhibit an average $\tan\delta_0$ of $3.1 \pm 0.4 \times 10^{-5}$. This is comparable to what has been reported for a-Si:H [2, 18, 19]. We measured β values in the range of 0.5–0.8. We confirm that the low-power loss is dominated by the a-SiC:H and not by the NbTiN by measuring a shunted NbTiN CPW quarter-wavelength microwave resonator (CPWR) with a 6 μm center line width and a 16 μm gap width, which was fabricated directly on top of the c-Si substrate ($\rho > 10$ kΩ cm), i.e. without a-SiC:H. The low-power $1/Q_\mathrm{i}$ of $4.1 \pm 0.1 \times 10^{-6}$ of the CPWR is significantly smaller than that of the μWRs.

3.3.5. Discussion on the physical origin of the loss

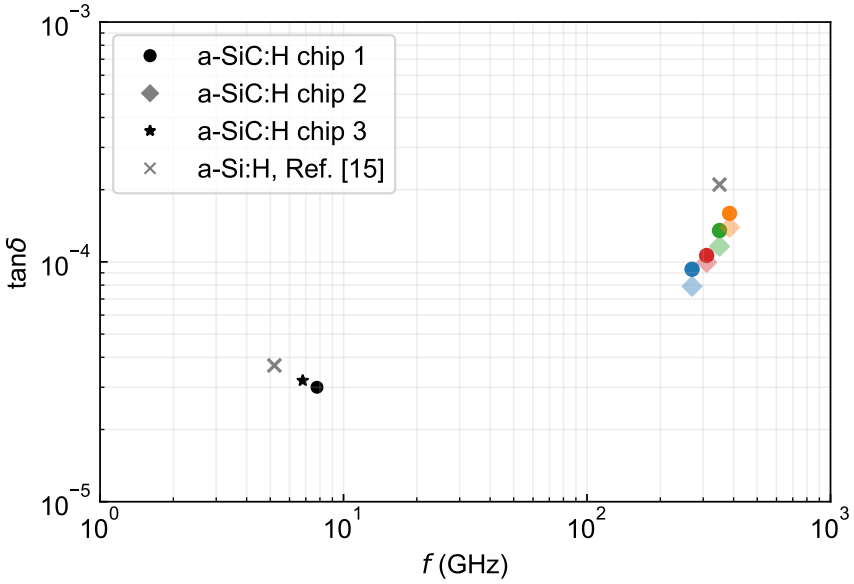

Figure 3.6: Overview of the mm-submm $\tan\delta = 1/(pQ_\mathrm{i})$ values of chips 1 and 2, together with the microwave $\tan\delta_0$ values of chips 1 and 3. The $\tan\delta_0$ values were obtained from Eq. (4.2). The a-Si:H loss value at 350 GHz was reported in earlier work and was measured using the same experimental method [2].

The physical origin of the loss is not yet fully understood. We give an overview of the measured losses in Fig. 3.6, together with data from Ref. [2] on a-Si:H. The microwave loss of the a-SiC:H is well described by the STM for TLSs. However, the significantly larger mm-submm loss than microwave loss as well as the frequency dependence of the mm-submm loss are surprising in the framework of the STM which assumes a frequency independent TLS density of states [14]. We note that a larger mm-submm than microwave loss was also reported for SiN_x [12, 18] and a-Si:H [2, 18]. Although a generalized TLS model with a frequency dependent TLS density of states has been reported [20], from Fig. 3.6 we observe that the mm-submm loss follows a power law dependence which does not extrapolate to the microwave loss value. This leads us to the hypothesis that the mm-submm loss has a different origin than the microwave loss: We suggest that the microwave loss of the a-SiC:H is dominated by TLS loss, whereas the mm-submm loss is dominated by the absorption tail of vibrational modes at far-infrared wavelengths [2, 21, 22].

3.4. Dielectric constant, film uniformity and residual stress

We estimated the sub-kelvin dielectric constant ε_r of the a-SiC:H by comparing the measured resonance frequencies of μWR1–4 and FP1–4 to Sonnet [11] simulations of the microstrips. We find an ε_r of 7.8 ± 0.7, where the uncertainty is due to the non-uniformity and uncertainty in the NbTiN properties across the wafer [3]. Within this uncertainty the microwave and mm-submm ε_r are indistinguishable.

We used ellipsometry to measure a room temperature ε_r of 7.5 at 250 THz (1200 nm) at the wafer's center, with a non-uniformity in $\varepsilon_r < 1$ % within a 3.5 cm radius around the wafer's center. Furthermore, from the ellipsometry measurement we determined the film thickness to be 295 nm at the wafer's center, with a non-uniformity in thickness < 1 %. The excellent uniformity in thickness and dielectric constant suggests that the deposition process of the a-SiC:H is highly uniform across the wafer. From the same ellipsometry measurement, we observe a band gap of 1.8 eV, which we obtained by fitting the Tauc-Lorentz dispersion model to the ellipsometry data in the range of 0.8–2.7 eV.

We determined the residual stress of the a-SiC:H films from the wafer bow before and after deposition on bare c-Si substrates, using the Stoney equation. The wafer bow was measured using a Flexus 2320-S. The a-SiC:H films exhibit

low stress: −20 MPa compressive at 200 nm thickness to 60 MPa tensile at 1000 nm thickness.

3.5. Conclusion

To conclude, PECVD a-SiC:H exhibits the lowest low-power sub-kelvin mm-submm dielectric loss that has been reported to date for microstrip resonators. The microwave loss is comparable to the best values that have been reported for microstrip resonators [2, 19]. In addition to the low loss, the a-SiC:H films are free of blisters, exhibit low stress and have excellent uniformity in terms of the thickness and dielectric constant measured by ellipsometry. These properties make a-SiC:H a promising dielectric for microwave to submm wave superconducting circuits in many applications. However, the origin of the mm-submm loss in the a-SiC:H remains unknown, which is what we investigate in Chapter 4.

Bibliography

[1] B. Buijtendorp, S. Vollebregt, K. Karatsu, D. Thoen, V. Murugesan, K. Kouwenhoven, S. Hähnle, J. Baselmans, and A. Endo, "Hydrogenated Amorphous Silicon Carbide: A Low-Loss Deposited Dielectric for Microwave to Submillimeter-Wave Superconducting Circuits," *Physical Review Applied*, vol. 18, p. 064003, Dec. 2022.

[2] S. Hähnle, K. Kouwenhoven, B. Buijtendorp, A. Endo, K. Karatsu, D. Thoen, V. Murugesan, and J. Baselmans, "Superconducting Microstrip Losses at Microwave and Submillimeter Wavelengths," *Phys. Rev. Appl.*, vol. 16, no. 1, p. 014019, 2021.

[3] D. J. Thoen, B. G. C. Bos, E. A. F. Haalebos, T. M. Klapwijk, J. J. A. Baselmans, and A. Endo, "Superconducting NbTin Thin Films With Highly Uniform Properties Over a ${\varnothing}$ 100 mm Wafer," *IEEE Transactions on Applied Superconductivity*, vol. 27, pp. 1–5, June 2017.

[4] E. P. van de Ven, "Advances In Plasma Enhanced Thin Film Deposition," in *SPIE Advanced Processing Technologies for Optical and ELectronic Devices*, (Santa Clara, CA), p. 117, 1988.

[5] P. Sarro, C. de Boer, E. Korkmaz, and J. Laros, "Low-stress PECVD SiC thin films for IC-compatible microstructures," *Sens. Actuator A Phys.*, vol. 67, no. 1-3, pp. 175–180, 1998.

[6] R. M. J. Janssen, J. J. A. Baselmans, A. Endo, L. Ferrari, S. J. C. Yates, A. M. Baryshev, and T. M. Klapwijk, "High optical efficiency and photon noise limited sensitivity of microwave kinetic inductance detectors using phase readout," *Appl. Phys. Lett.*, vol. 103, no. 20, p. 203503, 2013.

[7] J. van Rantwijk, M. Grim, D. van Loon, S. Yates, A. Baryshev, and J. Baselmans, "Multiplexed Readout for 1000-Pixel Arrays of Microwave Kinetic Inductance Detectors," *IEEE Trans. Microwave Theory Techn.*, vol. 64, no. 6, pp. 1876–1883, 2016.

[8] P. K. Day, H. G. LeDuc, B. A. Mazin, A. Vayonakis, and J. Zmuidzinas, "A broadband superconducting detector suitable for use in large arrays," *Nature*, vol. 425, pp. 817–821, Oct. 2003.

[9] M. Pollnau and M. Eichhorn, "Spectral coherence, Part I: Passive-resonator linewidth, fundamental laser linewidth, and Schawlow-Townes approximation," *Progress in Quantum Electronics*, vol. 72, Aug. 2020.

[10] J. Gao, *The Physics of Superconducting Microwave Resonators*. PhD thesis, California Institute of Technology, 2008.

[11] "Sonnet User's Guide — Sonnet 17."

[12] A. Endo, C. Sfiligoj, S. J. C. Yates, J. J. A. Baselmans, D. J. Thoen, S. M. H. Javadzadeh, P. P. van der Werf, A. M. Baryshev, and T. M. Klapwijk, "On-chip filter bank spectroscopy at 600–700 GHz using NbTiN superconducting resonators," *Appl. Phys. Lett.*, vol. 103, no. 3, p. 032601, 2013.

[13] S. Hailey-Dunsheath, P. S. Barry, C. M. Bradford, G. Chattopadhyay, P. Day, S. Doyle, M. Hollister, A. Kovacs, H. G. LeDuc, N. Llombart, P. Mauskopf, C. McKenney, R. Monroe, H. T. Nguyen, R. O'Brient, S. Padin, T. Reck, E. Shirokoff, L. Swenson, C. E. Tucker, and J. Zmuidzinas, "Optical Measurements of SuperSpec: A Millimeter-Wave On-Chip Spectrometer," *J. Low Temp. Phys.*, vol. 176, no. 5-6, pp. 841–847, 2014.

[14] W. A. Phillips, "Tunneling states in amorphous solids," *J. Low Temp. Phys.*, vol. 7, no. 3-4, pp. 351–360, 1972.

[15] M. S. Khalil, M. J. A. Stoutimore, F. C. Wellstood, and K. D. Osborn, "An analysis method for asymmetric resonator transmission applied to superconducting devices," *J. Appl. Phys*, vol. 111, no. 5, p. 054510, 2012.

[16] C. Müller, J. H. Cole, and J. Lisenfeld, "Towards understanding two-level-systems in amorphous solids: Insights from quantum circuits," *Rep. Prog. Phys.*, vol. 82, no. 12, p. 124501, 2019.

[17] M. Molina-Ruiz, Y. J. Rosen, H. C. Jacks, M. R. Abernathy, T. H. Metcalf, X. Liu, J. L. DuBois, and F. Hellman, "Origin of mechanical and dielectric losses from two-level systems in amorphous silicon," *Phys. Rev. Mater.*, vol. 5, no. 3, p. 035601, 2021.

[18] A. D. O'Connell, M. Ansmann, R. C. Bialczak, M. Hofheinz, N. Katz, E. Lucero, C. McKenney, M. Neeley, H. Wang, E. M. Weig, A. N. Cleland, and J. M. Martinis, "Microwave dielectric loss at single photon energies and millikelvin temperatures," *Appl. Phys. Lett.*, vol. 92, no. 11, p. 112903, 2008.

[19] B. A. Mazin, D. Sank, S. McHugh, E. A. Lucero, A. Merrill, J. Gao, D. Pappas, D. Moore, and J. Zmuidzinas, "Thin film dielectric microstrip kinetic inductance detectors," *Appl. Phys. Lett.*, vol. 96, no. 10, p. 102504, 2010.

[20] L. Faoro and L. B. Ioffe, "Interacting tunneling model for two-level systems in amorphous materials and its predictions for their dephasing and noise in superconducting microresonators," *Phys. Rev. B*, vol. 91, no. 1, p. 014201, 2015.

[21] G. Cataldo, J. A. Beall, H.-M. Cho, B. McAndrew, M. D. Niemack, and E. J. Wollack, "Infrared dielectric properties of low-stress silicon nitride," *Optics Letters*, vol. 37, p. 4200, Oct. 2012.

[22] G. Cataldo, E. J. Wollack, A. D. Brown, and K. H. Miller, "Infrared dielectric properties of low-stress silicon oxide," *Optics Letters*, vol. 41, p. 1364, Apr. 2016.

Chapter 4

Origin of the mm-submm loss in a-SiC:H

4.1. Introduction

In this chapter we present loss measurements of a-SiC:H films in the 0.27–100 THz range, where in the 270–600 GHz range we used superconducting microstrip resonators, and above 3 THz we used Fourier-transform spectroscopy (FTS). The agreement between the loss data and a Maxwell-Helmholtz-Drude (MHD) dispersion model suggests that vibrational modes above 10 THz dominate the loss in the a-SiC:H above 200 GHz.

Although the very low mm-submm loss of the a-SiC:H (Chapter 3) was promising for integrated superconducting astronomical instruments, we had not yet uncovered the origin of the mm-submm loss in the a-SiC:H. In Chatper 3 we observed that the mm-submm loss increases monotonically with frequency. The frequency dependence of the loss is surprising in the framework of the standard tunneling model (STM) for two-level systems (TLSs) [2, 3], which led us to the hypthesis that infrared absorption modes are responsible for the mm-submm loss in a-SiC:H.

This chapter was based on a published article [1].

4.2. Deposition details and material characterization of the a-SiC:H

We deposited the 2.1-μm-thick a-SiC:H films by plasma-enhanced chemical vapor deposition (PECVD) using a Novellus Concept One [4]. All the a-SiC:H films which we measured for this work were deposited together on a total of four c-Si wafers (W1–4). We fabricated the microstrip resonators on W1, and on this wafer we deposited the a-SiC:H on a NbTiN ground layer that was sputter-deposited on the c-Si substrate. On W2–4 we deposited the a-SiC:H directly on the c-Si substrates. Prior to the deposition of the a-SiC:H we removed any native oxide on each wafer with a 10-s 10% HF dip. The deposition parameters are listed in Table 2.1.

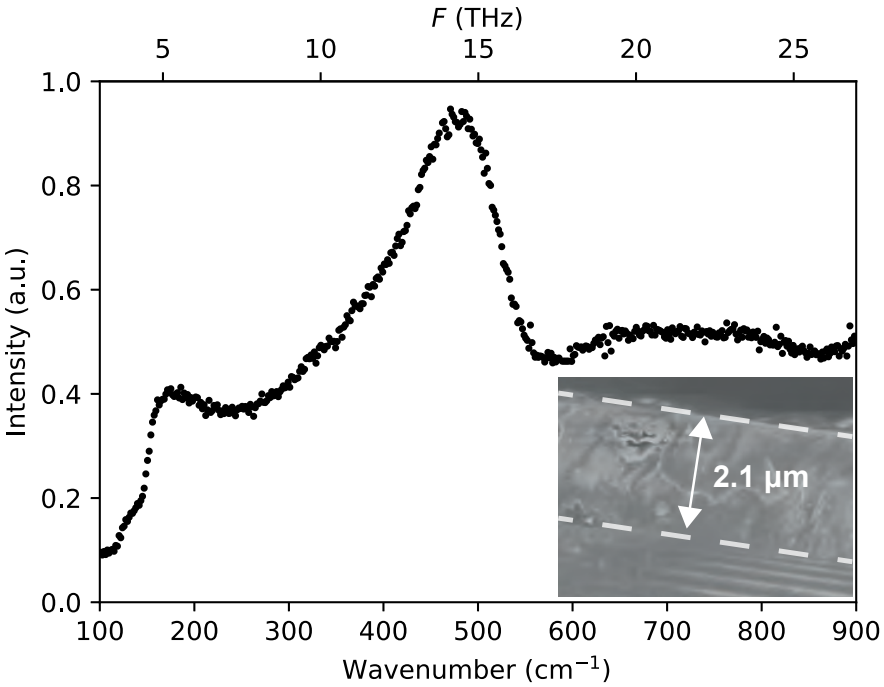

Figure 4.1: Raman spectrum of a 2.1-μm-thick a-SiC:H film on a c-Si substrate. The Raman spectrum is typical for fully amorphous a-SiC:H. The inset shows a scanning electron micrograph of a cleaved c-Si wafer with an a-SiC:H film, from which we determined the film thickness.

We performed several characterization measurements on W2 to determine the material properties of the a-SiC:H films. We verified that the a-SiC:H is fully amorphous by performing Raman spectroscopy with a 514-nm laser. We plotted the Raman spectrum in Fig. 4.1. The spectrum's broadened features are typical for fully amorphous a-SiC:H [5–7]. We determined that the a-SiC:H has an atomic Si/C ratio of 0.8 using energy-dispersive X-ray spectroscopy (EDS). We measured a 2.1-μm film thickness from a scanning-electron micrograph of the cross section of the wafer, as shown in the inset of Fig. 4.1. Finally, we measured a relative dielectric constant $\varepsilon_{\mathrm{r}}^{'}$ of 7.6 at 250 THz and a band gap of 1.8 eV by performing ellipsometry and fitting a Tauc-Lorentz dispersion model [8].

4.3. Far infrared loss, measured in superconducting microstrip resonators

4.3.1. Device design and fabrication

To measure the 270–600 GHz loss of the a-SiC:H we used a lab-on-chip experiment based upon superconducting Fabry-Pérot (FP) resonators fabricated from a-SiC:H and NbTiN. The design of the loss measurement device (Fig. 4.2a) is similar to the one reported in Chapter 3 and in Refs. [9, 10], with the exception that we enabled wide-band measurements by using leaky-wave antennas (Fig. 4.2b) fabricated on 1-μm-thick SiN_x membranes [11, 12]. The signal from each antenna is coupled to a FP via a NbTiN coplanar waveguide (CPW) with 2-μm center line width and 2-μm gap width, designed to eliminate radiation loss [13]. The four FPs (FP1–4) have a NbTiN/a-SiC:H/NbTiN microstrip geometry with 2.1-μm-thick a-SiC:H and 14-μm line width. The power transmitted through the FPs is measured using CPW NbTiN-Al hybrid MKIDs [14]. The couplings between the FPs and the input/output CPW lines are made at the ends of each FP, with a 22-μm-long overlap between the FP microstrip lines and the center lines of the NbTiN CPWs (Fig. 4.2d). The galvanic connections between the NbTiN center lines, which are coupled to the FPs and the Al center lines of the CPW NbTiN-Al hybrid MKIDs, are made on a layer of SiN_x (Fig. 4.2d) to avoid enhanced erosion of the Al at the Si-NbTiN interfaces [15].

We optimized the FP resonator and FP coupler design to cover the wide bandwidth of 270–600 GHz (Appendix G). We limited the maximum value of

the FP resonators' coupling quality factor Q_c such that (1) the FP peaks do not become too sharp to measure with the 20 MHz resolution of the photomixer source that generates the 270–600 GHz radiation, and (2) there is sufficient transmission at higher frequencies where the losses are high. Furthermore, we limited the minimum value of Q_c so that the FP transmission peaks do not have too much overlap to be individually resolved. Taking these limitations into consideration, we chose resonator lengths of 3.00 mm, 4.50 mm, 6.75 mm and 10.13 mm and a coupler overlap length of 22 μm (Fig. 4.2d), resulting in Q_c values in the range of 0.4×10^3 to 24×10^3 in the range of 600–270 GHz for all four FPs.

We fabricated the device on a high-resistivity c-Si wafer (W1). We coated the wafer with 1 μm of SiN_x on the front side and on the back side, using low pressure chemical vapor deposition. We removed the SiN_x front side everywhere except at the antennas and at the Al lines of the MKIDs. We sputter-deposited the 300-nm-thick NbTiN ground layer (under the a-SiC:H), the 100-nm thick NbTiN top layer (on top of the a-SiC:H), and the 100-nm thick Al layer using an Evatec LLS 801. We deposited the a-SiC:H on top of the NbTiN ground layer, as discussed in Section 4.2. We etched the a-SiC:H using reactive ion etching (RIE) with an SF_6 and O_2 plasma. We patterned the leaky-wave antennas, CPW mm-submm feed lines, MKIDs and CPW microwave readout lines into the NbTiN ground plane using RIE. We wet-etched the Al center lines of the MKIDs. We patterned the SiN_x on the back side using RIE to define KOH etching windows behind the four antennas, and we removed the c-Si substrate below the antennas by KOH etching, such that each antenna sits on top of a SiN_x membrane. For stray light absorption we covered the back side of the chip with a β–Ta mesh [16], which we sputter-deposited using an Evatec LLS 801. We removed the β–Ta below the SiN_x membranes using RIE.

4.3.2. Measurement

We measured the loss at 20 mK on the chip that is described in Subsection 4.3.1 and shown in Fig. 4.2a. The experimental setup was similar to the one reported in Chapter 3 and in Refs. [9, 10]. The radiation from a continous-wave photomixer source (Toptica Photonics Terascan 780) was swept from 270 to 600 GHz in frequency steps of 20 MHz. The broad beam from the photomixer source was weakly coupled to all four antennas. The loss of the a-SiC:H was determined from the power that was transmitted through the FPs, measured by the response of the MKIDs as a function of frequency. The

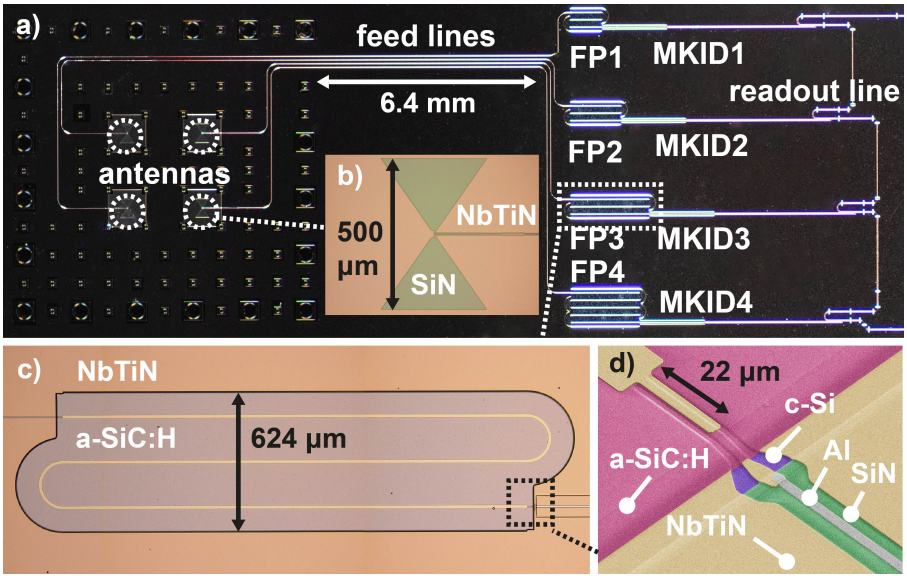

Figure 4.2: a) Photograph of the loss measurement device. The FPs receive the mm-submm signal from antennas, which receive radiation from a Toptica Photonics TeraScan 780 photomixer source. Each FP is coupled to an MKID, which detects the power transmitted through the FP. b) Micrograph of one of the leaky-wave antennas. c) Micrograph of FP3. The feed line is visible on the left side of the image and the MKID is visible on the right side of the image. d) Tilted scanning electron micrograph of the coupling of FP3 to the MKID, with false coloring.

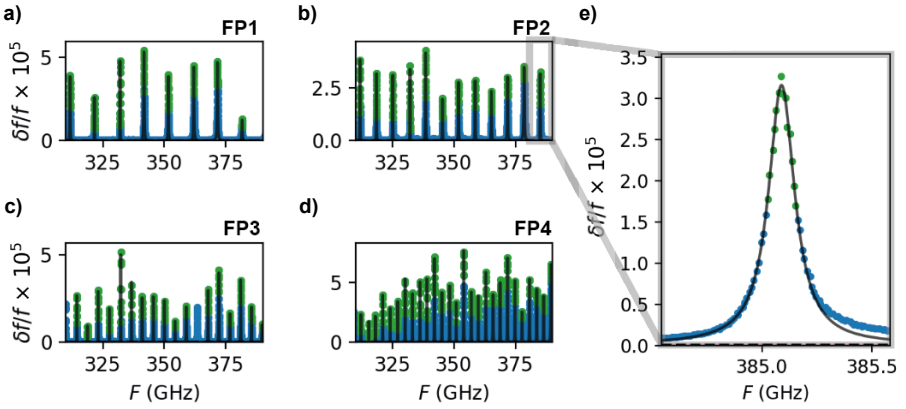

Figure 4.3: a–d) The measured MKID frequency response of FP1–4 in the 310–380 GHz band. The blue and green points represent the measurement data. The data represented as green points were used in the fitting. The black curves are Lorentzian fits to the FP transmission peaks, from which we obtained the loaded quality factor Q of each FP peak. The same analysis was performed for each of the seven frequency bands centered around 270, 310, 350, 400, 455, 520 and 600 GHz. e) Close-up of a single FP transmission peak of FP2.

transmitted power versus frequency is a sum of Lorentzian peaks located at $f_{\text{peak}} = nf_0$, where n is the mode number and f_0 is the fundamental resonance frequency. In Fig. 4.3a–d we plotted the measured MKID response in a frequency band around 350 GHz. Each peak corresponds to a loaded quality factor $Q = f_{\text{peak}}/\Delta f$, where Δf is the peak's full width at half maximum (FWHM).

4.3.3. Results

We determined the 270–600 GHz loss by fitting Lorentzian peaks to the MKID response data. We plotted the measured MKID response in the 310–380 GHz frequency band in Fig. 4.3. The variation in the peak heights in Fig. 4.3 is caused by a variation in the mm-submm power that enters the FPs, due to a frequency-dependence of the power output of the photomixer source and due to standing waves between the antennas and the FPs. We determined the Q value of each peak from a Lorentzian fit (Fig. 4.3e), where the fitting parameter Q is independent from the peak height. For the next steps in the analysis we separated the frequency response data into frequency bands centered around

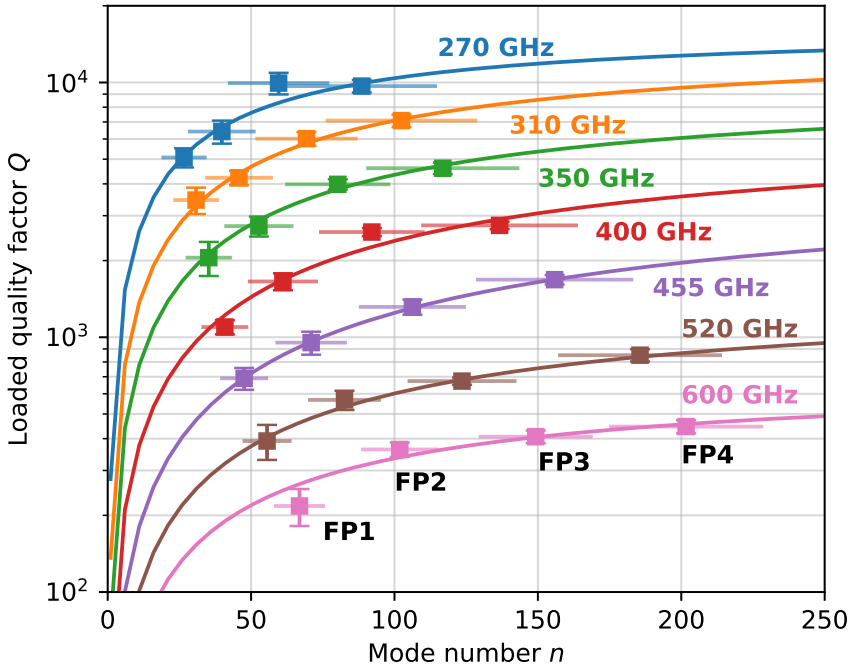

Figure 4.4: Average loaded quality factor Q versus average mode number n of the Fabry-Perot resonators (FP1–4) The curves are fits of Eq. (4.1). The vertical error bars represent the standard deviation ($\pm\sigma$) in Q. The horizontal bars represent the range of mode numbers used in computing the average.

270, 310, 350, 400, 455, 520 and 600 GHz. We determined the Q and n values at the center frequencies of each band from the average values computed over all peaks within each band. We present the average Q versus average n data in Fig. 4.4.

We determined the Q_i from the Q versus n data by fitting the equation:

$$Q = \frac{nQ_{\mathrm{c},1}Q_\mathrm{i}}{nQ_{\mathrm{c},1} + Q_\mathrm{i}}, \tag{4.1}$$

where $Q_\mathrm{c} = nQ_{\mathrm{c},1}$ is the FP's coupling quality factor. Here, the $Q_{\mathrm{c},1} = \pi/|t_\mathrm{c}|^2$, where t_c the transmission coefficient of the FPs' couplers. The FPs have identical couplers and therefore share a single $Q_{\mathrm{c},1}$ (and hence t_c) value, which is obtained together with Q_i from the fit (Fig. 4.4) of Eq. (4.1). Finally, from

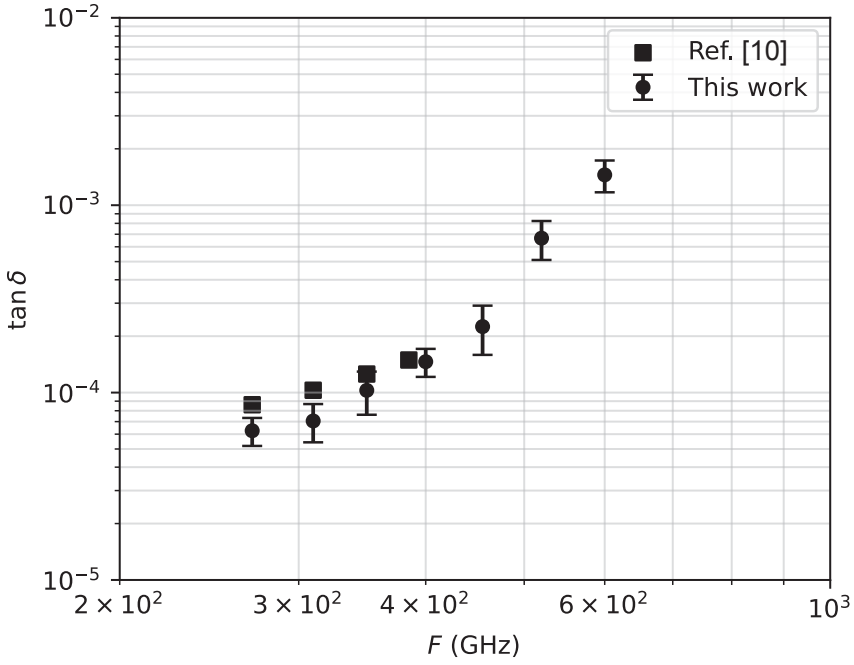

Figure 4.5: The mm-submm $\tan\delta = 1/(pQ_\mathrm{i})$ versus frequency, which we obtained by fitting Eq. (4.1) to the data in Fig. 4.4. The points represent the measured $\tan\delta$ values from this work, and the error bars represent one standard deviation ($\pm\sigma$) uncertainty in $\tan\delta$. The squares show the a-SiC:H losses reported in Ref. [10] (Chapter 3).

the FP resonators' internal quality factor Q_i we obtained the loss tangent $\tan\delta$:

$$\tan\delta = (pQ_\mathrm{i})^{-1}, \tag{4.2}$$

where p is the filling fraction of the a-SiC:H, which we determined to be 0.97 in our FPs using the EM-field solver Sonnet [17]. We present the resulting loss versus frequency data in the 270–600 GHz range in Fig. 4.5. We observe that the loss increases monotonically with frequency and that it is in agreement with the loss reported in Ref. [10] (Chapter 3).

4.4. Mid infrared loss measured by Fourier-transform spectroscopy

4.4.1. Sample fabrication

To measure the 3–100 THz loss of the a-SiC:H we fabricated three kinds of a-SiC:H samples for FTS measurements. Sample 1 (S1): A single a-SiC:H membrane with 2.1 μm thickness and 2 cm $\times$ 2 cm surface area, supported by a 400-μm-thick c-Si frame. Sample 2 (S2): A stack of two units that are equivalent to S1, as shown in Fig. 4.6b. Sample 3 (S3): A 2.1-μm-thick a-SiC:H film (not a membrane) on a double side polished c-Si substrate. We fabricated S1 and S2 from W3 and S3 from W4. The a-SiC:H films that were fabricated into membranes were deposited on the front side of the substrates, and were deposited simultaneously with the other a-SiC:H samples that are described in this work. Separately, we deposited an a-SiC:H layer on the back side of W3. This back side layer was removed using RIE below the membrane positions, thereby creating square-shaped etching windows. The membranes were then created by removing the c-Si substrate using KOH etching from the back side of the wafer.

4.4.2. Measurement

To obtain the 3–100 THz loss, we measured the FTS transmisison of S1–3 at room temperature. Furthermore, we measured the FTS transmission of an additional a-SiC:H membrane at 5 K to investigate if there is a temperature dependence of the complex dielectric constant, and we observed a fractional decrease of 1% in the $\varepsilon_{\mathrm{r}}^{'}$ upon cooling. For further details we refer to the Supplemental Material. The FTS transmission is defined as $T \equiv I_{\mathrm{s}}/I_{\mathrm{bg}}$. The I_{s} is the measured intensity when the sample is in the path from the source to the detector (Fig. 4.6a), and I_{bg} is the measured intensity without a sample in place. We measured the transmission through S1 and S2 in the ranges of 3–10 THz and 18–30 THz using a BioRad FTS system, at a resolution of 2.0 cm^{-1} and 0.5 cm^{-1} for S1 and S2 respectively. In Fig. 4.6a we present a photograph of S2 inside the BioRad FTS. Here we used a room temperature deuterated triglycine sulfate (DTGS) detector for frequencies above 4 THz and a cryogenic bolometer detector for frequencies below 4 THz. The sample chamber of the BioRad FTS was continously purged with dry air prior to and during the measurement. Furthermore, we measured the transmission through

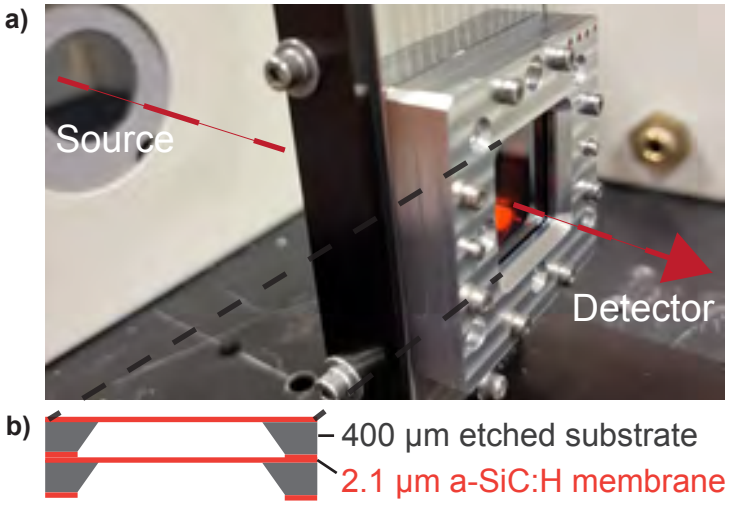

Figure 4.6: a) Photograph of S2 in the BioRad FTS system. b) Schematic of S2, which consists of two stacked a-SiC:H membranes.

S3 in the range of 18–100 THz using a Thermo Fischer Nicolet FTS system at a resolution of 4.0 cm^{-1}, where the sample chamber was continuously purged with nitrogen prior to and during the measurement.

4.4.3. Results

We determined the 3–100 THz loss by fitting transfer matrix method (TMM) [18] models to the FTS transmission data of S1–3. The transmission data and the best-fit transmission curves are presented in Fig. 4.7a and a close-up of the data in the 3–10 THz range is presented in Fig. 4.8. Here the complex permittivity $\hat{\varepsilon}_r \equiv \varepsilon_r^{'} + i\varepsilon_r^{''}$ (and therefore the loss) of the a-SiC:H was a model parameter which we obtained from the fitting. We combined the FTS transmission data of S1–3 in a single fitting procedure, where we normalized the fitting residuals by the number of data points in each data set. In the case of S3, we measured the bare c-Si substrate prior to the deposition of the a-SiC:H and we included the substrate properties in the TMM model. We note that the periodicity in the transmission of S2 (Fig. 4.7a) is dictated by the inter-membrane distance.

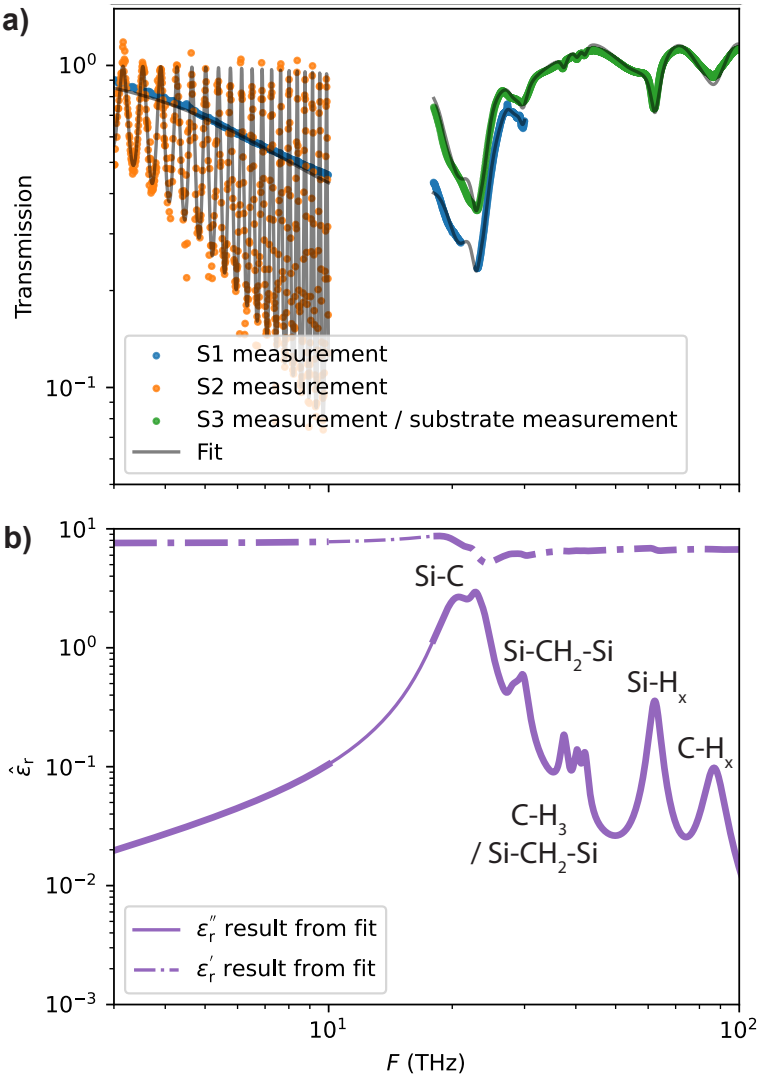

Figure 4.7: a) The points show the transmission through the a-SiC:H samples measured using FTS in the range of 3–100 THz, for S1–3. The solid grey curves show the best-fit results of TMM models where the $\hat{\varepsilon}_r$ is parameterized using the MHD dispersion model (Eq. (4.3)). A close-up of the 3–10 THz range is presented in Fig. 4.8. The plotted data of S3 was divided by the measured transmission of the bare c-Si substrate to clearly show the absorption features of the a-SiC:H. b) The real (ε_r') and imaginary (ε_r'') parts of the complex permittivity $\hat{\varepsilon}_r$ resulting from the fitting to the transmission data in Fig. 4.7a. The thin curves show the fitting results in the range of 3-100 THz, and the thick curves show the ranges where measurement data was available. The annotations identify the modes that are present in the absorption spectrum, which are detailed in Table H.1 in Appendix H.

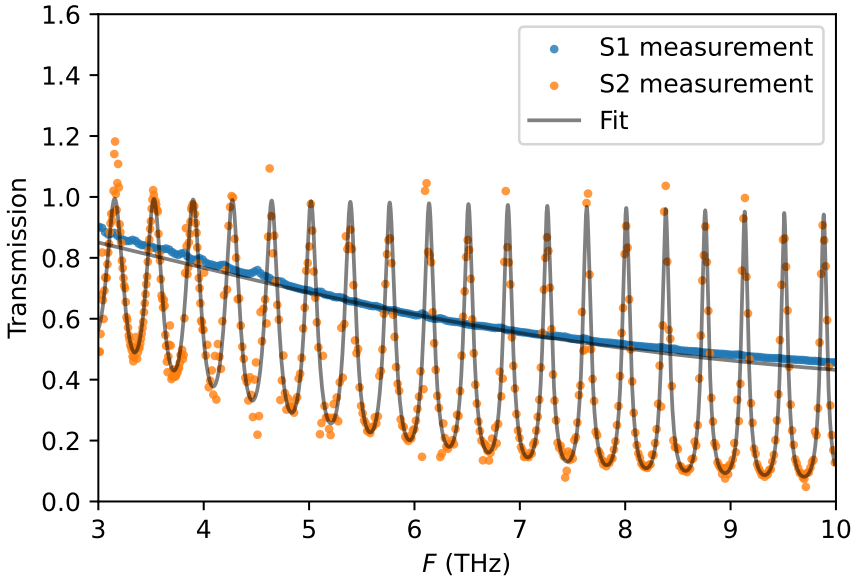

Figure 4.8: The points show the transmission data of S1 and S2. The solid grey curve shows the best-fit result of the TMM model. The data and fit result are a close-up of the data presented in Fig. 4.7a.

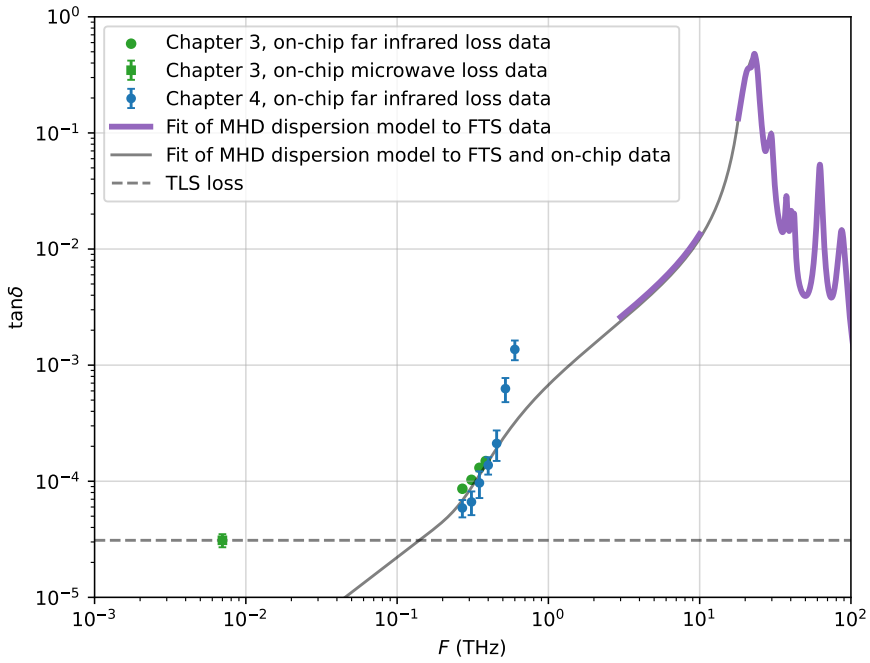

Figure 4.9: Loss tangent $\tan\delta$ versus frequency of the a-SiC:H. The solid grey curve represents the $\tan\delta$ which we obtained by fitting the MHD dispersion model to the combined FTS-measured transmission data (Fig. 4.7a) and FP-measured loss data (Fig. 4.5), as described in Section 4.5. The purple curve represents the $\tan\delta$ which we obtained by fitting the MHD dispersion model (Eq. (4.3)) to only the FTS data (Fig. 4.7a). The blue points represent the FP-measured loss data from this work (Fig. 4.5). The green points represent the a-SiC:H loss data reported from Chapter 3 (Ref. [10]). The intersection of the solid grey curve and the horizontal dashed line illustrates the crossover between the low-power cryogenic TLS loss and the loss due to vibrational modes.

In the fitting of the TMM models to the transmission data we parameterized the $\hat{\varepsilon}_{\mathrm{r}}$ of the a-SiC:H using the MHD dispersion model [19, 20]:

$$\hat{\varepsilon}_{\mathrm{r}} = \hat{\varepsilon}_{\infty} + \sum_{j=1}^{M} \frac{\Delta\hat{\varepsilon}_j \cdot \omega_{T_j}^2}{\omega_{T_j}^2 - \omega^2 - i\omega\Gamma'_j(\omega)}, \tag{4.3}$$

where the $\hat{\varepsilon}_{\mathrm{r}}$ consists of a sum of M modes (oscillators). Here, the broadening $\Gamma_j^{'}$ equals:

$$\Gamma_j^{'} = \Gamma_j \exp\left[-\alpha_j \left(\frac{\omega_{T_j}^2 - \omega^2}{\omega\Gamma_j}\right)^2\right], \tag{4.4}$$

where the broadening is purely Lorentzian if α_j equals zero, and is an interpolation between Lorentzian and Gaussian if α_j is greater than zero [19, 21, 22]. The Γ_j is the Lorentzian damping coefficient, ω_{T_j} is the center frequency of a mode, and $\Delta\hat{\varepsilon}_j$ is defined as $\Delta\hat{\varepsilon}_j \equiv \hat{\varepsilon}_j - \hat{\varepsilon}_{j+1}$. The modes are ordered such that $\omega_{T_{j+1}} > \omega_{T_j}$. The $\hat{\varepsilon}_\infty \equiv \hat{\varepsilon}_{M+1}$ is the contribution from modes at higher frequencies.

In Fig. 4.7b we present the $\hat{\varepsilon}_{\mathrm{r}}$ of the a-SiC:H resulting from the best-fit parameters, which are listed in Table H.1 in Appendix H. The observed vibrational modes have previously been reported in literature [23]: The Si–C stretch absorption band (∼18–30 THz), the Si–CH_2–Si wagging mode (∼30–31 THz), the Si–CH_2–Si scissor and bending modes (∼40 THz) and the C–H_3 symmetric (∼37 THz) and asymmetric (∼42 THz) bending bands, the Si–H_x stretch band (∼60–69 THz) and the C–H_x stretch band (∼84–93 THz). The purple curve of Fig. 4.9 represents the $\tan\delta = \varepsilon_{\mathrm{r}}^{''}/\varepsilon_{\mathrm{r}}^{'}$ corresponding to the $\hat{\varepsilon}_{\mathrm{r}}$ (purple curve) plotted in Fig. 4.7b.

4.5. Model of dielectric loss from microwave to mid-infrared

Finally, we examined whether the loss measured with the FPs at 270–600 GHz and at 20 mK (Fig. 4.5) and the loss measured by FTS in the range of 3–100 THz and at room temperature (fig. 4.7b) can be consistently explained with a common MHD dispersion model. Here we note that amorphous dielectrics typically exhibit negligible temperature dependence of the dielectric loss at infrared wavelengths [24]. We searched for a set of parameters in Eq. (4.3) using a numerical optimization algorithm that simultaneously minimizes the differences between (1) the calculated $\tan\delta$ and the FP-measured $\tan\delta$, and (2) the calculated transmission and the FTS-measured transmission. In the fitting (Fig. 4.5) we included the FP-measured $\tan\delta$ values from Ref. [10] (Chapter 3). The 520 GHz and 600 GHz points in Fig. 4.5 had to be excluded because they could not be reproduced by our current model. The resulting best-fit parameter values are listed in Table H.2 in Appendix H. In Fig. 4.9

we co-plotted the $\tan\delta$ resulting from the combined fitting to the FTS and FP measurements (grey curve), and the $\tan\delta$ corresponding to Fig. 4.7b resulting from FTS measurements alone (purple curve). Except for the points at 520 and at 600 GHz (which will be discussed in the next section), the modeled frequency dependence of $\tan\delta$ agrees well with both the FP and FTS measurements over the entire frequency range that was covered.

4.6. Discussion on the origin of the loss in deposited dielectrics

Our results show that the absorption tail of vibrational modes located at frequencies above 10 THz can explain the measured losses in the range of 270–455 GHz. Above a frequency of roughly 200 GHz the losses are anticipated to be dominated by vibrational modes, and below a frequency of roughly 200 GHz and at cryogenic temperatures and low power the loss is expected to be dominated by TLSs. At 520 GHz and at 600 GHz the on-chip loss data is not reproducible by the MHD dispersion model with the modes that have been reported in literature. For an overview of the modes in amorphous and crystalline SiC we refer to Refs. [23, 25]. The excess loss at 520 GHz and at 600 GHz is not expected to originate from the bulk of the superconductor since the NbTiN has an energy gap of roughly 1.1 THz. However, it is possible that the excess loss is caused by a small fraction of the superconductor which behaves differently than the bulk of the superconductor [26–28]. We recommend additional experiments, e.g. using narrow CPW resonators [13], to clarify this discrepancy between the model and our data at 520 GHz and at 600 GHz. Furthermore, we recommend additional measurements in the ∼0.1–20 THz frequency range with improved signal-to-noise ratio, e.g. using MKID detectors, to investigate if additional and relatively weak vibrational modes [29] which were not included in our model contribute to the mm-submm loss.

Our results pave the way for a thorough understanding of the dielectric loss in deposited dielectrics from microwave to near-infrared wavelengths. We emphasize that strong vibrational modes in the 10–30 THz range are present not only in a-SiC:H, but have also been reported for other commonly used deposited dielectrics such as a-Si:H [30, 31], SiN_x [19] and SiO_x [20]. Furthermore, the TLS loss tangent values at cryogenic temperatures and low electric field strengths $\tan\delta_{\mathrm{TLS}}$ reported at microwave frequencies of a-Si:H ($\sim 10^{-5}$) [9, 32, 33], SiN_x ($\sim 10^{-4}$) [32] and SiO_x ($\sim 10^{-4}$–10^{-3}) [32, 34] lead us to an-

ticipate a similar crossover for these materials from loss dominated by TLSs to loss dominated by vibrational modes.

We note that in our model we have not taken into account a possible loss contribution from Debye relaxation, since at sub-Kelvin temperatures the Debye loss is expected to be negligible due to a very large relaxation time at these temperatures. Furthermore, the room temperature FTS measurements were performed at frequencies above 3 THz, and at those frequencies the Debye loss is expected to be insignificant in comparison with the loss wings of the infrared vibrational modes, due to the $F^{-1/2}$ scaling of the Debye loss [20, 22]. However, if room temperature FTS measurements are performed at frequencies below ∼100 GHz the Debye loss could start to become a dominant loss contribution relative to the loss wings of the infrared vibrational modes, which scale proportionally to F in the case of a Lorentzian absorption peak and at frequencies well below the mode's resonance frequency [35].

4.7. Conclusion

We demonstrated that the dielectric loss of a-SiC:H above 200 GHz is dominated by the absorption tail of vibrational modes which are located at frequencies above 10 THz. Our results pave the way for a thorough understanding of the dielectric loss in deposited dielectrics from microwave to near infrared wavelengths, and will be beneficial for mm-submm astronomical instrumentation. In Chapter 5 we present how the a-SiC:H has been applied in mm-submm astronomical instruments.

Bibliography

[1] B. Buijtendorp, A. Endo, W. Jellema, K. Karatsu, K. Kouwenhoven, D. Lamers, A. Van Der Linden, K. Rostem, H. Veen, E. Wollack, J. Baselmans, and S. Vollebregt, "Vibrational modes as the origin of dielectric loss at 0.27–100 THz in a - Si C : H," *Physical Review Applied*, vol. 23, p. 014035, Jan. 2025.

[2] C. Müller, J. H. Cole, and J. Lisenfeld, "Towards understanding two-level-systems in amorphous solids: Insights from quantum circuits," *Rep. Prog. Phys.*, vol. 82, no. 12, p. 124501, 2019.

[3] W. A. Phillips, "Tunneling states in amorphous solids," *J. Low Temp. Phys.*, vol. 7, no. 3-4, pp. 351–360, 1972.

[4] P. Sarro, C. de Boer, E. Korkmaz, and J. Laros, "Low-stress PECVD SiC thin films for IC-compatible microstructures," *Sens. Actuator A Phys.*, vol. 67, no. 1-3, pp. 175–180, 1998.

[5] C. Ricciardi, A. Primiceli, G. Germani, A. Rusconi, and F. Giorgis, "Microstructure analysis of a-SiC:H thin films grown by high-growth-rate PECVD," *Journal of Non-Crystalline Solids*, vol. 352, pp. 1380–1383, June 2006.

[6] W. Yu, W. Lu, L. Han, and G. Fu, "Structural and optical properties of hydrogenated amorphous silicon carbide films by helicon wave plasma-enhanced chemical vapour deposition," *Journal of Physics D: Applied Physics*, vol. 37, pp. 3304–3308, Dec. 2004.

[7] S. Nakashima and H. Harima, "Raman Investigation of SiC Polytypes," *physica status solidi (a)*, vol. 162, pp. 39–64, July 1997.

[8] J. Budai, I. Hanyecz, E. Szilágyi, and Z. Tóth, "Ellipsometric study of SixC films: Analysis of Tauc–Lorentz and Gaussian oscillator models," *Thin Solid Films*, vol. 519, pp. 2985–2988, Feb. 2011.

[9] S. Hähnle, K. Kouwenhoven, B. Buijtendorp, A. Endo, K. Karatsu, D. Thoen, V. Murugesan, and J. Baselmans, "Superconducting Microstrip Losses at Microwave and Submillimeter Wavelengths," *Phys. Rev. Appl.*, vol. 16, no. 1, p. 014019, 2021.

[10] B. Buijtendorp, S. Vollebregt, K. Karatsu, D. Thoen, V. Murugesan, K. Kouwenhoven, S. Hähnle, J. Baselmans, and A. Endo, "Hydrogenated Amorphous Silicon Carbide: A Low-Loss Deposited Dielectric for Microwave to Submillimeter-Wave Superconducting Circuits," *Physical Review Applied*, vol. 18, p. 064003, Dec. 2022.

[11] S. Hahnle, O. Yurduseven, S. Van Berkel, N. Llombart, J. Bueno, S. J. C. Yates, V. Murugesan, D. J. Thoen, A. Neto, and J. J. A. Baselmans, "An Ultrawideband Leaky Lens Antenna for Broadband Spectroscopic Imaging Applications," *IEEE Transactions on Antennas and Propagation*, vol. 68, pp. 5675–5679, July 2020.

[12] A. Neto, "UWB, Non Dispersive Radiation From the Planarly Fed Leaky Lens Antenna - Part 1: Theory and Design," *IEEE Transactions on Antennas and Propagation*, vol. 58, pp. 2238–2247, July 2010.

[13] S. Hähnle, N. V. Marrewijk, A. Endo, K. Karatsu, D. J. Thoen, V. Murugesan, and J. J. A. Baselmans, "Suppression of radiation loss in high kinetic inductance superconducting co-planar waveguides," *Applied Physics Letters*, vol. 116, p. 182601, May 2020.

[14] R. M. J. Janssen, J. J. A. Baselmans, A. Endo, L. Ferrari, S. J. C. Yates, A. M. Baryshev, and T. M. Klapwijk, "High optical efficiency and photon noise limited sensitivity of microwave kinetic inductance detectors using phase readout," *Appl. Phys. Lett.*, vol. 103, no. 20, p. 203503, 2013.

[15] L. Ferrari, O. Yurduseven, N. Llombart, S. J. C. Yates, J. Bueno, V. Murugesan, D. J. Thoen, A. Endo, A. M. Baryshev, and J. J. A. Baselmans, "Antenna Coupled MKID Performance Verification at 850 GHz for Large Format Astrophysics Arrays," *IEEE Transactions on Terahertz Science and Technology*, vol. 8, pp. 127–139, Jan. 2018.

[16] J. J. A. Baselmans, S. J. C. Yates, S. M. Doyle, A. Baryshev, J. Bueno, L. Ferrari, N. Llombart, V. Murugesan, D. J. Thoen, O. Yurduseven, and P. Barry, "Eliminating stray radiation inside large area imaging arrays," in *Millimeter, Submillimeter, and Far-Infrared Detectors and Instrumentation for Astronomy IX* (J. Zmuidzinas and J.-R. Gao, eds.), (Austin, United States), p. 67, SPIE, July 2018.

[17] "Sonnet User's Guide — Sonnet 17."

[18] A. Luce, A. Mahdavi, F. Marquardt, and H. Wankerl, "TMM-Fast, a transfer matrix computation package for multilayer thin-film optimization: Tutorial," *Journal of the Optical Society of America A*, vol. 39, p. 1007, June 2022.

[19] G. Cataldo, J. A. Beall, H.-M. Cho, B. McAndrew, M. D. Niemack, and E. J. Wollack, "Infrared dielectric properties of low-stress silicon nitride," *Optics Letters*, vol. 37, p. 4200, Oct. 2012.

[20] G. Cataldo, E. J. Wollack, A. D. Brown, and K. H. Miller, "Infrared dielectric properties of low-stress silicon oxide," *Optics Letters*, vol. 41, p. 1364, Apr. 2016.

[21] C. C. Kim, J. W. Garland, H. Abad, and P. M. Raccah, "Modeling the optical dielectric function of semiconductors: Extension of the critical-point parabolic-band approximation," *Physical Review B*, vol. 45, pp. 11749–11767, May 1992.

[22] G. Cataldo and E. J. Wollack, "Submillimeter and far-infrared dielectric properties of thin films," in *SPIE Astronomical Telescopes + Instrumentation* (W. S. Holland and J. Zmuidzinas, eds.), (Edinburgh, United Kingdom), p. 99142W, July 2016.

[23] S. King, M. French, J. Bielefeld, and W. Lanford, "Fourier transform infrared spectroscopy investigation of chemical bonding in low-k a-SiC:H thin films," *Journal of Non-Crystalline Solids*, vol. 357, pp. 2970–2983, July 2011.

[24] U. Strom and P. C. Taylor, "Temperature and frequency dependences of the far-infrared and microwave optical absorption in amorphous materials," *Physical Review B*, vol. 16, pp. 5512–5522, Dec. 1977.

[25] A. M. Hofmeister, K. M. Pitman, A. F. Goncharov, and A. K. Speck, "Optical Constants of Silicon Carbide for Astrophysical Applications. II. Extending Optical Functions from Infrared to Ultraviolet using Single-crystal Absorption Spectra," *The Astrophysical Journal*, vol. 696, pp. 1502–1516, May 2009.

[26] V. Lacquaniti, S. Maggi, E. Monticone, and R. Steni, "Thickness dependence of electrical and structural properties of Nb thin films," *Physica Status Solidi (a)*, vol. 151, pp. 335–344, Oct. 1995.

[27] M. S. M. Minhaj, S. Meepagala, J. T. Chen, and L. E. Wenger, "Thickness dependence on the superconducting properties of thin Nb films," *Physical Review B*, vol. 49, pp. 15235–15240, June 1994.

[28] A. Chandrasekaran, R. W. Van De Kruijs, J. M. Sturm, and F. Bijkerk, "Nb Texture Evolution and Interdiffusion in Nb/Si-Layered Systems," *ACS Applied Materials & Interfaces*, vol. 13, pp. 31260–31270, July 2021.

[29] H. Shanks, W. Kamitakahara, J. McClelland, and C. Carlone, "Phonon density of states of amorphous silicon," *Journal of Non-Crystalline Solids*, vol. 59–60, pp. 197–200, Dec. 1983.

[30] A. A. Langford, M. L. Fleet, B. P. Nelson, W. A. Lanford, and N. Maley, "Infrared absorption strength and hydrogen content of hydrogenated amorphous silicon," *Physical Review B*, vol. 45, pp. 13367–13377, June 1992.

[31] B. T. Buijtendorp, J. Bueno, D. J. Thoen, V. Murugesan, P. M. Sberna, J. J. A. Baselmans, S. Vollebregt, and A. Endo, "Characterization of

low-loss hydrogenated amorphous silicon films for superconducting resonators," *Journal of Astronomical Telescopes, Instruments, and Systems*, vol. 8, June 2022.

[32] A. D. O'Connell, M. Ansmann, R. C. Bialczak, M. Hofheinz, N. Katz, E. Lucero, C. McKenney, M. Neeley, H. Wang, E. M. Weig, A. N. Cleland, and J. M. Martinis, "Microwave dielectric loss at single photon energies and millikelvin temperatures," *Appl. Phys. Lett.*, vol. 92, no. 11, p. 112903, 2008.

[33] B. A. Mazin, D. Sank, S. McHugh, E. A. Lucero, A. Merrill, J. Gao, D. Pappas, D. Moore, and J. Zmuidzinas, "Thin film dielectric microstrip kinetic inductance detectors," *Appl. Phys. Lett.*, vol. 96, no. 10, p. 102504, 2010.

[34] J. Gao, A. Vayonakis, O. Noroozian, J. Zmuidzinas, P. K. Day, H. G. Leduc, B. Young, B. Cabrera, and A. Miller, "Measurement of loss in superconducting microstrip at millimeter-wave frequencies," in *The Thirteenth International Workshop on Low Temperature Detectors — LTD13*, (Stanford (California)), pp. 164–167, 2009.

[35] J. Petzelt and S. Kamba, "Submillimetre and infrared response of microwave materials: Extrapolation to microwave properties," *Materials Chemistry and Physics*, vol. 79, pp. 175–180, Apr. 2003.

Chapter 5

Conclusions and outlook

5.1. Conclusions

We demonstrated that the mm-submm loss in deposited dielectrics can be explained by the absorption tail of infrared vibrational modes which are located above 10 THz. These results pave the way for a thorough understanding of the dielectric loss in deposited dielectrics from microwave to near infrared wavelengths. Furthermore, we found that a-SiC:H has a very low mm-submm loss tangent of 1.3×10^{-4} at 350 GHz, which makes it a promising low-loss deposited dielectric for mm-submm superconducting integrated circuits.

Additionally, we performed material characterization of the a-SiC:H and a-Si:H. From the Raman measurements we observed that the a-Si:H and the a-SiC:H are fully amorphous. For the a-Si:H we observed that an increase in the substrate temperature during deposition T_{sub} results in films with less hydrogen, less voids, smaller microstructure parameter, less bond-angle disorder, and higher refractive index. Even though the structural and compositional properties at room temperature of the a-Si:H exhibited a monotonic dependence on T_{sub}, we did not observe a correlation of the room temperature properties with the cryogenic microwave $\tan\delta$.

5.2. Applications of the a-SiC:H in on-chip mm-submm superconducting astronomical instruments

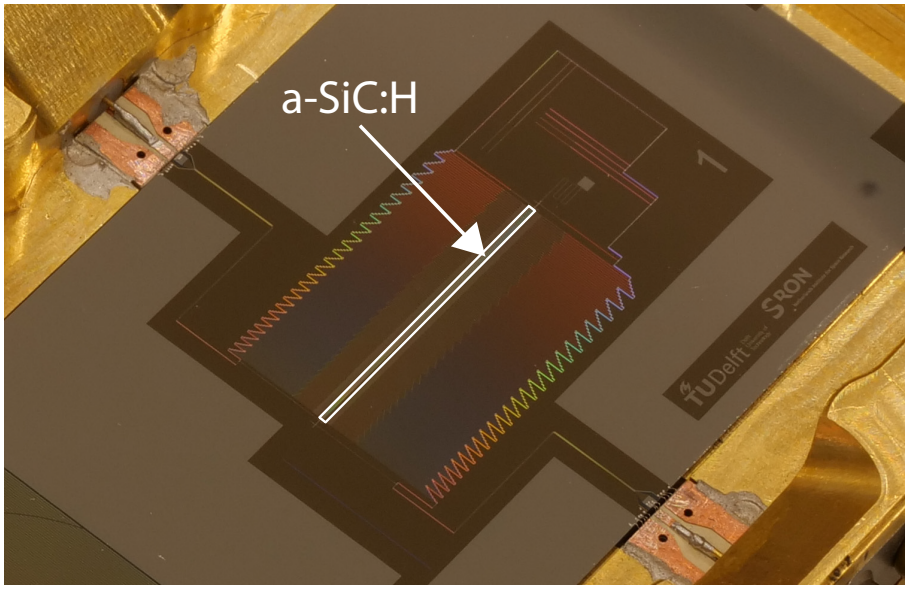

Figure 5.1: Photograph of the part of the DESHIMA 2.0 chip with the filter bank and detectors. The DESHIMA 2.0 chip has seen first light at the ASTE telescope in the Atacama Desert in 2023. The area of the microstrip filter bank with the a-SiC:H is highlighted by the white edges.

The a-SiC:H has transmitted light from distant galaxies: The dielectric was applied in the DESHIMA 2.0 filter bank (Fig. 5.1), which has seen first light in 2023 at the ASTE telescope in the Atacama Desert. Furthermore, the upcoming DESHIMA 2.1 design will incorporate the a-SiC:H in a novel type of filter with increased filter transmission, which was designed by Louis Marting and will be fabricated by Leon Olde Scholtenhuis, during the course of their PhD projects.

Furthermore, the a-SiC:H was applied in a novel compact KID (CKID) design, in the M.Sc. thesis project [2] of Sietse de Boer which was supervised within the context of this PhD project. Here, the capacitive part of the MKID exists of a parallel plate capacitor with a-SiC:H, thereby drasti-

cally decreasing the detector's footprint. Although the detectors did not reach generation-recombination noise limited performance under dark conditions, the small footprint of this novel detector is promising. Since it was found that the noise equivalent power (NEP) decreased when decreasing the width of the inductive, coplanar waveguide (CPW) part of the MKID due to the relatively large kinetic inductance fraction, it was suggested to use electron beam lithography to fabricate narrower CPW lines. Furthermore, it was suggested to study the effect of the thickness of the a-SiC:H and of the parallel plate capacitor area on the noise properties of the detector. Here we note that recently it has been reported that a-Si:H films deposited by ICPCVD [3], and evaporated amorphous germanium films [4], have low TLS density and therefore potentially can be used to fabricate CKIDs with low noise.

Another type of MKID which incorporates a parallel plate capacitor with a-SiC:H was studied by Kevin Kouwenhoven as part of his PhD project. Here, the effect of the capacitive area and of the thickness of the a-SiC:H on the loss and noise properties of the MKID were studied. The capacitive area was varied by a factor 44 and the a-SiC:H thickness was varied by a factor 4. A thickness dependence of the microwave loss was found, which can be explained by excess losses originating from surface layers, which have a relatively large contribution for thinner dielectrics. However, the frequency noise did not demonstrate this effect. It was observed that the frequency noise decreased with decreasing PPC area.

5.3. Impact of the work

The a-SiC:H has the lowest mm-submm losses for deposited dielectrics so far reported in literature (Fig. 5.2). This means that the a-SiC:H currently is the most promising deposited dielectric for on-chip filter banks. The low losses allow for larger filter resolutions (resolving powers) without sacrificing too much optical efficiency. This enables a wide range of integrated field unit (IFU) designs with relatively large resolving powers, and therefore the a-SiC:H is a good building block for the TIFUUN project.

The application of the Maxwell-Helmholtz-Drude dispersion model to explain the losses in the 0.1–1 THz range is novel in the field of mm-submm astronomical instrumentation. The model paves the way for a solid understanding of the mm-submm loss in deposited dielectrics. This will be beneficial for the further development of low-loss deposited dielectrics for mm-submm astronomy.

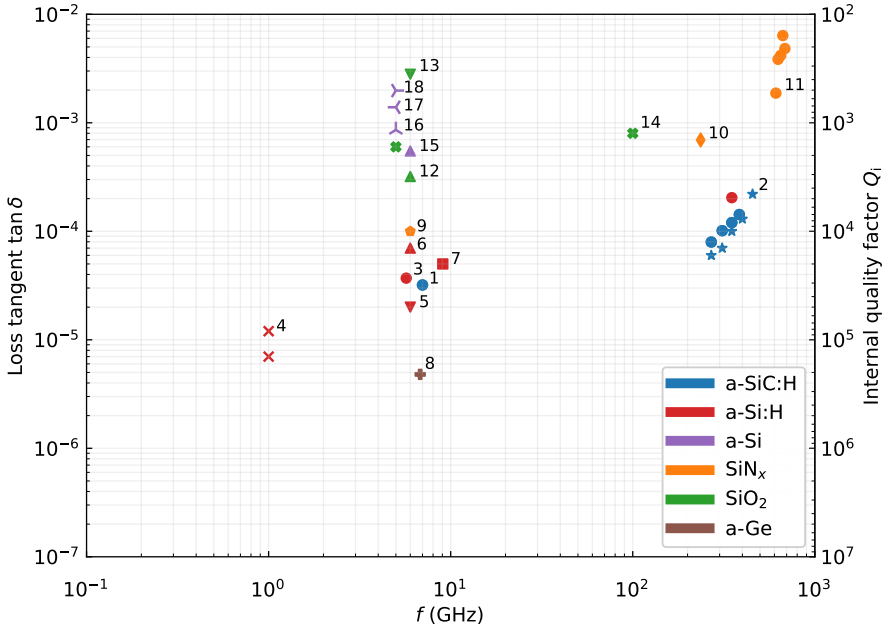

Figure 5.2: An overview of the mm-submm wave and microwave cryogenic dielectric loss tangent data, which had been reported in literature at the start of this PhD project for various deposited dielectrics. Data sources: (1) Chapter 3 (Ref. [5]), microstrip; (2) Chapter 4 (Ref. [6]), microstrip; (3) Ref. [7], microstrip; (4) Ref. [3], PPC; (5) Ref. [8], PPC; (6): Ref. [8], CPW; (7) Ref. [8], PPC; (8) Ref. [4], CPW; (9) Ref. [8]; (10) Ref. [9], microstrip; (11) Ref. [10], CPW; (12) Ref. [8], CPW, thermal SiO_2; (13) Ref. [8], CPW, sputtered SiO_2; (14) Ref. [11], microstrip; (15) Ref. [8], CPW; (16): Ref. [12], $T_{sub} = 50°C$; (17): Ref. [12], $T_{sub} = 225°C$; (18): Ref. [12], $T_{sub} = 425°C$.

5.4. Output of this PhD project

This PhD project has resulted in:

- Three first-authored journal papers.
- Four co-authored journal papers, where the results of this PhD project were implemented in follow-up experiments or applications.
- Four first-authored contributions to scientific conferences.
- Five co-authored contributions to scientific conferences.

- Contributions to multiple papers which are currently in preparation in the context of the lab and on-sky measurements of DESHIMA 2.0 and DESHIMA 2.1.

- The supervision of a M.Sc. thesis project [2].

- A patent on high-frequency cryogenic applications of a-SiC:H [13].

5.5. Recommendations

We recommend to test the effect of T_{sub} on the infrared absorption spectrum and the mm-submm loss of a-SiC:H and a-Si:H. Here we note that we currently only have mm-submm loss data for a-SiC:H deposited at a relatively high T_{sub} of 400°C and for a-Si:H deposited at a relatively low T_{sub} of 250°C. It is possible that depositing the a-Si:H at higher T_{sub} will result in decreased mm-submm loss due to a reduction in hydrogen content and a resulting reduction in the intensity of the absorption peak near 640 cm^{-1}. However, it is impractical that the a-Si:H deposited by PECVD exhibits high stress when deposited at a T_{sub} of 350°C (Section 2.3), in contrast to the a-SiC:H which exhibits a low stress value (Section 2.3) when deposited at a T_{sub} of 400°C. Therefore, we recommend to investigate if low stress a-Si:H and a-SiC:H films with low hydrogen content and potentially lower losses can be deposited by ICPCVD [3]. Furthermore, we recommend to investigate if the a-SiC:H can be optimized by decreasing the intensity of the Si-C absorption band near 750 cm^{-1} . This could be achieved by decreasing the Si/C ratio of the a-SiC:H, for example by decreasing the LF power [1] or by increasing the SiH_4/CH_4 gas flow ratio during the deposition. However, it is not yet clear if this would produce the desired effect since the higher Si/C ratio could lead to an increased intensity of the Si-H_x absorption band near 19 THz. Additionally, we recommend to perform measurements on a wider range of deposited dielectrics. For example, the mm-submm loss values of hydrogen-free amorphous silicon (carbide) and of amorphous germanium [4] have not yet been measured. In addition to measuring these other novel dielectrics, we recommend additional FTS measurements in the 1–20 THz frequency range to investigate if additional infrared vibrational modes, including phonon modes, are present in the a-SiC:H and a-Si:H [14]. For increased sensitivity in the FTS measurements we recommend to investigate if even thicker membranes than 2 μm can be fabricated.

Bibliography

[1] P. Sarro, C. de Boer, E. Korkmaz, and J. Laros, "Low-stress PECVD SiC thin films for IC-compatible microstructures," *Sens. Actuator A Phys.*, vol. 67, no. 1-3, pp. 175–180, 1998.

[2] S. H. de Boer, "Compact MKIDs - Miniaturization of Microwave Kinetic Inductance Detectors," *M.Sc. thesis, TU Delft, Delft, The Netherlands*, May 2021.

[3] F. Defrance, A. D. Beyer, S. Shu, J. Sayers, and S. R. Golwala, "Characterization of the low electric field and zero-temperature two-level-system loss in hydrogenated amorphous silicon," *Physical Review Materials*, vol. 8, p. 035602, Mar. 2024.

[4] C. J. Kopas, J. Gonzales, S. Zhang, D. R. Queen, B. Wagner, M. Robinson, J. Huffman, and N. Newman, "Low microwave loss in deposited Si and Ge thin-film dielectrics at single-photon power and low temperatures," *AIP Advances*, vol. 11, p. 095007, Sept. 2021.

[5] B. Buijtendorp, S. Vollebregt, K. Karatsu, D. Thoen, V. Murugesan, K. Kouwenhoven, S. Hähnle, J. Baselmans, and A. Endo, "Hydrogenated Amorphous Silicon Carbide: A Low-Loss Deposited Dielectric for Microwave to Submillimeter-Wave Superconducting Circuits," *Physical Review Applied*, vol. 18, p. 064003, Dec. 2022.

[6] B. T. Buijtendorp, A. Endo, W. Jellema, K. Karatsu, K. Kouwenhoven, D. Lamers, A. J. van der Linden, K. Rostem, M. Veen, E. J. Wollack, J. J. A. Baselmans, and S. Vollebregt, "Vibrational modes as the origin of dielectric loss at 0.27-100 THz in a-SiC:H," May 2024.

[7] S. Hähnle, K. Kouwenhoven, B. Buijtendorp, A. Endo, K. Karatsu, D. Thoen, V. Murugesan, and J. Baselmans, "Superconducting Microstrip Losses at Microwave and Submillimeter Wavelengths," *Phys. Rev. Appl.*, vol. 16, no. 1, p. 014019, 2021.

[8] A. D. O'Connell, M. Ansmann, R. C. Bialczak, M. Hofheinz, N. Katz, E. Lucero, C. McKenney, M. Neeley, H. Wang, E. M. Weig, A. N. Cleland, and J. M. Martinis, "Microwave dielectric loss at single photon energies and millikelvin temperatures," *Appl. Phys. Lett.*, vol. 92, no. 11, p. 112903, 2008.

[9] S. Hailey-Dunsheath, P. S. Barry, C. M. Bradford, G. Chattopadhyay, P. Day, S. Doyle, M. Hollister, A. Kovacs, H. G. LeDuc, N. Llombart, P. Mauskopf, C. McKenney, R. Monroe, H. T. Nguyen, R. O'Brient, S. Padin, T. Reck, E. Shirokoff, L. Swenson, C. E. Tucker, and J. Zmuidzinas, "Optical Measurements of SuperSpec: A Millimeter-Wave On-Chip Spectrometer," *J. Low Temp. Phys.*, vol. 176, no. 5-6, pp. 841–847, 2014.

[10] A. Endo, C. Sfiligoj, S. J. C. Yates, J. J. A. Baselmans, D. J. Thoen, S. M. H. Javadzadeh, P. P. van der Werf, A. M. Baryshev, and T. M. Klapwijk, "On-chip filter bank spectroscopy at 600–700 GHz using NbTiN superconducting resonators," *Appl. Phys. Lett.*, vol. 103, no. 3, p. 032601, 2013.

[11] J. Gao, A. Vayonakis, O. Noroozian, J. Zmuidzinas, P. K. Day, H. G. Leduc, B. Young, B. Cabrera, and A. Miller, "Measurement of loss in superconducting microstrip at millimeter-wave frequencies," in *The Thirteenth International Workshop on Low Temperature Detectors — LTD13*, (Stanford (California)), pp. 164–167, 2009.

[12] M. Molina-Ruiz, Y. J. Rosen, H. C. Jacks, M. R. Abernathy, T. H. Metcalf, X. Liu, J. L. DuBois, and F. Hellman, "Origin of mechanical and dielectric losses from two-level systems in amorphous silicon," *Phys. Rev. Mater.*, vol. 5, no. 3, p. 035601, 2021.

[13] J. J. A. Baselmans, B. T. Buijtendorp, and A. Endo, "Low-loss dielectric for high frequency cryogenic applications," Jan. 2021.

[14] H. Shanks, W. Kamitakahara, J. McClelland, and C. Carlone, "Phonon density of states of amorphous silicon," *Journal of Non-Crystalline Solids*, vol. 59–60, pp. 197–200, Dec. 1983.

Appendix A

Transfer-matrix method

We used the transfer-matrix method (TMM) to model the Fourier-transform (infrared) spectroscopy transmission through our samples. Furthermore, the TMM was used for the analysis of the ellipsometry data. The TMM is a popular method to determine the transmission (or reflection) resulting from the interaction of an incoming light wave with an arbitrary stack of dielectrics [1, 2]. The TMM is based on the Fresnel equations:

$$\begin{aligned} r_{\mathrm{s}} &= \frac{n_1 \cos\theta_1 - n_2 \cos\theta_2}{n_1 \cos\theta_1 + n_2 \cos\theta_2}, \qquad r_{\mathrm{p}} = \frac{n_2 \cos\theta_1 - n_1 \cos\theta_2}{n_2 \cos\theta_1 + n_1 \cos\theta_2} \\ t_{\mathrm{s}} &= \frac{2n_1 \cos\theta_1}{n_1 \cos\theta_1 + n_2 \cos\theta_2}, \qquad t_{\mathrm{p}} = \frac{2n_1 \cos\theta_1}{n_2 \cos\theta_1 + n_1 \cos\theta_2} \end{aligned}, \tag{A.1}$$

where r is the reflection coefficient of the total layer stack, t is the transmission coefficient of the total layer stack, and the subscripts s and t stand for S-polarized and P-polarized respectively. The θ_1 and θ_2 are the angles with respect to the normal of the interface, of the incoming and outgoing rays respectively. The r and t coefficients are also referred to as the Fresnel coefficients.

In general there are N layers, including the semi-infinitely thick vacuum layers on both sides of the FTIR sample. This means that a thin film on a substrate is modeled with four layers in the TMM, as we show in Fig. A.1. Here, $a_{\mathrm{f,n}}$ is the amplitude of the forward traveling wave, and $a_{b,n}$ is the amplitude of the backward traveling wave, at the interface between the layers n and $n-1$, at the side of layer n of the interface. In a typical FTIR experiment the light enters the sample from only one direction, and the light which is transmitted through the sample is not reflected back towards the sample. In

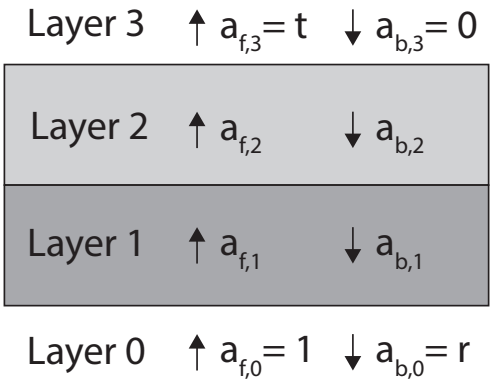

Figure A.1: Schematic of the TMM method for a four-layer stack, as is the case for a deposited dielectric film on a substrate. Here, layers 0 and 3 are the air inside the sample chamber.

this case:

$$a_{\mathrm{f,N-1}} \equiv t, \qquad a_{\mathrm{b,N-1}} = 0, \qquad a_{\mathrm{f,0}} \equiv 1, \qquad a_{\mathrm{b,0}} \equiv r. \tag{A.2}$$

The $a_{\mathrm{f,n+1}}$ and the $a_{\mathrm{b,n}}$ are related to the $a_{\mathrm{f,n}}$ and $a_{\mathrm{b,n+1}}$ through the Fresnel coefficients:

$$\begin{aligned} a_{\mathrm{f},n+1} &= \left(a_{\mathrm{f},n} e^{i\delta_{\mathrm{n}}}\right) t_{n,n+1} + a_{\mathrm{b},n+1} r_{n+1,n} \\ a_{\mathrm{b},n} e^{-i\delta_n} &= a_{\mathrm{b},n+1} t_{n+1,n} + \left(a_{\mathrm{f},n} e^{i\delta_n}\right) r_{n,n+1} \end{aligned}, \tag{A.3}$$

where $\delta_n = d_n \hat{k}_n$, with d_n the thickness of layer n and $\hat{k}_n$ the complex wave number of the forward traveling wave in layer n, and $r_{i,j}$ and $t_{i,j}$ are the reflection and transmission coefficients respectively, at the interface of layers i and j, when traveling in the direction of i to j. If the incoming light is pointed perfectly normal with respect to the sample interface, the $\hat{k}_n = \frac{2\pi\hat{n}}{\lambda}$, with λ the wavelength in vacuum and $\hat{n}$ the complex refractive index:

$$\hat{n} = n + ik, \tag{A.4}$$

where n is the refractive index and k is the extinction coefficient. We can write:

$$\begin{pmatrix} a_{\mathrm{f},n} \\ a_{\mathrm{b},n} \end{pmatrix} = M_n \begin{pmatrix} a_{\mathrm{f},n+1} \\ a_{\mathrm{b},n+1} \end{pmatrix}, \tag{A.5}$$

where the identities $r_{a,b} = -r_{b,a}$ and $t_{a,b}t_{b,a} - r_{a,b}r_{b,a} = 1$ (resulting from Eq. (A.1)) need to be used. The M_n are defined as:

$$M_n \equiv \begin{pmatrix} e^{-i\delta_n} & 0 \\ 0 & e^{i\delta_n} \end{pmatrix} \begin{pmatrix} 1 & r_{n,n+1} \\ r_{n,n+1} & 1 \end{pmatrix} \frac{1}{t_{n,n+1}}. \tag{A.6}$$

The transfer matrix $\bar{M}$ is defined as:

$$\begin{pmatrix} 1 \\ r \end{pmatrix} = \bar{M} \begin{pmatrix} t \\ 0 \end{pmatrix}, \tag{A.7}$$

and is given by the equation:

$$\bar{M} = \frac{1}{t_{0,1}} \begin{pmatrix} 1 & r_{0,1} \\ r_{0,1} & 1 \end{pmatrix} M_1 M_2 \dots M_{N-2}. \tag{A.8}$$

Finally the transmission coefficient t and the reflection coefficient r can be determined from the transfer matrix:

$$t = 1/\bar{M}_{0,0}, \qquad r = \bar{M}_{1,0}/\bar{M}_{0,0}. \tag{A.9}$$

Bibliography

[1] T. G. Mackay, *The Transfer-Matrix Method in Electromagnetics and Optics*. Synthesis Lectures on Electromagnetics, Springer Cham, 1 ed., Apr. 2020.

[2] A. Luce, A. Mahdavi, F. Marquardt, and H. Wankerl, "TMM-Fast, a transfer matrix computation package for multilayer thin-film optimization: Tutorial," *Journal of the Optical Society of America A*, vol. 39, p. 1007, June 2022.

Appendix B

FTIR analysis of c-Si substrate

We used the methodology described in Subsection 2.4.1 to measure the $\hat{n}$ of a blank c-Si wafer, which came from the same wafer box as the substrates which were used to fabricate the a-Si:H and a-SiC:H samples described in Section 2.4. This allowed us to model the samples including the substrates using the transfer-matrix method (TMM), thereby allowing us to isolate substrate and film data in the subsequent FTIR experiments of Section 2.4. For the c-Si substrate we assumed a frequency-independent infrared refractive index value $n = 3.42$ [1]. In Fig. B.1 we present the measured substrate transmission.

We observed that the measured substrate transmission decreases with increasing frequency. This effect could not be reproduced by our TMM model, even when a small frequency-dependence [2, 3] of the substrate n would be included in the model. Therefore, we performed a baseline correction to account for unknown optical effects which are not included in the model. For this purpose we fitted a linear slope (red dashed line in Fig. B.1) to the measured substrate transmission (orange curve in Fig. B.1) in the wavelength range denoted by the black vertical dashed lines in Fig. B.1. Since the baseline fit was only possible in a wavelength range without absorption features, we extrapolated the baseline fit to the frequencies outside the fitting range. Subsequently, we divided the substrate transmission data (orange curve in Fig. B.1) by the quotient of the baseline fit (red dashed line in Fig. B.1) and the calculated substrate transmission (blue line in Fig. B.1, where we used $n = 3.42$ and $k = 0$) to obtain the baseline adjusted substrate measurement data (green curve in Fig. B.1) which we used for the subsequent analysis of the substrate.

Finally, we determined the substrate's extinction coefficient k as a function of wavelength by performing a point-by-point fit of the TMM model to the

B

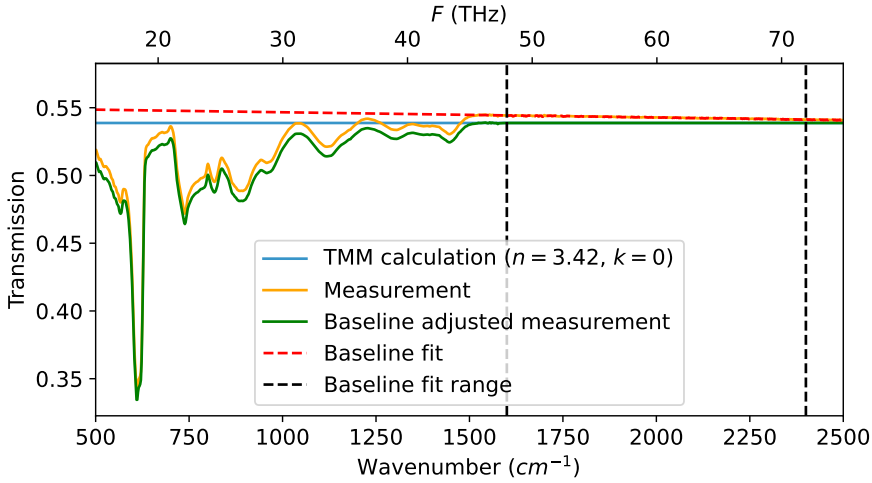

Figure B.1: FTIR transmission of the c-Si substrate. A baseline adjustment was applied to the transmission data to account for optical effects which are not included in our transfer-matrix method (TMM) model. Here, the measured transmission was corrected by a linear slope which was determined within the wavenumber range denoted by the vertical dashed lines.

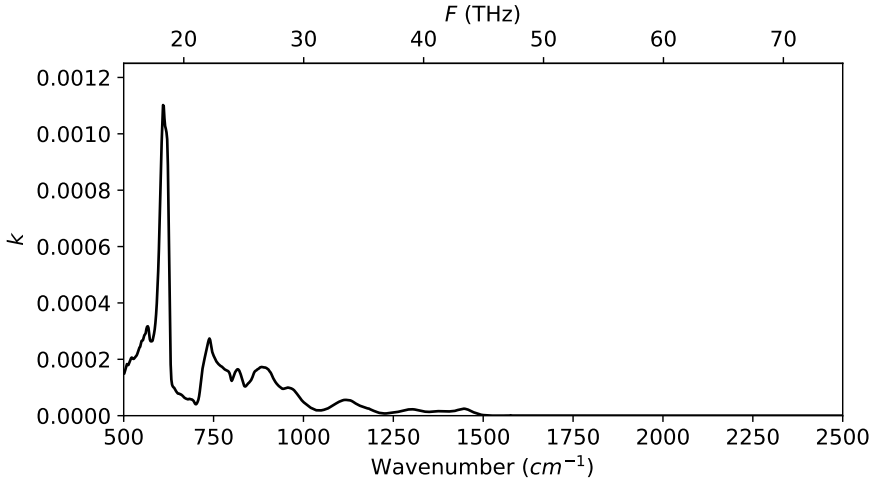

Figure B.2: Extinction coefficient k of the c-Si substrate, determined from a point-by-point fit of the TMM model to the measured FTIR transmission of the substrate. Based on literature [1] we assumed a constant infrared refractive $n = 3.42$ for the c-Si substrate.

baseline-corrected transmission data. The resulting substrate k (presented in Fig. B.2) together with the substrate $n = 3.42$ were used in Section 2.4 for the TMM modeling of the FTIR samples with the deposited dielectrics.

Bibliography

[1] A. A. Langford, M. L. Fleet, B. P. Nelson, W. A. Lanford, and N. Maley, "Infrared absorption strength and hydrogen content of hydrogenated amorphous silicon," *Physical Review B*, vol. 45, pp. 13367–13377, June 1992.

[2] D. F. Edwards and E. Ochoa, "Infrared refractive index of silicon," *Applied Optics*, vol. 19, p. 4130, Dec. 1980.

[3] E. J. Wollack, G. Cataldo, K. H. Miller, and M. A. Quijada, "Infrared properties of high-purity silicon," *Optics Letters*, vol. 45, p. 4935, Sept. 2020.

Appendix C

Additional ellipsometry data

In this appendix we present the ψ and Δ (Eq. (2.8)) values measured by ellipsometry for the a-Si:H film deposited with $T_{\text{sub}} = 250°\text{C}$ and for the a-SiC:H film. The analysis and results are presented in Section 2.6). We plotted the measurement performed at an angle of incidence $\theta = 60°$ in the 1–4 eV range (242–967 THz). In addition tot the measurement for $\theta = 60°$, we measured at θ values of at 45°, 55°, 65°, 70° and 75°. The data of all θ values were fitted together in a single fitting procedure. The mean squared errors of the models to the measured ψ and Δ for θ values other than 60° were similar to that of $\theta = 60°$.

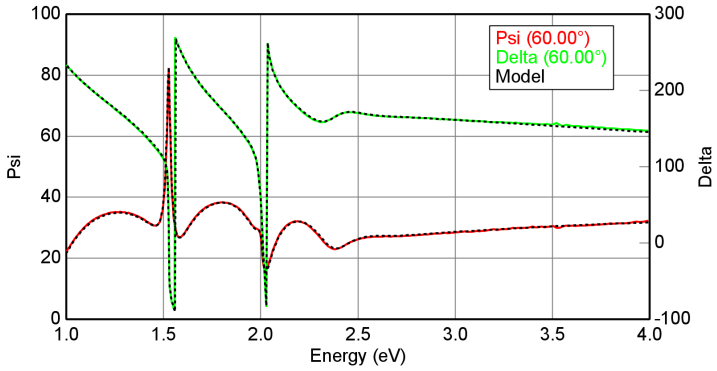

Figure C.1: The measured ψ (red curve) and Δ (green curve) of the a-Si:H film deposited with $T_{\text{sub}} = 250°\text{C}$ which we analyzed in Section 2.6, measured at an angle of incidence $\theta = 60°$. The black dashed curve represents the model calculation.

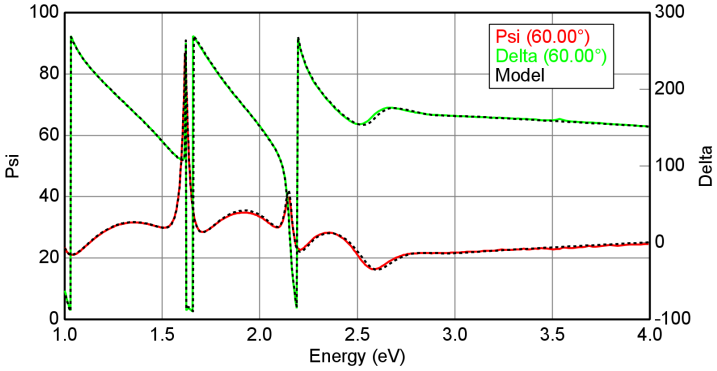

Figure C.2: The measured ψ (red curve) and Δ (green curve) of the a-SiC:H film which we analyzed in Section 2.6, measured at an angle of incidence $\theta = 60°$. The black dashed curve represents the model calculation.

Appendix D

Low-power microwave loss measurement setup design

To measure the microwave loss tangent at very low readout powers, it is necessary to optimize the signal to noise ratio of the measurement setup by adding low-noise amplifiers (LNAs) at room temperature before the vector network analyzer (VNA). Furthermore, a variable attenuator (VA) is needed to prevent the LNAs from reaching the P1dB compression point (with 10 dBm margin) where the LNA's become nonlinear. Additionally, a switch can be used to bypass some of the LNAs, to prevent subsequent LNAs from reaching the P1dB compression point when the VA has reached its maximum attenuation. In Fig. D.1 we show a schematic of the *Hydra* setup in Delft, which includes the VNA, the dilution refrigerator and the cabling.

We searched for the optimal configuration for the number of LNAs n_1 before the VA, and the number of if LNAs n_2 after the VA. Furthermore, since the VA has a maximum attenuation of 62 dB we checked if it is necessary to use a switch to bypass the LNAs before the VA when using high VNA powers, to prevent reaching the P1dB compression point. To compare different configurations we compared the signal-to-noise ratios (SNRs):

$$\mathrm{SNR} = \frac{P_{\mathrm{source}}}{k_{\mathrm{B}} T_{\mathrm{N}}} \sqrt{\frac{\tau}{B}}, \tag{D.1}$$

where P_{source} is the source power, which is equal to the readout power, and where B is the VNA's IF bandwidth and τ is the VNAs integration time. For B we assumed a value of 750 Hz and for $1/\tau$ we assumed a value of 1 kHz. We emphasize that the comparative analysis holds independently of

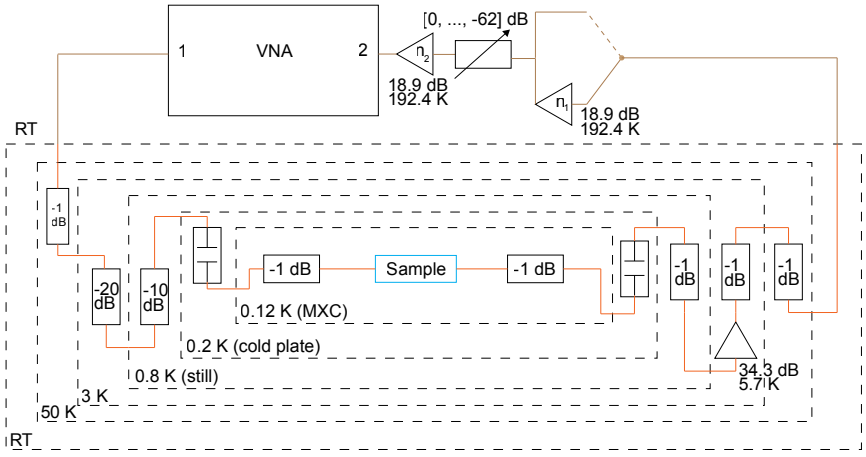

Figure D.1: Schematic of the Hydra cryostat in the Cryo Lab in Delft. In addition to the standard setup, we have added a variable attenuator (VA) and low-noise amplifiers (LNAs) at room temperature. The variable attenuator can be programmed to change with the vector network analyzer (VNA) power. In this appendix we describe how the number n_1 of amplifiers before the VA and the number n_2 of amplifiers after the VA were determined to achieve optimal performance. We determined that the optimum equals $n_1 = 2$ and $n_2 = 2$. Additionally, we checked if it would be beneficial to add a switch to the LNAs before the VA, so that these amplifiers can be bypassed for higher VNA powers. We concluded that the switch is not necessary in this setup. In this diagram the orange lines represent CuNi coax cables, and the brown lines represent Cu coax cables.

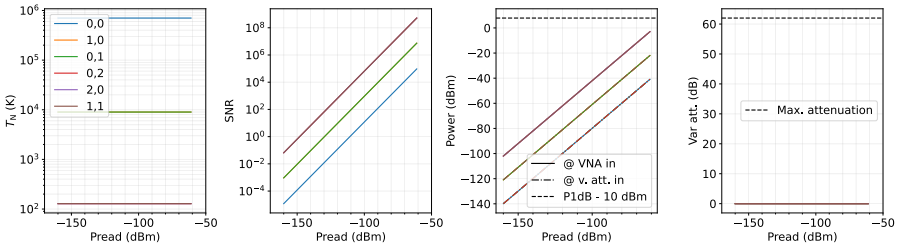

Figure D.2: Comparison of configurations with a total number of 0, 1, or 2 LNAs.

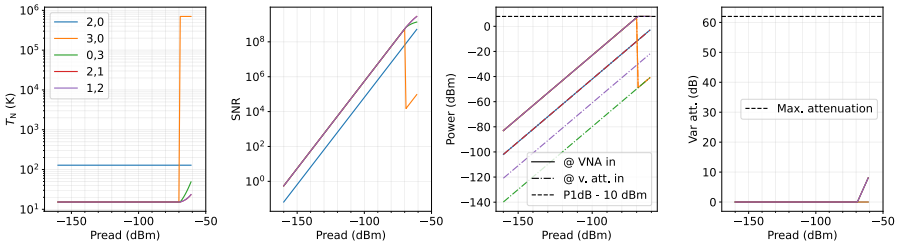

Figure D.3: Comparison of configurations with a total number of 2 or 3 LNAs.

these numbers, since one can choose to compare the total (cascaded) noise temperature T_{N}. The noise temperature T_{N} of a cascade of n elements, each with their own noise temperature and gain, can be calculated using the Friis equation:

$$T_{\mathrm{N}} = T_{\mathrm{N},1} + \frac{T_{\mathrm{N},2}}{G_1} + \frac{T_{\mathrm{N},3}}{G_1 G_2} + \cdots + \frac{T_{\mathrm{N,n}}}{G_1 G_2 \cdots G_{n-1}}, \tag{D.2}$$

where $T_{\mathrm{N},i}$ is the noise temperature of element i and where G_i is the gain of element i. In the situation as drawn in Fig. D.1 the first element is de 1 dB attenuator after the sample, and the last element is the last LNA before the signal reaches port 2 of the VNA. The effective noise temperature of an attenuator $T_{\mathrm{N,att}}$ can be calculates as:

$$T_{\mathrm{N,att}} = T\,(L-1)\,, \tag{D.3}$$

where T is the physical temperature of the attenuator and where L is the linear attenuation factor.

In Fig. D.2 we plotted the comparison of the configurations with a total number of 0, 1 or 2 LNAs. Out of these three options, the best SNR is achieved

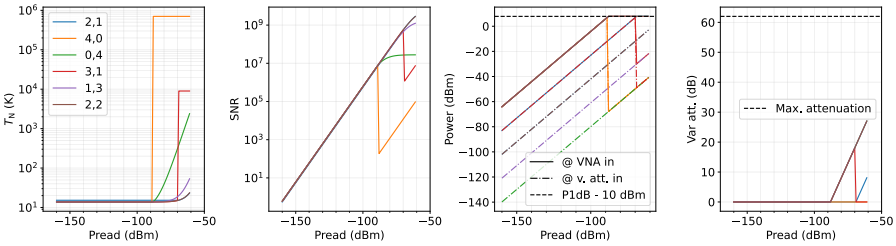

Figure D.4: Comparison of configurations with a total number of 3 or 4 LNAs.

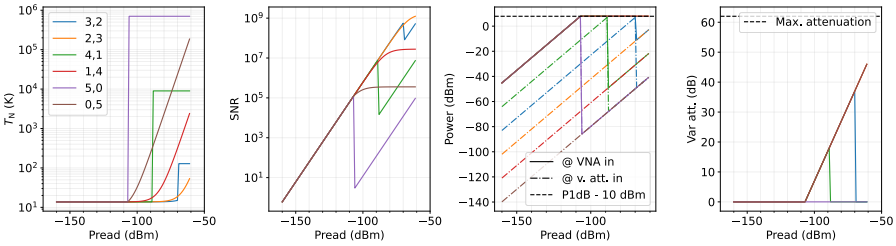

Figure D.5: Comparison of configurations with a total number of 5 LNAs.

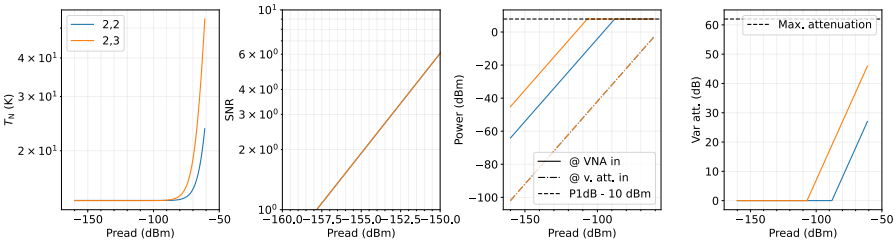

Figure D.6: Comparison of configuration ($n_1 = 2$, $n_2 = 3$) with ($n_1 = 2$, $n_2 = 2$).

with 2 LNAs. In Fig. D.3 we compared configurations with a total number of 2 or 3 LNAs. where we concluded that we can achieve a better SNR with 3 LNAs than with 2 LNAs. The ($n_1 = 3$, $n_2 = 0$) configuration is the only configuration that triggers the switch. In Fig. D.4 we compared configurations with a total number of 3 or 4 LNAs. We conclude that the best SNR can be achieved with a total number of 4 LNAs., and here the best configuration is ($n_1 = 2$, $n_2 = 2$) . In Fig. D.5 we compare the possible configurations with a total number of 5 LNAs, where we concluded that the ($n_1 = 2$, $n_2 = 3$) is the best configuration when using 5 LNAs. Finally, in Fig. D.6 we compare the ($n_1 = 2$, $n_2 = 3$) with the ($n_1 = 2$, $n_2 = 2$) configuration. We note that the switch is not necessary in both configurations. We conclude that the ($n_1 = 2$, $n_2 = 3$) configuration provides no benefit over the ($n_1 = 2$, $n_2 = 2$) configuration, and therefore the optimal configuration is ($n_1 = 2$, $n_2 = 2$).

Appendix E

Internal mm-submm power in Fabry-Pérot resonators

To rule out that the observed frequency dependence of the mm-submm loss tangent that is presented in Chapter 3 is a result of the saturation of two-level systems (TLSs), we determined the correlation between the internal quality factors Q_i of the Fabry-Pérot (FP) resonators and the mm-submm internal powers $P_\mathrm{int,FP}$ circulating inside the FP resonators. TLS saturation would lead to a positive correlation between Q_i and $P_\mathrm{int,FP}$ [1].

We determined the Q_i of each FP peak as:

$$\frac{1}{Q_\mathrm{i}} = \frac{1}{Q} - \frac{1}{Q_\mathrm{c}}, \tag{E.1}$$

where Q is the loaded quality factor, which we determined from the full-width at half-maxima of the FP peaks. Q_c is the coupling quality factor (accounting for power leaking out of both couplers), which equals $Q_\mathrm{c} = nQ_\mathrm{c,1}$. Here n is the mode number of the FP peak and $Q_\mathrm{c,1} = \pi/|t_\mathrm{c}|^2$, with t_c the transmission coefficient of a single coupler [2]. We measured the $Q_\mathrm{c,1}$ values at the center frequencies of each of the four frequency bands, according to the method that is explained in the main text. The frequency bands are visible in the legend of Fig. 1. The $Q_\mathrm{c,1}$ is frequency dependent and therefore we approximated the $Q_\mathrm{c,1}$ values of the individual peaks by fitting a polynomial to the four measured $Q_\mathrm{c,1}$ values versus frequency f. The Q_i versus f for all four FPs combined is shown in Fig. 1a. Each point represents a single FP peak and the different colors (and markers) denote the frequency bands that were used in the main text to partition the data set. We calculated the Pearson correlation coefficient

for all frequency bands combined. Since the TLS-induced loss tangent has a power law dependence on power [1], we calculated all correlation coefficients in this supplemental text on a log-log scale. We observe a correlation ($|\rho| > 0.46$) of $\ln(Q_\mathrm{i})$ with $\ln(f)$.

Due to internal losses in the FPs, the circulating internal power $P_\mathrm{int,FP}$ of the FPs is not equal over the length of the resonator [3]. We define $P_\mathrm{int,FP}$ as the power that flows inside the FP in the direction of the microwave kinetic inductance detector (MKID), at the MKID end of the FP. The $P_\mathrm{int,FP}$ is composed of power coming from the mm-submm photomixer source, plus thermal power $P_\mathrm{int,thermal}$ from the 300-K black-body radiation seen by the antenna: $P_\mathrm{int,FP} = P_\mathrm{int,source} + P_\mathrm{int,thermal}$. The relation between $P_\mathrm{int,FP}$ and the power P_MKID that flows out of the FP towards the MKID is [3]:

$$P_\mathrm{int,FP} = P_\mathrm{MKID} \frac{Q_\mathrm{c,1}}{\pi}. \tag{E.2}$$

We can use Eq. E.2 to determine $P_\mathrm{int,source}$, since the MKID measures the frequency response relative to the thermal base load and therefore only measures the power $P_\mathrm{MKID,source}$ at the MKID that comes from the photomixer source. We corrected the MKID's frequency response for stray light by subtracting the frequency response of an MKID which is not connected to an FP resonator. We find that the MKID frequency responses $\frac{df_\mathrm{0,MKID}}{f_\mathrm{0,MKID}}$ corresponding to the intensities of the FP peaks approximately have a log-normal distribution with a geometric mean of 10^{-5}. To estimate the responsivity of our MKIDs we used a previously performed calibration measurement on similar Al-NbTiN MKIDs [4], accounting for a factor 0.7 difference in responsivity due to differences in the Al volume and the kinetic inductance fraction. We estimate that our MKIDs have a responsivity $\frac{df_\mathrm{0,MKID}}{f_\mathrm{0,MKID}}/dP$ of 1.7×10^8 (W^{-1}), corresponding to a geometric mean of $P_\mathrm{KID,source}$ on the order of 0.1 pW.

In Fig. 1b we show the Q_i versus $P_\mathrm{int,source}$. The positive correlation $|\rho| < 0.10$ between $\ln(Q_\mathrm{i})$ and $\ln(P_\mathrm{int,source})$, This correlation is significantly smaller than the observed correlation between $\ln(Q_\mathrm{i})$ and $\ln(f)$.

To determine the thermal power that is incident at the FP, we calculated the power spectral density (PSD) using a radiation transfer calculation that accounts for the optical efficiency of the full optics stack and for reflections in the cryostat window. The resulting thermal power incident at the FP $P_\mathrm{inc,thermal}$ is roughly 0.1 pW integrated over a FP peak. On-resonance, the relation between the power that is incident at the FP resonator P_inc to the $P_\mathrm{int,FP}$ is [3]:

$$P_{\mathrm{int,FP}} = P_{\mathrm{inc}} \frac{(\frac{\pi}{Q_{\mathrm{c,1}}}) e^{-\frac{n\pi}{Q_{\mathrm{i}}}}}{(1-(1-\frac{\pi}{Q_{\mathrm{c,1}}}) e^{-\frac{n\pi}{Q_{\mathrm{i}}}})^2}. \tag{E.3}$$

We used Eq. E.3 to calculate the $P_{\mathrm{int,thermal}}$ from the $P_{\mathrm{inc,thermal}}$. Then we calculated $P_{\mathrm{int,FP}} = P_{\mathrm{int,source}} + P_{\mathrm{int,thermal}}$. In Fig. 1c we show the Q_{i} versus $P_{\mathrm{int,FP}}$. We find a small and positive correlation coefficient $|\rho| < 0.13$ between $\ln(Q_{\mathrm{i}})$ and $\ln(P_{\mathrm{int,FP}})$. We note that a small positive correlation between $\ln(Q_{\mathrm{i}})$ and $\ln(P_{\mathrm{int,FP}})$ as well as between $\ln(Q_{\mathrm{i}})$ and $\ln(P_{\mathrm{int,source}})$ is expected if the dielectric loss increases with frequency. This is because the higher frequencies in this experiment correspond with lower powers due to the 400 GHz low-pass filter present in the optical stack.

To conclude, we find a significant negative Pearson correlation coefficient $|\rho| > 0.46$ between Q_{i} and f. We rule out that the observed frequency dependence of the mm-submm loss tangent is due to saturation of TLSs, since we observe a significantly smaller correlation coefficient between Q_{i} and $P_{\mathrm{int,FP}}$.

Bibliography

[1] J. Gao, *The Physics of Superconducting Microwave Resonators*. PhD thesis, California Institute of Technology, 2008.

[2] S. Hähnle, K. Kouwenhoven, B. Buijtendorp, A. Endo, K. Karatsu, D. Thoen, V. Murugesan, and J. Baselmans, "Superconducting Microstrip Losses at Microwave and Submillimeter Wavelengths," *Phys. Rev. Appl.*, vol. 16, no. 1, p. 014019, 2021.

[3] M. Pollnau and M. Eichhorn, "Spectral coherence, Part I: Passive-resonator linewidth, fundamental laser linewidth, and Schawlow-Townes approximation," *Progress in Quantum Electronics*, vol. 72, Aug. 2020.

[4] A. Endo, K. Karatsu, A. P. Laguna, B. Mirzaei, R. Huiting, D. J. Thoen, V. Murugesan, S. J. C. Yates, J. Bueno, N. van Marrewijk, S. Bosma, O. Yurduseven, N. Llombart, J. Suzuki, M. Naruse, P. J. de Visser, P. P. van der Werf, T. M. Klapwijk, and J. J. A. Baselmans, "Wideband on-chip terahertz spectrometer based on a superconducting filterbank," *J. Astron. Telesc. Instrum. Syst.*, vol. 5, p. 1, June 2019.

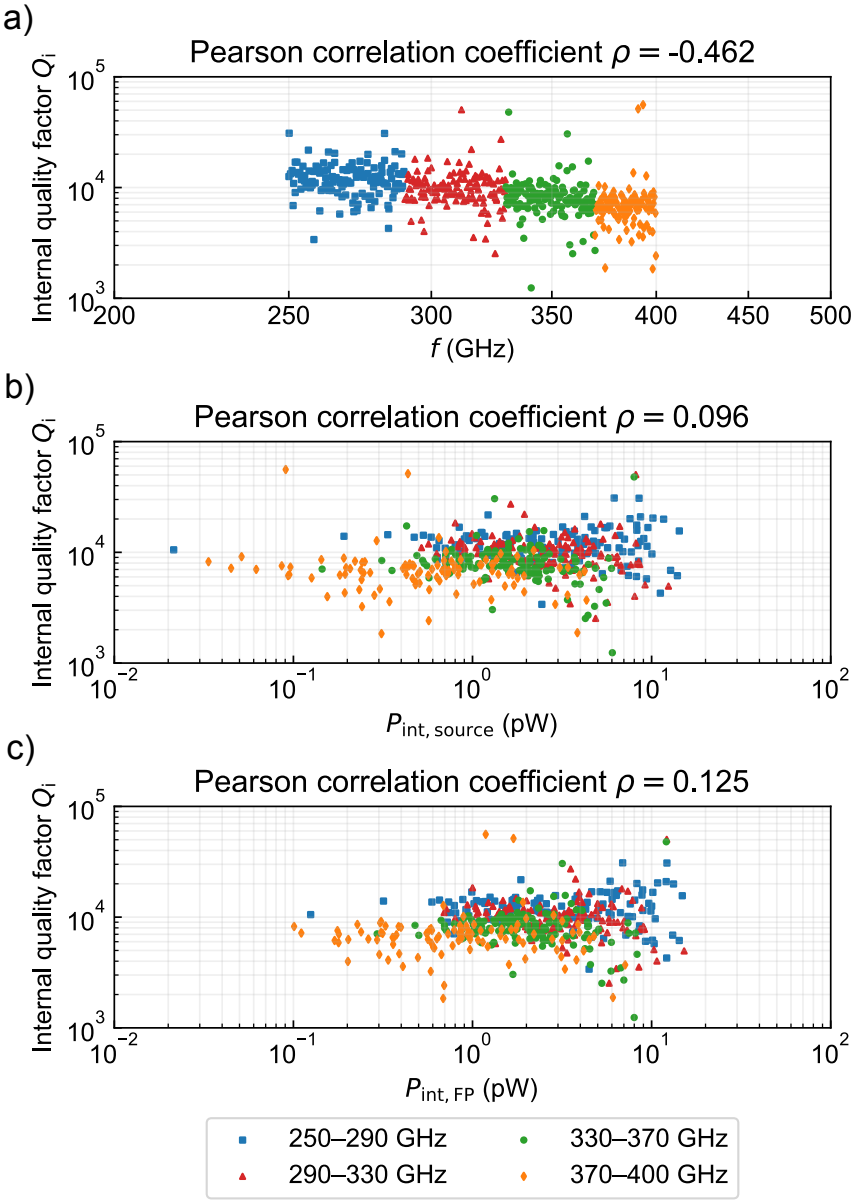

Figure E.1: a) Q_i versus f. The title shows the correlation coefficient of $\ln(Q_\mathrm{i})$ and $\ln(f)$. b) Q_i versus $P_\mathrm{int,source}$. The title shows the correlation coefficient of $\ln(Q_\mathrm{i})$ and $\ln(P_\mathrm{int,source})$. c) Q_i versus $P_\mathrm{int,FP}$. The title shows the correlation coefficient of $\ln(Q_\mathrm{i})$ and $\ln\left(P_\mathrm{int,FP}\right)$.

Appendix F

Additional mm-submm quality factor data and microwave loss data

In this appendix we present the additional measurement data of Chapter 3. In Fig. F.1 we show the mm-submm Q versus n data of chip 2, which was fabricated on the same wafer as chip 1. In Fig. F.2 we plot the $Q_{c,1}$ values of chips 1 and 2, which we obtained from the fits of Eq. (3.1) to the Q versus n data. In Fig. F.3 we plot the microwave $\tan\delta$ versus N data of chip 3, which was fabricated on the same wafer as chip 1.

Bibliography

[1] M. S. Khalil, M. J. A. Stoutimore, F. C. Wellstood, and K. D. Osborn, "An analysis method for asymmetric resonator transmission applied to superconducting devices," *J. Appl. Phys*, vol. 111, no. 5, p. 054510, 2012.

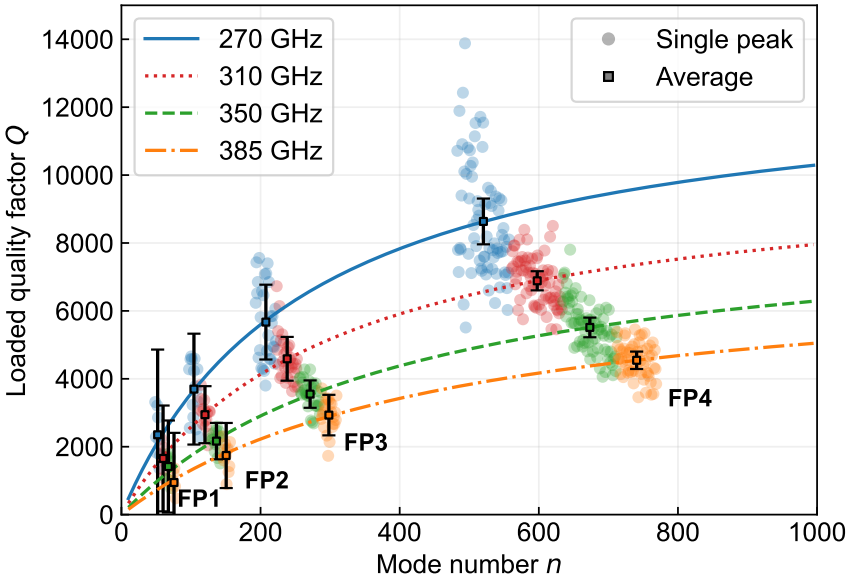

Figure F.1: Loaded quality factor Q versus mode number n of the Fabry-Pérot resonators (FP1–4) of chip 2. The curves are fits of Eq. 3.1 to the average Q and average n values. The error bars represent 30 standard errors (±30 SE) in Q and the $1/SE$ were used as fitting weights.

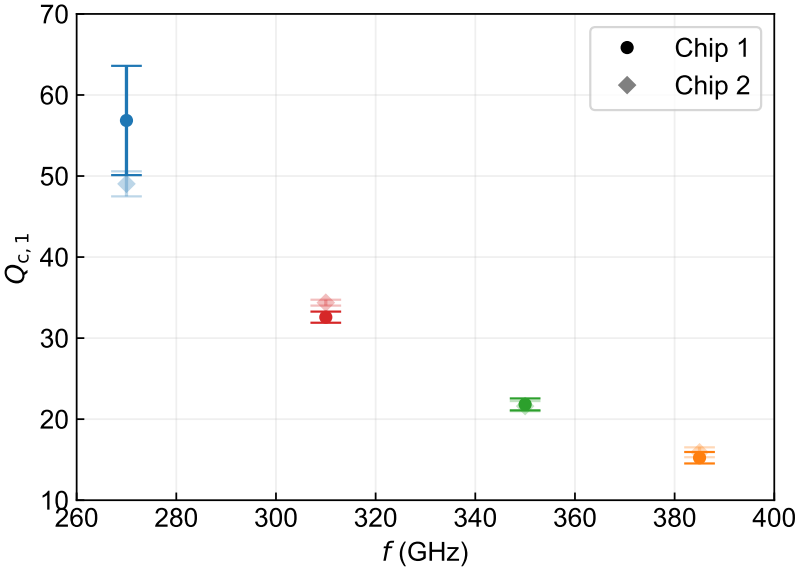

Figure F.2: The FP coupler's $Q_{c,1}$ versus frequency for chips 1 and 2, obtained from the fit of the Q versus n data to Eq. (3.1). The error bars represent one standard deviation ($\pm\sigma$).

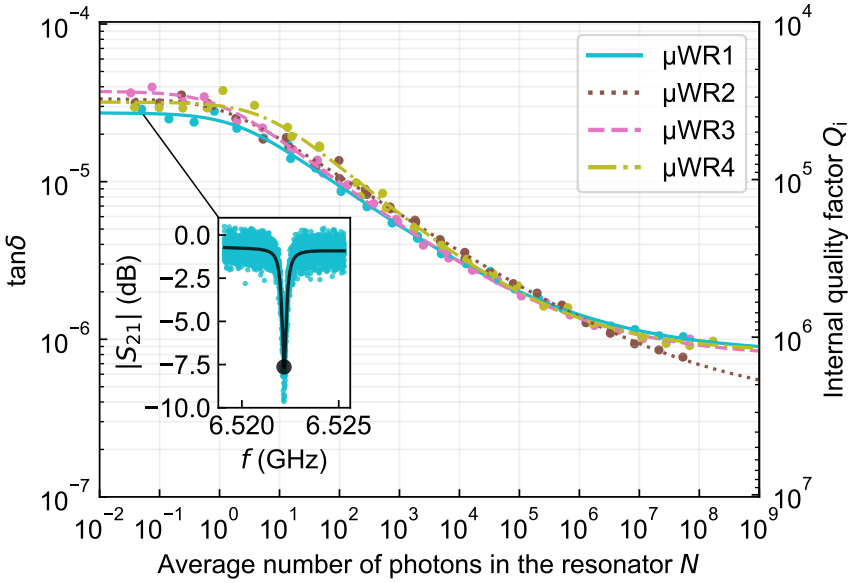

Figure F.3: Measured microwave $\tan\delta = 1/(pQ_i)$ versus average number of photons in the resonators μWR1–4 of chip 3. The curves are fits to Eq. 4.2. The inset illustrates how $\tan\delta$ is obtained at each power, by fitting the $|S_{21}|$ dips using the model in Ref. [1]. The $\tan\delta_0$ are obtained by fitting the $\tan\delta$ versus N curves to Eq. 4.2.

Appendix G

Wide-band Fabry-Pérot design

The Fabry-Pérot (FP) chip which we used to measure the loss of the a-SiC:H in the 270–385 GHz range (Chapter 3) made use of twin-slot antennas centered around 350 GHz. To study the origin of the mm-submm loss (Chapter 4) we aimed for a measurement range of 225–900 GHz. To extend the measurable frequency range, we replaced the twin-slot antennas by leaky-wave antennas. In the wide frequency band of 225–900 GHz it is not trivial that the measurement method will work with a single chip design (i.e. that the method will return the correct Q_i values). This is because (1) The FP peaks need to be wide enough to be measurable using the photomixer source, which has a minimum frequency resolution of 20 MHz. (2) The peak transmission scales with Q/Q_c and therefore we want the Q_c not to be too large in comparison with Q_i to prevent very weak peaks. (3) The peak spacing f_0 should be large enough compared to the FWHM to be able to fit the individual FP peaks. In the rest of this appendix we elaborate on how these three issues were taken into account in the design of the FP resonators, and we show the results of a simulation that we used to validate the design. We note that since the Q_c is dependent on the coupler geometry as well as on the FP resonator lengths, we first chose a coupler geometry and then determined the FP resonator lengths that satisfy our design requirements. For the coupler overlap length we chose 22 μm, which is the same length as in previous designs.

(1) The FP peaks need to be wide enough to be measurable using the photomixer source, which has a minimum frequency resolution of 20 MHz. The fitted Lorentzian function (which includes a baseline signal value, for example due to stray light) has four fitting parameters. Therefore we would theoretically need at least 5 data points to be able to fit this function.

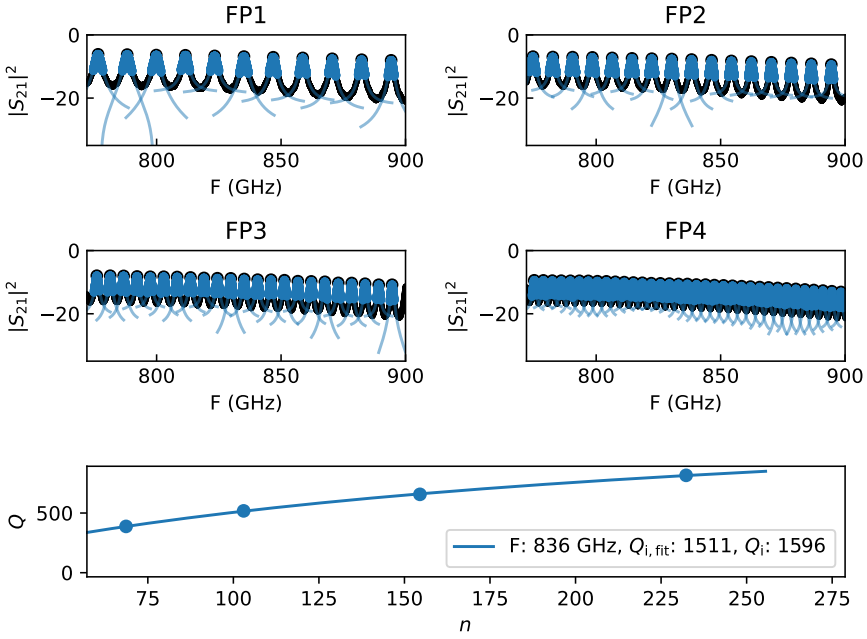

Figure G.1: Simulated data and fitting in the 776–900 GHz range for FP1–4. In the legend, $Q_{i,fit}$ refers to the value obtained from the fitting and Q_i refers to the value which was entered into the simulation.

However, we decided to place a requirement of at least 10 data points above the noise floor. From previous measurements on Fabry-Pérot chips we estimated that the noise floor due to stray light is roughly 30 dB below the average peak intensity. Therefore, we expect that we are unable to measure peaks which are narrower than 180 MHz at −30 dB. This corresponds to $\gamma = \frac{180/2}{\sqrt{1000-1}} = 2.85$ MHz, which means that the maximum Q at 225 GHz equals 4×10^4. Based on previous measurements we estimate the Q_i at 225 GHz to be 1.6×10^4. Therefore, within the frequency band of 225–900 GHz it is expected that the 20 MHz frequency resolution of the photomixer source does not pose a problem for our measurements.

(2) The peak transmission scales with Q/Q_c and therefore we want the Q_c not to be too large in comparison with Q_i. We have chosen to demand that $Q_\mathrm{c} < 9Q_\mathrm{i}$, such that we get at least 10% of the maxium peak transmission. Based on previous measurements we estimated the Q_i of the a-SiC:H to be 1.4×10^3 at 900 GHz. This means that at 900 GHz we need to have $Q_\mathrm{c} < 1.3 \times 10^4$ and at 225 GHz we need to have $Q_\mathrm{c} < 1.4 \times 10^5$.

(3) The peak spacing f_0 should be large enough compared to the FWHM to be able to fit the individual FP peaks. Fundamentally, the limit for this is called the Taylor criterion: $f_0 \geq \mathrm{FWHM}$. This concern is only relevant at the high frequency end of the measurement bandwidth, where the Q_i is expected to be the lowest. Furthermore this concern is only relevant for FP4 which has the smallest resonator length and therefore the smallest peak spacing. The Q at 900 GHz will be smaller than the estimated Q_i at 900 GHz of 1.4×10^3. Based on Sonnet simulations of the FP coupler we estimate that $Q_{\mathrm{c},1} = 5$ at 900 GHz. Choosing a mode number $n = 200$ at 900 GHz, corresponding with a peak spacing of 4.5 GHz, we have a Q_c of 1000 at 900 GHz. This corresponds with a Q of 6×10^2 at 900 GHz, and a FWHM of 1.5 GHz. Therefore, in this configuration the Taylor criterion is satisfied, with a safety margin of a factor 3.

Taking these three design considerations into account, we have chosen a design where the coupler has an overlap length of 22 μm and where the FP resonators have lengths of 3.00 mm, 4.50 mm, 6.75 mm and 10.13 mm. This design satisfies the requirements for Q_c and for the peak spacing f_0. Finally, we verified the design by fitting a a simulated dataset. The simulated data was generated using the ABCD matrix formalism. The S-parameter matrix of the FP couplers and the transmission line properties were calculated using Sonnet simulations. We plotted the simulated data in the 772–900 GHz frequency range in Fig. G.1. Over the entire frequency range of 225–900 GHz we found that the resulting errors in the fitted $Q_{\mathrm{i,fit}}$ were below 8% relative to the Q_i values that we entered into the simulation.

Appendix H

FTS fitting parameters

In this appendix we present the best-fit values for the fitting parameters of the Maxwell-Helmholtz-Drude (MHD) dispersion model. The measurements, fitting procedure, and results are described in Chapter 4.

j	Vibrational mode	$\omega_{T,j}/2\pi$ (THz)	$\Delta\varepsilon_j^{'}$	Γ_j(THz)	α_j
1	Si–C stretch	20.7	5.5×10^{-1}	4.6	**0**
2	Si–C stretch	22.8	9.8×10^{-2}	1.7	3.8×10^{-2}
3	Si–C stretch	23.9	5.8×10^{-2}	1.9	**0**
4	Si–CH_2–Si wag	28.3	9.0×10^{-3}	1.7	4.2×10^{-1}
5	Si–CH_2–Si wag	29.8	2.5×10^{-2}	1.8	**0**
6	C–H_3 symmetric bend	37.4	$\mathbf{5.0 \times 10^{-3}}$	**1.5**	2.6×10^{-6}
7	Si–CH_2–Si scissor or symmetric bend	40.3	$\mathbf{3.0 \times 10^{-3}}$	**1.5**	**0**
8	C–H_3 asymmetric bend	42.1	$\mathbf{3.0 \times 10^{-3}}$	**1.5**	**0**
9	Si–H_x stretch	62.3	2.2×10^{-2}	**4.0**	**0**
10	C–H_x stretch	**87.0**	1.1×10^{-2}	**10.0**	**0**

Table H.1: Best-fit values corresponding to the results in Fig. 4.7b, of the MHD dispersion model paramaters (Eq. 4.3). The MHD dispersion model was fitted to only the FTS-measured transmission data (Fig. 4.7a). The ε_∞ resulting from the fit equals 6.8. The values shown in bold were constrained to the listed values to reduce the number of free fitting parameters.

j	Vibrational mode	$\omega_{T,j}/2\pi$ (THz)	$\Delta\varepsilon_j'$	Γ_j(THz)	α_j
1	Si–C stretch	19.6	1.9×10^{-1}	3.1	**0**
2	Si–C stretch	22.1	4.8×10^{-1}	4.2	1.5×10^{-5}
3	Si–C stretch	23.5	3.3×10^{-2}	1.2	**0**
4	Si–CH_2–Si wag	28.5	9.3×10^{-3}	1.5	5.2×10^{-1}
5	Si–CH_2–Si wag	29.8	1.6×10^{-2}	1.2	**0**
6	C–H_3 symmetric bend	37.4	$\mathbf{5.0 \times 10^{-3}}$	**1.5**	6.2×10^{-7}
7	Si–CH_2–Si scissor or symmetric bend	40.2	$\mathbf{3.0 \times 10^{-3}}$	**1.5**	**0**
8	C–H_3 asymmetric bend	42.1	$\mathbf{3.0 \times 10^{-3}}$	**1.5**	**0**
9	Si–H_x stretch	62.3	2.3×10^{-2}	**4.0**	**0**
10	C–H_x stretch	**87.0**	1.1×10^{-2}	**10.0**	**0**

Table H.2: Best-fit values corresponding to the solid grey curve in Fig. 4.9, of the MHD dispersion model parameters (Eq. 4.3). The MHD dispersion model was fitted to the combined FTS-measured transmission data (Fig. 4.7a) and the FP-measured loss data (Fig. 4.5). The ε_∞ resulting from the fit equals 6.8. The values shown in bold were constrained to the listed values to reduce the number of free fitting parameters.

List of publications and patents

Journal papers

J1. **B.T. Buijtendorp**, A. Endo, W. Jellema, K. Karatsu, K. Kouwenhoven, D. Lamers, A. J. van der Linden, K. Rostem, M. Veen, E. J. Wollack, J. J. A. Baselmans, S. Vollebregt "Vibrational modes as the origin of dielectric loss at 0.27–100 THz in a-SiC:H", *Preprint arXiv:2405.13688v2* (May 2024)

J2. K. Kouwenhoven, G.P.J. van Doorn, **B.T. Buijtendorp**, S. A. H. de Rooij, D. Lamers, D. J. Thoen, V. Murugesan, J. J. A. Baselmans, P. J. de Visser "Geometry dependence of TLS noise and loss in a-SiC:H parallel plate capacitors for superconducting microwave resonators", *Physical Review Applied, Vol. 21, Iss. 4* (April 2024)

J3. **B.T. Buijtendorp**, S. Vollebregt, K. Karatsu, D.J. Thoen, V. Murugesan, K. Kouwenhoven, S. Hähnle, J.J.A. Baselmans, A. Endo "Hydrogenated Amorphous Silicon Carbide: A Low-Loss Deposited Dielectric for Microwave to Submillimeter-Wave Superconducting Circuits", *Physical Review Applied, Vol. 18, Issue 6* (December 2022)

J4. A. Taniguchi, T. J. L. C. Bakx, J. J. A. Baselmans, R. Huiting, K. Karatsu, N. Llombart, M. Rybak, T. Takekoshi, Y. Tamura, H. Akamatsu, S. Brackenhoff, J. Bueno, **B. T. Buijtendorp**, S. O. Dabironezare, A. Doing, Y. Fujii, K. Fujita, M. Gouwerok, S. Hähnle, T. Ishida, S. Ishii, R. Kawabe, T. Kitayama, K. Kohno, A. Kouchi, J. Maekawa, K. Matsuda, V. Murugesan, S. Nakatsubo, T. Oshima, A. Pascual Laguna, D. J. Thoen, P. P. van der Werf, S. J. C. Yates, A. Endo "DESHIMA 2.0: Development of an integrated superconducting spectrometer for science-grade astronomical observations", *Journal of Low Temperature Physics, Vol. 209* (November 2022)

J5. **B. T. Buijtendorp**, J. Bueno, D. J. Thoen, V. Murugesan, P. M. Sberna, J. J. A. Baselmans, S. Vollebregt, A. Endo "Characterization of low-loss hydrogenated amorphous silicon films for superconducting resonators", *Journal of Astronomical Telescopes, Instruments, and Systems, Vol. 8, Iss. 2* (June 2022)

J6. A. Pascual Laguna, K. Karatsu, D. J. Thoen, V. Murugesan, **B. T. Buijtendorp**, A. Endo, J. J. A. Baselmans "Terahertz band-pass filters for wideband superconducting on-chip filter-bank spectrometers", *IEEE Transactions on Terahertz Science and Technology, Vol. 11, Iss. 6* (July 2021)

J7. S. Hähnle, K. Kouwenhoven, **B. T. Buijtendorp**, A. Endo, K. Karatsu, D. J. Thoen, V. Murugesan, J. J. A. Baselmans "Superconducting microstrip losses at microwave and submillimeter wavelengths", *Physical Review Applied, Vol. 16, Iss. 1* (July 2021)

Conference presentations and proceedings

C1. **B.T. Buijtendorp**, A. Endo, R. Huisman, W. Jellema, K. Karatsu, K. Kouwenhoven, D. Lamers, A. J. van der Linden, K. Rostem, M. Veen, E. J. Wollack, J. J. A. Baselmans, S. Vollebregt "Origin of mm-submm loss in deposited dielectrics for superconducting astronomical instrumentation", *Proc. SPIE PC13102, Millimeter, Submillimeter, and Far-Infrared Detectors and Instrumentation for Astronomy XII* (June 2024)

C2. K. Kohno, A. Endo, Y. Tamura, A. Taniguchi, T. Takekoshi, S. Ikeda, N. Yoshida, K. Moriwaki, K. Karatsu, J. J. A. Baselmans, L. H. Marting, A. Moerman, **B. T. Buijtendorp**, S. O. Dabironezare, M. Rybak, T. J. L. C. Bakx, L. G. Olde Scholtenhuis, F. Steenvoorde, R. Huiting, D. J. Thoen, L. Wang, A. Simionescu, S. J. C. Yates, A. Monfardini, M. Calvo, P. P. van der Werf, S. Vollebregt, B. R. Brandl, T. Oshima, R. Kawabe, K. Fujita, S. Nakatsubo, Y. Kimura, A. Tsujita, Y. Yoshimura, K. Morokuma-Matsui, F. Egusa, T. Minamidani, S. Ishii, A. Lidz, D. Burgarella "Submillimeter-wave dual-band line intensity mapping using the Terahertz Integral Field Units with Universal Nanotechnology (TIFUUN) for the Atacama Submillimeter Telescope Experiment (ASTE)", *Proc. SPIE PC13102, Millimeter, Submillimeter, and Far-Infrared Detectors and Instrumentation for Astronomy XII* (June 2024)

C3. A. Endo, K. Karatsu, T. Takekoshi, Y. Tamura, A. Taniguchi, M. Rybak, K. Kohno, H. Akamatsu, J. Aguilera, T. J. L. C. Bakx, **B. T. Buijtendorp**, S. Cray, S. O. Dabironezare, Y. Fujii, K. Fujita, M. Hagimoto, S. Hanany, S. Hotta, R. Huiting, T. Iino, C. Imamura, S. Ishii, K. Iwakami, T. Kitayama, K. Konishi, R. Kawabe, M. Klettke, T. Kobiki, L. H. Marting, T. Matsumura, T. Minamidani, A. Moerman, K. Morokuma, V. Murugesan, S. Nakatsubo, K. Ohtawara, N. Okauchi, L. G. Olde Scholtenhuis, T. Oshima, A. Pascual Laguna, H. Sakurai, F. Steenvoorde, R. Takaku, D. J. Thoen, A. Tsujita, H. Umehata, S. Vollebregt, D. Wernicke, P. P. van der Werf, S. J. C. Yates, J. J. A. Baselmans "DESHIMA 2.0 on ASTE: The Commissioning and Science Verification of an Ultra-wideband Integrated Superconducting Spectrometer", *Proc. SPIE PC13102, Millimeter, Submillimeter, and Far-Infrared Detectors and Instrumentation for Astronomy XII* (June 2024)

C4. K. Karatsu, A. Endo, A. Moerman, S. J. C. Yates, R. Huiting, A. Pascual Laguna, S. O. Dabironezare, V. Murugesan, D. J. Thoen, H. Akamatsu, T. J. L. C. Bakx, **B T. Buijtendorp**, S. Cray, K. Fujita, S. Hanany, R. Kawabe, T. Kitayama, K. Kohno, K. Konishi, L. H. Marting, T. Matsumura, S. Nakatsubo, T. Oshima, M. Rybak, H. Sakurai, R. Takaku, T. Takekoshi, Kitami, Y. Tamura, A. Taniguchi, P. P. van der Werf, J. J. A. Baselmans "DESHIMA 2.0: full system evaluation of the ultra-wideband integrated superconducting spectrometer in laboratory", *Proc. SPIE PC13102, Millimeter, Submillimeter, and Far-Infrared Detectors and Instrumentation for Astronomy XII* (June 2024)

C5. **B. T. Buijtendorp**, A. Endo, K. Karatsu, D. J. Thoen, V. Murugesan, K. Kouwenhoven, S. Hähnle, J. J. A. Baselmans, S. Vollebregt "Low-loss a-SiC:H for superconducting microstrip lines for (sub-)millimeter astronomy", *Proc. SPIE PC12190, Millimeter, Submillimeter, and Far-Infrared Detectors and Instrumentation for Astronomy XI* (August 2022)

C6. K. Karatsu, A. Endo, S. J. C. Yates, R. Huiting, A. Moerman, A. Pascual Laguna, S. Dabironezare, V. Murugesan, D. J. Thoen, H. Akamatsu, T. J. L. C. Bakx, J. Bueno, **B. T. Buijtendorp**, Y. Fujii, K. Fujita, S. Hähnle, T. Ishida, S. Ishii, R. Kawabe, T. Kitayama, K. Kohno, A. Kouchi, N. Llombart, J. Maekawa, K. Matsuda, S. Nakatsubo, T. Oshima, M. Rybak, T. Takekoshi, Y. Tamura, A. Taniguchi, P. P. van der Werf, J. J. A. Baselmans "DESHIMA 2.0: Laboratory demonstration of the ultra-wideband integrated superconducting spectrometer", *Proc.*

SPIE PC12190, Millimeter, Submillimeter, and Far-Infrared Detectors and Instrumentation for Astronomy XI (August 2022)

C7. **B.T. Buijtendorp**, A. Endo, K. Karatsu, D.J. Thoen, V. Murugesan, K. Kouwenhoven, S. Hähnle, J.J.A. Baselmans, S. Vollebregt "Hydrogenated Amorphous Silicon Carbide: A Low-Loss Deposited Dielectric for mm-submm Astronomy," 19th International Workshop on Low Temperature Detectors (LTD19) Virtual Only Event (July 2021)

C8. **B. T. Buijtendorp**, J. Bueno, D. J. Thoen, V. Murugesan, P. M. Sberna, J. J. A. Baselmans, S. Vollebregt, A. Endo "Characterization of low-loss hydrogenated amorphous silicon films for superconducting resonators", *Proc. SPIE 11453, Millimeter, Submillimeter, and Far-Infrared Detectors and Instrumentation for Astronomy X* (December 2020)

C9. A. Endo, K. Karatsu, Y. Tamura, T. Oshima, A. Taniguchi, T. Takekoshi, S. Asayama, T. J. L. C. Bakx, S. Bosma, J. Bueno, **B. T. Buijtendorp**, K. W. Chin, Y. Fujii, K. Fujita, E. Huijten, R. Huiting, S. Ikarashi, T. Ishida, S. Ishii, R. Kawabe, T. M. Klapwijk, K. Kohno, A. Kouchi, N. Llombart, J. Maekawa, V. Murugesan, S. Nakatsubo, M. Naruse, K. Ohtawara, A. Pascual Laguna, J. Suzuki, K. Suzuki, D. J. Thoen, T. Tsukagoshi, T. Ueda, P. J. de Visser, P. P. van der Werf, S. J. C. Yates, Y. Yoshimura, O. Yurduseven, S. Dabironezare, S. Hähnle, J. J. A. Baselmans, "DESHIMA on ASTE: On-sky performance and upgrade to ultra wideband," *Proc. SPIE 11453, Millimeter, Submillimeter, and Far-Infrared Detectors and Instrumentation for Astronomy X* (December 2020)

Patents

P1. J.J.A. Baselmans (Inventor), **B.T. Buijtendorp** (Inventor), A. Endo (Inventor), S. Vollebregt (Inventor), TU Delft (Applicant) "Low-loss dielectric for high frequency cryogenic applications", *OCT-19-097, H01L, H02N, H01P* (January 2021)

Thesis co-supervised

T1. S. H. de Boer, “Compact MKIDs - Miniaturization of Microwave Kinetic Inductance Detectors”, *M.Sc. thesis*, Delft University of Technology, Delft, the Netherlands (May 2021)

Acknowledgements

I wouldn't have been able to complete this dissertation without the support of the many people around me. I want to start by thanking my excellent supervisory team: Akira, Sten and Jochem. I'm convinced that I couldn't have wished for more inspiring or more supportive supervisors. Akira, I always felt welcome to walk into your office, not only to talk about my research but also about life outside of academia. I'm very grateful for how you supported me, during good times and during difficult times. Furthermore, I'm very thankful for how much you've taught me and for how you always went the extra mile in helping me to become a better scientist. One of the many examples of this was when I had my first presentation at an international conference, and we had practice sessions where you taught me how to become a better storyteller. These are the kind of lessons that I will carry with me for the rest of my life. Sten, I'm very grateful for everything that you have done for me in the last few years. I always felt welcome to reach out to you, and your knowledge about all things related to materials science felt endless and you were always enthusiastic to teach me. You made sure that I could find my way in the EKL cleanroom, and it is thanks to you that I had so many kinds of measurement tools at my disposal. Furthermore, you personally taught me how to do many of the measurements that were essential for my PhD research. You always made me feel that anything was possible, and this can-do attitude was very inspiring and is something that I will always remember in my future work. Jochem, you've always been a tremendous promotor and I'm very grateful for that. Your endless enthusiasm about your work has always been inspiring. The discussions that we had about my research were always interesting and they've been essential in my journey of becoming an independent researcher. Furthermore, you never hesitated to help me with the cryogenic measurements at SRON Leiden and I'm very grateful for this.

Outside of my supervisory team, there are many more people who I have enjoyed working with and who I should thank. David, you were a great mentor

in the Kavli cleanroom, where we spent many hours together especially during the first half of my PhD project. It was always fun to work with you, and you always took great care to teach me as much as possible. Thanks to you I became much more confident in working in the cleanroom, and it was always fun to talk to you about very diverse topics. Furthermore, you always remind the people around you to celebrate all the small victories and I found this an important lesson that I will carry with me. Kenichi, I want to thank you for all the support that you have given me, especially for everything related to the measurements in the Cryo Lab. You are the person who knows every nut and bolt in the lab, and without your help I would never have been able to carry out many parts of my research. Furthermore, you have always been very patient and helpful in answering all my questions, and when I got stuck you never hesitated to help me with troubleshooting. Sebastian, you have also been of great help in getting me up and running in the Cryo Lab, and you have patiently guided me with the measurements at the start of my PhD project and I am very thankful for that. Paolo, you always made me feel welcome to reach out to you in the EKL cleanroom. When I had a problem there, I was often lucky enough to come across you and you were always happy to help me. Furthermore, outside of the cleanroom I have enjoyed your many humorous jokes and I think that you always bring a lot of fun to our research group. Willem, I want to thank you for your help with the measurements at SRON Groningen. You have always very enthusiastically helped me and I am very grateful for that. Furthermore, I want to thank the great cleanroom magicians at SRON who have worked very hard on many difficult chip fabrication steps. David, Vignesh, Dimitry, Ton, Tonny and Martijn, you have all made essential contributions to my work and I want to thank you so much for all your efforts in the cleanroom. Additionally, I want to thank the many PhD students who I've had the pleasure to work with. It's been a pleasure to spend time with you during and after working hours, and I will especially cherish the memories of the fun that we had together when we went to a conference in Yokohama.

Finally, I want to thank the many people from my personal life who've always been there for me. It's nearly impossible to list all my friends and family members who I'm grateful for. I hope that everyone of you knows how much I appreciate you for always being there for me. I'm very grateful to my parents, Monica and Tom, for all the love that they've given me and for all the support that they've given me throughout my entire life. I want to thank my siblings, Carmen, Adriaan and Marcus, for always being there for me. Fenna, I'm very grateful for all the love and support that you've given me, for all the fun that we've had together in the past few years, and for everything that I've learned from you.

ISBN/EAN 978-94-6384-777-3